

**Probing Surface Heterogeneity, Electrochemical Properties and Bubble-Solid
Interaction Mechanisms of Sulfide Minerals in Flotation**

by

Lei Xie

A thesis submitted in partial fulfillment of the requirements for the degree of

Doctor of Philosophy

in

Chemical Engineering

Department of Chemical and Materials Engineering
University of Alberta

© Lei Xie, 2017

Abstract

The colloidal stability governed by various surface interactions including van der Waals (VDW) interaction, electrical double layer (EDL) interaction, hydrophobic interaction, and some other interactions, plays an important role in a wide range of natural phenomena and engineering applications. The basic understanding of surface properties and interaction mechanisms of colloidal particles is of both fundamental and practical importance in many engineering processes such as mineral froth flotation. In this study, the surface characteristics of sulfide minerals, such as sphalerite, galena and molybdenite, were investigated in complex aqueous media using several complementary experimental techniques to better elucidate the surface heterogeneity, electrochemical properties and bubble-particle interaction mechanisms that contribute to various interfacial phenomena in flotation.

Atomic force microscopy (AFM) force mapping was applied to probe the nanoscale heterogeneity of surface hydrophobicity and surface interactions on sphalerite surface before/after conditioning treatment (i.e. copper activation and xanthate adsorption). It was shown that sphalerite surface was hydrophilic with homogeneous surface hydrophobicity, while conditioned sphalerite exhibited heterogeneous distribution of surface hydrophobicity due to non-uniform adsorption of xanthate. The significantly enhanced adhesion after conditioning treatment with chemical reagents originated from the additional hydrophobic attraction.

Equipped with the electrochemical setup, the interfacial chemical reaction and evolution of surface characteristics (i.e. morphological changes and surface interactions) on galena surface were simultaneously measured using AFM at the nanoscale. The in-situ

topographic imaging revealed homogeneous electrochemical oxidation across the mineral surface, leading to slight surface roughening at the applied potential of 0 V (0.206 V vs standard hydrogen electrode) and more pronounced surface roughening at higher potentials (e.g. 0.3 V and 0.45 V). The quantitative force results demonstrated that hydrophobic interaction was strengthened with increasing the applied potential from -0.7 V to 0.45 V, which agreed well with the enhanced hydrophobicity of galena surface. The electrochemical oxidation at 0 V was believed to be the formation of metal-deficient lead sulfide, while the oxidation at 0.45 V arose from the formation of elemental sulfur that was further confirmed by cryo-XPS.

Furthermore, AFM bubble probe technique was employed to quantitatively measure the interaction forces between air bubbles and mineral surfaces (i.e. sphalerite before/after conditioning treatment and molybdenite before/after depressant adsorption). Surface forces were shown to play the critical role in bubble-mineral interaction and attachment, which agreed excellently with the theoretical calculations based on Reynolds lubrication theory and augmented Young-Laplace equation by including the effect of disjoining pressure. Increasing the salt concentration led to weakened EDL repulsion, and thus facilitated the bubble-mineral attachment. For the hydrophilic sphalerite case, the bubble was more readily attached to the mineral surface after conditioning treatment, which was contributed from the strengthened hydrophobic attraction. For the hydrophobic molybdenite case, the adsorption of polymer depressant weakened hydrophobic attraction and induced steric repulsion, thereby stabilizing thin water film and inhibiting bubble-mineral attachment.

This work provides novel methodologies to study the surface properties and interaction mechanisms of sulfide minerals in complex aqueous media at the nanoscale. The results in this work provide valuable and quantitative information on the fundamental understanding of surface heterogeneity, electrochemical properties and bubble-particle interaction mechanisms of sulfide minerals in complex aqueous media, which can be readily extended to many mineral systems and other related engineering processes.

Preface

Chapter 3 of this thesis will be submitted for publication as Xie, L.; Wang, J.; Shi, C.; Cui, X.; Huang, J.; Zhang, H.; Liu, Q.; Liu, Q.; Zeng H., “Mapping Nanoscale Heterogeneity of Surface Hydrophobicity on Sphalerite Mineral.” I was responsible for surface characterization, AFM force mapping, data analysis, and manuscript composition. Dr. J. Wang assisted with cryo-XPS analysis, force curve analysis, and manuscript edits. C. Shi assisted with AFM force mapping and surface energy measurement. X. Cui, J. Huang, Dr. H. Zhang, Dr. Q. Liu and Dr. Q. Liu contributed to the manuscript edits. Dr. Hongbo Zeng was the supervisory author and was involved in concept formation and manuscript composition.

Chapter 4 of this thesis has been published as Xie, L.; Wang, J.; Shi, C.; Huang, J.; Zhang, H.; Liu, Q.; Liu, Q.; Zeng H., “Probing Surface Interactions of Electrochemically Active Galena Mineral Surface Using Atomic Force Microscopy,” *The Journal of Physical Chemistry C*, vol. 120, issue 39, 22433-22442. I was responsible for surface characterization, electrochemical AFM measurement, data analysis, and manuscript composition. Dr. J. Wang assisted with electrochemical AFM setup, force curve analysis and manuscript edits. C. Shi assisted with AFM imaging and force measurement. J. Huang, Dr. H. Zhang, Dr. Q. Liu, and Dr. Q. Liu contributed to the manuscript edits. Dr. Hongbo Zeng was the supervisory author and was involved in concept formation and manuscript composition.

Chapter 5 of this thesis has been published as Xie, L.; Shi, C.; Wang, J.; Huang, J.; Lu, Q.; Liu, Q.; Zeng H., “Probing the Interaction between Air Bubble and Sphalerite Mineral Surface Using Atomic Force Microscopy,” *Langmuir* 2015, 31, 2438-2446. I was responsible for surface characterization, AFM force measurement, data analysis, and

manuscript composition. C. Shi assisted with preparation of bubble probe, force curve analysis and manuscript edits. Dr. J. Wang assisted with AFM imaging and surface characterization. J. Huang, Q. Lu, and Dr. Q. Liu contributed to the manuscript edits. Dr. Hongbo Zeng was the supervisory author and was involved in concept formation and manuscript composition.

Chapter 6 of this thesis will be submitted for publication as Xie, L.; Wang, J.; Yuan, D.; Shi, C.; Cui, X.; Zhang, H.; Liu, Q.; Liu, Q.; Zeng H., “Interaction Mechanisms between Air Bubble and Molybdenite Surface: Impact of Solution Salinity and Polymer Adsorption.” I was responsible for surface characterization, AFM force measurement, data analysis, and manuscript composition. Dr. J. Wang assisted with AFM imaging, surface characterization and manuscript edits. D. Yuan assisted with mineral flotation. C. Shi, X. Cui, Dr. H. Zhang, Dr. Q. Liu and Dr. Q. Liu contributed to the manuscript edits. Dr. Hongbo Zeng was the supervisory author and was involved in concept formation and manuscript composition.

Chapters 1, 2, and 7 are originally written by Lei Xie, and have never been published before.

Acknowledgement

I would love to express my sincere gratitude to Dr. Hongbo Zeng for his excellent guidance and inspiring encouragement throughout the course of my PhD study. His passion and dedication into scientific research always inspired me to pursue my career goal as a researcher. I also wish to thank Dr. Qingxia Liu for his experienced suggestions. His widespread industrial experience and excellent safety attitude during work set an example for me.

I wish to thank all my group members for their solid support and kind help during my PhD study. Special thanks are given to Dr. Jingyi Wang and Mr. Chen Shi for their generous help in valuable discussion and revision of my manuscripts throughout the project.

I would like to acknowledge Dr. Shihong Xu and Dr. Anxiang He in nanoFAB for their assistance with cryo-XPS and FE-SEM measurements.

The financial support from the Natural Sciences and Engineering Research Council of Canada (NSERC), Canadian Centre for Clean Coal/Carbon and Mineral Processing Technologies (C5MPT), the Canada Foundation for Innovation (CFI) and the Alberta Advanced Education & Technology Small Equipment Grants Program (AET/SEGP) is gratefully appreciated.

Finally, my deepest gratitude goes to my family. I am forever grateful to my parents, my wife Ms. Qiuyi Lu and my son Oscar Xie for their love and support.

Table of Contents

List of Tables	xii
List of Figures.....	xiii
List of Acronyms	xx
Chapter 1 Introduction	1
1.1 Principles of mineral flotation	1
1.2 Challenges of mineral flotation	2
1.3 Interactions involved in mineral flotation	5
1.3.1 Van der Waals (VDW) force	5
1.3.2 Electrical double layer (EDL) force	6
1.3.3 Derjaguin-Landau-Verwey-Overbeek (DLVO) theory	7
1.3.4 Non-DLVO forces	8
1.4 Direct force measurements	9
1.5 Objectives	12
1.6 Structure of the thesis	13
1.7 References	14
Chapter 2 Experimental Methods	21
2.1 Preparation of mineral surfaces	21
2.2 Surface characterization	22
2.3 Preparation of AFM bubble probe.....	23
2.4 References	24
Chapter 3 Mapping Nanoscale Heterogeneity of Surface Hydrophobicity on Sphalerite Mineral	25
3.1 Introduction	25
3.2 Materials and methods.....	28

3.2.1 Materials	28
3.2.2 Preparation of sphalerite surface	29
3.2.3 Surface characterization	29
3.2.4 Adhesion force mapping.....	30
3.2.5 Force curve analysis	31
3.2.6 Surface energy measurement.....	33
3.3 Results and discussion.....	34
3.3.1. Cryo-XPS	34
3.3.2 Contact angle measurements	35
3.3.3 Adhesion force mapping.....	38
3.3.4 Adhesion energy	44
3.4 Conclusions	45
3.5 Acknowledgement.....	46
3.6 References	46

Chapter 4 Probing Surface Interactions of Electrochemically Active Galena Mineral

Surface using Atomic Force Microscopy	53
4.1 Introduction	53
4.2 Materials and methods.....	56
4.2.1 Materials	56
4.2.2 Electrochemical experiments.....	57
4.2.3 Electrochemical atomic force microscopy (EC-AFM).....	58
4.2.4 Surface characterization	60
4.2.5 Force curve analysis	61
4.3 Results and discussion.....	62
4.3.1 Cyclic voltammetry (CV)	62
4.3.2 Contact angle measurements	63
4.3.3 In situ topographic imaging.....	65
4.3.4 Cryo-XPS and conductive AFM.....	67
4.3.5 AFM force measurements	70

4.4 Conclusions	76
4.5 Acknowledgements	77
4.6 References	77
Chapter 5 Probing the Interaction between Air Bubble and Sphalerite Mineral	
Surface using Atomic Force Microscopy	84
5.1 Introduction	84
5.2 Materials and methods.....	86
5.2.1 Materials	86
5.2.2 Preparation of sphalerite surface	87
5.2.3 Surface characterization	88
5.2.4 Force measurements	88
5.2.5 Theoretical model.....	90
5.3 Results and discussion.....	92
5.3.1 Surface characterization	92
5.3.2 Bubble-sphalerite interaction in 500 mM NaCl solution.....	93
5.3.3 The effect of conditioning treatment	97
5.3.4 The effects of solution ionic strength	100
5.4 Conclusions	106
5.5 Acknowledgement.....	107
5.6 References	107
Chapter 6 Interaction Mechanisms between Air Bubble and Molybdenite Surface:	
Impact of Solution Salinity and Polymer Adsorption	115
6.1 Introduction	115
6.2 Materials and methods.....	117
6.2.1 Materials	117
6.2.2 Preparation of molybdenite surface.....	118
6.2.3 Surface characterization	118
6.2.4 Force measurements	119

6.2.5 Theoretical model.....	120
6.2.6 Microflotation tests.....	122
6.3 Results and discussion.....	122
6.3.1. Surface morphology	122
6.3.2. Surface wettability.....	126
6.3.3 Bubble-molybdenite interaction	127
6.3.4 Effect of polymer adsorption on the interaction.....	131
6.3.5 Molybdenite flotation.....	134
6.4 Conclusions	135
6.5 Acknowledgement.....	136
6.6 References	136
Chapter 7 Conclusions and Future Work.....	144
7.1 Major conclusions	144
7.2 Original contributions.....	146
7.3 Suggestions for future work	147
Bibliography	149

List of Tables

Table 3.1 The average static/advancing/receding water contact angle and contact angle hysteresis of sphalerite and conditioned sphalerite	36
Table 3.2 Surface energy γ with Lifshitz-van der Waals γ^{LW} and Lewis acid-base γ^{AB} (electron acceptor γ^+ and electron donor γ^-) components for different surfaces, mJ/m ²	45
Table 5.1 Comparison of theoretically fitted surface potential values of air bubble and the literature values.....	103
Table 5.2 Comparison of theoretically fitted surface potential values of sphalerite and the measured zeta potential values of sphalerite particles.....	103
Table 5.3 Ion composition of the saline water	105
Table 6.1 Comparison of theoretically fitted surface potentials and literature values of air bubble and molybdenite in different solution conditions.....	130

List of Figures

Figure 1.1 Schematic of DLVO interaction energy versus separation distance between two similarly charged surfaces in 1:1 electrolyte solution.....	8
Figure 1.2 Schematic of typical AFM force measurements using AFM probe.....	10
Figure 3.1 The schematic of AFM adhesion force mapping on mineral surface. Inset figure shows the geometry of conical AFM tip with a spherical cap at the apex, where α is the geometry angle for spherical cap, R is the radius of spherical cap, r is the radius of the circle of the tip at a given vertical position, D is the distance between the tip end and mineral surface.....	32
Figure 3.2 Typical FE-SEM images for analysis of the geometry of thiol-functionalized AFM tips.....	33
Figure 3.3 Cryo-XPS spectra of S 2p for (A) sphalerite and (B) conditioned sphalerite, and C 1s for (C) sphalerite and (D) conditioned sphalerite.....	35
Figure 3.4 Topographic image (A) and corresponding adhesion map (B) of sphalerite surface, and topographic image (C) and corresponding adhesion map (D) of conditioned sphalerite surface.....	39
Figure 3.5 The histograms of measured adhesion F_{adh}/R and the fitted Gaussian distributions (solid curve) of (A) sphalerite and (B) conditioned sphalerite.....	41

Figure 3.6 Interaction force between the hydrophobic AFM tip and sphalerite surface in 0.5 M NaCl. Experiment results are shown in open symbols, and theoretical calculations based on the classical DLVO model are shown in red curve.....42

Figure 3.7 Interaction force between the hydrophobic AFM tip and different domains (i.e. domain I, II, III, and IV) of conditioned sphalerite in 0.5 M NaCl. Experiment results are shown in open symbols, and theoretical calculations based on the classical DLVO model and extended DLVO model including the hydrophobic effect are shown in red curve and green curve, respectively.....43

Figure 4.1 (A) The schematic of EC-AFM for the topographic imaging and force measurements on galena mineral surface during a typical electrochemical AFM experiment. Inset figure shows the geometry of conical AFM tip with a spherical cap at the apex, where α is the geometry angle for spherical cap, R is the radius of spherical cap, r is the radius of the circle of the tip at a given vertical position, D is the distance between the tip end and galena surface, and L is the distance between a differential surface section of the tip and galena surface. (B) Typical FE-SEM images for analysis of the geometry of AFM tips.....58

Figure 4.2 CV curve of galena surface in 0.5 M NaCl at a potential sweep rate of 0.02 V/s.....63

Figure 4.3 Static water contact angle of galena surface as a function of electrochemical potential.....64

Figure 4.4 AFM topographic images ($5 \times 5 \mu\text{m}^2$) of galena surface at the electrochemical potential of (A) -0.7 V, (B) -0.3 V, (C) 0 V, (D) 0.3 V, and (E) 0.45 V for 20 s in 0.5 M NaCl.....65

Figure 4.5 XPS spectra of S 2p for potentiostatically treated galena surface at the electrochemical potential of -0.7 V, 0 V and 0.45 V.....68

Figure 4.6 The topographic images and corresponding current distributions ($2 \times 2 \mu\text{m}^2$) of potentiostatically treated galena surface at the electrochemical potential of (A) -0.7 V, (B) 0 V and (C) 0.45 V.....70

Figure 4.7 The interaction force F (left axis) between silicon nitride AFM tip and galena surface potentiostatically treated at various electrochemical potentials in 0.5 M NaCl and the corresponding interaction energy (W) per unit area between two flat surfaces (right axis) given by $W = F/2\pi R$ as a function of separation distance (D). The inset shows zoomed-in view at short separation. Experiment results are shown in open symbols, and DLVO calculations are shown in red curve.....71

Figure 4.8 The interaction force F (left axis) between the hydrophobic OTS modified tip and galena surface potentiostatically treated at the electrochemical potential of (A) -0.7 V, (B) -0.3 V, (C) 0 V, (D) 0.3 V, and (E) 0.45 V in 0.5 M NaCl, and the corresponding interaction energy (W) per unit area between two flat surfaces (right axis) given by $W = F/2\pi R$ as a function of separation distance (D). The inset shows zoomed-in view at short separation. Experiment results are shown in open symbols, and theoretical calculations based on VDW interaction and the extended DLVO model including the effect of hydrophobic interaction (HB) are shown in green curves and red curves, respectively.....72

Figure 4.9 The histograms of measured adhesion F_{ad}/R and the fitted Gaussian distributions between the hydrophobic OTS modified AFM tip and galena surface potentiostatically treated at different electrochemical potentials.....75

Figure 5.1 (A) Optical microscope image of a cantilever-attached bubble with radius of 75 μm which is used as an AFM bubble probe. (B) Schematic of force measurements between air bubble and sphalerite surface in aqueous solution using the AFM bubble probe. h_{min} is the minimum separation or minimum film thickness of the confined water film between air bubble and solid surface.....89

Figure 5.2 AFM topographic images ($5 \times 5 \mu\text{m}^2$) of (A) sphalerite surface and (B) conditioned sphalerite surface.....92

Figure 5.3 The interaction and the corresponding minimum film thickness of the confined water film as a function of time between an air bubble of radius 75 μm and a sphalerite surface in 500 mM NaCl solution under approaching velocity of (A) $v = 1 \mu\text{m/s}$, (B) $v = 10 \mu\text{m/s}$, and (C) $v = 30 \mu\text{m/s}$. Experiment results are shown in open symbols, and theoretical calculations are shown in solid curves. For all these figures, the constant C and the decay length D_0 used are 0.08 N/m and $1.0 \pm 0.1 \text{ nm}$, respectively.....95

Figure 5.4 The interaction and the corresponding minimum film thickness of the confined water film as a function of time between an air bubble of radius 75 μm and a conditioned sphalerite surface in 500 mM NaCl solution under different approaching velocities $v = 1$ and $30 \mu\text{m/s}$ (open symbols for experiment results, and solid curves for theoretical calculations). The constant C and the decay length D_0 used are 0.41 N/m and $1.5 \pm 0.1 \text{ nm}$, respectively.....98

Figure 5.5 The VDW disjoining pressure Π_{VDW} , hydrophobic disjoining pressure Π_{HB} and the overall disjoining pressure Π for the interactions of bubble-water-sphalerite and bubble-water-conditioned sphalerite in 500 mM NaCl solution (air bubble radius $\sim 75 \mu\text{m}$).....99

Figure 5.6 The interaction and the corresponding minimum film thickness of the confined water film as a function of time between an air bubble of radius $75 \mu\text{m}$ and a sphalerite surface at low ionic concentration solutions: (A) 1 mM NaCl, (B) 10 mM NaCl and (C) 10 mM CaCl_2 , under a low approaching velocity $v = 1 \mu\text{m/s}$ (open symbols for experiment results, and solid curves for theoretical calculations). The constant C and the decay length D_0 used are 0.08 N/m and $1.0 \pm 0.1 \text{ nm}$, respectively.....102

Figure 5.7 The overall disjoining pressure Π for the bubble-water-sphalerite interaction in various solution conditions (air bubble radius $\sim 75 \mu\text{m}$).....104

Figure 5.8 The measured interaction forces between an air bubble of radius $75 \mu\text{m}$ and a sphalerite surface under different approaching velocities in saline water (mixture of simulated seawater and process water as shown in Table 2.3).....105

Figure 6.1 Schematic of force measurements between air bubble and molybdenite surface in aqueous solution using the bubble probe AFM.....120

Figure 6.2 AFM height (Left) and phase (Right) images ($5 \times 5 \mu\text{m}^2$) of molybdenite surface conditioned at different polymer concentrations: (A) 0 ppm, (B) 1 ppm, (C) 5 ppm, (D) 10 ppm, and (E) 50 ppm at pH 9.....124

Figure 6.3 AFM height images ($5 \times 5 \mu\text{m}^2$) of molybdenite surface conditioned in 1 ppm polymer solution with the addition of (A) 10 mM and (B) 100 mM NaCl at pH 9.....125

Figure 6.4 Zeta potential of (A) guar gum (measured values) and (B) molybdenite (literature values) at different salt concentrations at pH 9.⁴⁸⁻⁵¹126

Figure 6.5 Water contact angle of molybdenite surface conditioned at different polymer concentrations.....127

Figure 6.6 Interaction forces (A-C) and calculated thin water film profile at maximum force load (D-F) between air bubble and molybdenite surface in NaCl solutions of different concentrations: 100 mM (A and D), 10 mM (B and E) and 1 mM (C and F) at an approaching velocity $v = 1 \mu\text{m/s}$ at pH 9 (open symbols for experiment results and red curves for theoretical calculations).....128

Figure 6.7 Calculated disjoining pressure profiles between air bubble and molybdenite surface in NaCl solutions of different concentrations: (A) 100 mM, (B) 10 mM and (C) 1 mM.....131

Figure 6.8 Interaction forces between air bubble and molybdenite surface conditioned in (A) 1 ppm polymer solution and (B) 5 ppm polymer solution in 100 mM NaCl at $v = 1 \mu\text{m/s}$ at pH 9 (open symbols for experiment results and solid curves for theoretical calculations).....132

Figure 6.9 Normalized interfacial adhesion F_{adh}/R measured between air bubble and molybdenite surface conditioned in 5 ppm polymer solution at different values of (A)

maximum force load F_{max} and (B) contact time $t_{contact}$ at a maximum force load $F_{max} = 18$ nN.....133

Figure 6.10 Flotation recovery of molybdenite in polymer solution of different concentrations in 100 mM NaCl at pH 9.....134

List of Acronyms

VDW	van der Waals
EDL	electrical double layer
AFM	atomic force microscopy
EC-AFM	electrochemical atomic force microscopy
CV	Cyclic Voltammetry
DLVO	Derjaguin-Landau-Verwey-Overbeek
CFM	chemical force microscopy
SAMs	self-assembled monolayers
RICM	reflection interference contrast microscopy
TPCL	three-phase contact line
OTS	octadecyltrichlorosilane
FTIR	fourier transform infrared spectroscopy
XPS	X-ray photoelectron spectroscopy
ToF-SIMS	time of flight secondary ion mass spectrometry
SECM	scanning electrochemical microscopy
DMT	Derjaguin-Muller-Toporov
VCG	Van Oss-Chaudhury-Good
rms	root-mean-square
SFA	surface forces apparatus
OCP	Open circuit potential
PAX	Potassium amyl xanthate

CMC carboxymethyl cellulose

MIBC 4-Methyl-2-pentanol

Chapter 1 Introduction

1.1 Principles of mineral flotation

Froth flotation is an important mining and mineral processing technique used to selectively separate valuable minerals from gangue minerals based on their attachment propensities to air bubbles.¹⁻³ Due to the difference in the interactions between air bubbles and mineral particles, hydrophobic particles more readily attach to air bubbles and rise to the surface of the pulp to form a mineralized froth, and hydrophilic particles remain suspended in the pulp as the tailings.¹⁻³

Sulfide minerals, a class of minerals containing sulfide (S^{2-}), are economically important as metal sources. The majority of sulfide minerals are metallic and opaque, some of which exhibit perfect cleavage along the crystal plane such as sphalerite, galena and molybdenite. Most sulfide minerals are naturally hydrophilic and difficult to float with air bubbles without the presence of chemical reagents known as collectors. Short-chain xanthates are widely used as collectors to enhance the hydrophobicity and floatability of sulfide minerals.³⁻⁵

Sphalerite, consisting largely of zinc sulfide, crystallizes in the isometric crystal system, where zinc and sulfur atoms are tetrahedrally coordinated. Due to the relative instability of zinc-xanthate, sphalerite responds poorly to thiol collectors, and thus the activators are commonly used to improve the adsorption of xanthate on sphalerite surface.³⁻⁵ Cu^{2+} is the most widely used activator, and some other heavy metal ions (e.g. Pb^{2+} , Fe^{2+}/Fe^{3+}) in ore deposits or process water can also activate sphalerite.³⁻⁵ Copper activation of sphalerite was generally considered to follow an ion exchange mechanism

between Cu(II) in aqueous solution and Zn(II) on sphalerite surface; thereafter, Cu(II) on sphalerite surface is reduced to Cu(I), which reacts with xanthates to form stable Cu(I)-xanthate, thereby resulting in the oxidation of surface sulfide to hydrophobic species such as polysulfide, metal-deficient sulfide and elemental sulfur.³⁻⁵

Galena (natural mineral of lead sulfide) crystallizes in the isometric crystal system, where lead and sulfur atoms form a close-packed cubic unit cell. As compared to sphalerite, galena responds better to thiol collectors due to stronger lead-xanthate interaction. In addition, galena is a semiconductor material with a small band gap of ~0.4 eV, so electrochemical treatment, due to its cost-effective and environment-friendly properties, can be a feasible alternative to enhance the hydrophobicity and floatability of galena particles.⁶

Molybdenite, natural mineral of molybdenum disulfide, consists of a sheet of molybdenum atoms sandwiched between sheets of sulfur atoms. The Mo-S covalent bonds are very strong, thereby resulting in a stable sandwich-like tri-layer structure. The interaction between two tri-layer structures is van der Waals force, which is easy to break to expose the naturally hydrophobic basal plane. Molybdenite frequently occurs in the form of copper-molybdenum ores, and the common practice is to depress chalcopyrite from the bulk concentrate.⁷⁻⁹

1.2 Challenges of mineral flotation

Over the past few decades, substantial progress has been achieved with respect to the interfacial phenomena in the flotation of sulfide minerals,^{1-5, 10-12} yet there are still considerable knowledge gaps between the fundamental understanding of nanoscopic interaction mechanisms at the air/water/mineral interfaces and the macroscopic mineral

flotation, particularly for the challenging issues associated with complex water chemistry and fine particle flotation.¹³⁻¹⁷

Due to the shortage of available fresh water sources and restrictions for disposal of used water to the environment, the use of recycled water and seawater in mineral process is believed to be a sustainable solution. Recently, recycled water and seawater have been successfully applied in the flotation of several sulfide minerals such as Cu-Mo, Cu-Pb-Zn and Cu-Au ores.^{13-15, 18-19} Increasing research interest has been focused on the effect of water chemistry on the interfacial phenomena in mineral flotation such as surface properties and bubble-particle attachment.^{13-15, 18-23} The presence of electrolytes was found to significantly influence the surface properties of mineral particles (e.g. hydration layer) and air bubbles (e.g. bubble coalescence and froth stability), thereby affecting the flotation performance.²⁰⁻²² The bubble-mineral attachment governed by the interaction forces between air bubbles and mineral particles has been characterized in electrolyte solutions, which showed the attachment efficiency was closely related to the mineral size, surface hydrophobicity and salt concentration.²³⁻²⁴ Nevertheless, the basic understanding of the interaction mechanisms in complex aqueous media, particularly for the bubble-mineral interaction, is still very limited.

Fine particle flotation has also puzzled researchers due to the low collision and attachment efficiencies of fine particles with air bubbles, which significantly affects the recovery and selectivity of valuable minerals.¹⁶⁻¹⁷ The efficiencies of bubble-particle collision and attachment were reported to increase with decreasing bubble size.²⁵⁻²⁷ Hence, various methods have been attempted to improve the performance of fine particle flotation by decreasing bubble size.²⁸⁻³⁰ Hydrodynamic cavitation is a mechanical

approach used for generating tiny bubbles (e.g. nanobubbles) that are preferentially anchored onto the hydrophobic domains of fine particles, thereby enabling the attachment of fine particles to conventional sized bubbles in mineral flotation.²⁹ Dissolved gas flotation is a physiochemical approach to generate “nuclear” air on the hydrophobic domains of fine particles by precipitating the gas molecules in supersaturated state.³⁰ As compared to hydrodynamic cavitation, the low air flow rate of dissolved gas flotation can cause relatively low selectivity, which makes it only suitable for fine particle flotation in wastewater treatment.³⁰ In fine particle flotation, the hydrophobic domains of fine particles provide the anchoring sites for tiny bubbles, and thus elucidating the size and distribution of hydrophobic domains will help modulate the hydrophobic domains toward improved flotation performance of fine particles.

Some other challenging issues include collectorless flotation with electrochemical treatment and thin film drainage process. Fully solving the above challenges highly relies on a basic understanding of the surface properties and interaction mechanisms involved in the respective mineral systems, which will underlie great opportunities in controlling the air/water/mineral interfaces toward developing novel mineral processing technologies. Compared to the extensive studies on the composition, characterization and floatability associated with the flotation of sulfide minerals, limited reports are available on elucidating the surface properties and interaction mechanisms (i.e. surface heterogeneity, electrochemical properties and bubble-particle interaction) at the nanoscale in mineral systems, and such studies are urgently needed in the field of mineral process.

1.3 Interactions involved in mineral flotation

In mineral flotation, the interactions between air bubbles and mineral particles determine the flotation recovery, while the interactions between air bubbles and gangue particles and between mineral particles and gangue particles govern the flotation selectivity. The interactions that contribute to various interfacial phenomena in mineral flotation involve van der Waals (VDW) force, electrical double layer (EDL) force, hydrophobic force, and some other forces such as steric force.

1.3.1 Van der Waals (VDW) force

The VDW force, named after Dutch physicist J. D. van der Waals, is the sum of attractive or repulsive forces between atoms, molecules and even surfaces arising from intermolecular interactions with the exclusion of chemical bonds. Keesom interaction (dipole-dipole interaction between two polar molecules), Debye interaction (dipole-induced dipole interaction between a polar molecule and a non-polar molecule) and Dispersion interaction (instantaneously induced dipole-instantaneously induced dipole interaction between two non-polar molecules), each varying with the inverse sixth power of the distance, together contribute to the total VDW interaction.³¹

The VDW force between two objects in a medium can be attractive or repulsive based on the Lifshitz theory by considering the influence of neighboring atoms on the interaction between any pair of atoms. The VDW force is attractive provided that the parameters (i.e. dielectric constant, refractive index) of the medium are lower or higher than those of two objects (e.g. mineral-gangue interaction in water). On the other hand,

the VDW force is repulsive provided that the parameters of the medium lie between those of two objects (e.g. bubble-mineral interaction in water).³¹

1.3.2 Electrical double layer (EDL) force

Most particles suspended in water carry surface charges, which may be originated from the ionization of surface groups, the adsorption of ions from solution, or charge exchange mechanism.³¹ Whatever the charging mechanism, the surface charge of co-ions is balanced by counterions to sustain the colloidal system electrically neutral. Some of the counterions are firmly bound to the surface via coulomb force within the stern layer, in which the electric potential linearly decreases with the distance, whereas other loosely associated counterions are free to move within the diffuse layer under the influence of electric attraction and thermal motion, in which the electrical potential distribution follows the Poisson-Boltzmann equation.³¹ Thus, an EDL develops near the charged surface in aqueous solution.

When two particles approach each other, the EDL of each particle overlaps. The potential profile between these two particles induces the variation of ionic concentration within the gap with respect to the bulk solution and generates an osmotic pressure, which is the origination of EDL force.³¹ The strength of EDL force increases with the magnitude of surface potential, but decreases with the distance up to a few tenths of nanometers. The EDL force between two similarly charged surfaces is repulsive and decays exponentially at large separation, though the force can turn to attraction at small separation under certain conditions. On the other hand, the EDL force between two oppositely charged surfaces is attractive at any separation.

When the particle moves in aqueous solution, the ions and ion-bearing solution inside the shear plane simultaneously move with the particle due to coulomb attraction between charged surface and surrounding counterions. The potential at the shear plane (viz. zeta potential) could be measured through electrophoresis phenomenon and commonly used to characterize the surface charge of particles in colloidal system. Once an electric field is applied across the suspension, charged particles are attracted toward the oppositely charged electrode and the electrophoretic mobility can be used to calculate zeta potential through different equations depending on the particle size.

1.3.3 Derjaguin-Landau-Verwey-Overbeek (DLVO) theory

The DLVO theory is widely used to quantitatively describe the interaction and stabilization mechanisms in colloidal systems by considering the effects of VDW and EDL interactions. The net DLVO interaction energy is considered as the sum of VDW interaction energy and EDL interaction energy. Figure 1.1 shows the schematic of DLVO interaction energy between two similarly charged surfaces in 1:1 electrolyte solution.

The VDW attraction is insensitive to the variation of solution conditions such as ionic concentration and pH condition, which rises quickly and turns infinite as separation distance $D \rightarrow 0$. For highly charged surfaces in low ionic concentration solution, a strong EDL interaction results in a long-range repulsion and an energy barrier, which inhibit the surfaces approaching each other and sustain a stable colloidal system.³¹ To break the stable colloidal system, the ionic concentration can be increased to weaken the EDL repulsion and reduce the energy barrier.³¹ Therefore, the DLVO interaction energy plays an important role in bubble-particle attachment and particle-particle aggregation in mineral flotation.

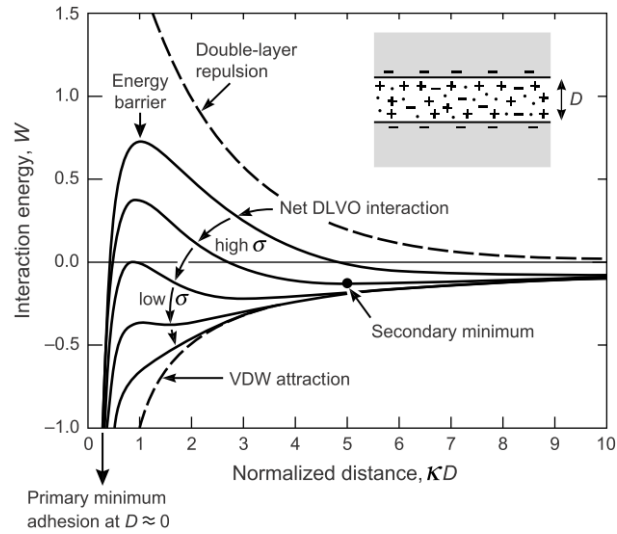


Figure 1.1 Schematic of DLVO interaction energy versus separation distance between two similarly charged surfaces in 1:1 electrolyte solution.³¹

1.3.4 Non-DLVO forces

The DLVO theory has been successfully used to describe the colloidal stability with the effects of only VDW and EDL interactions. Once the colloidal system becomes complicated, the DLVO theory fails to describe the phenomena due to additional non-DLVO forces such as hydrophobic and steric interactions.

Hydrophobic interaction, referring to the usually strong attraction between hydrophobic atoms, molecules and even surfaces in aqueous solution, is ubiquitous in a wide range of water-based systems, such as Lotus-inspired self-cleaning technologies,³² self-assembly of biomolecules,³³ and aggregation of oil droplets in water.³⁴ In mineral flotation, hydrophilic mineral particles remain suspended in slurry due to the repulsive DLVO interaction at large separation, while hydrophobic mineral particles can attach to air bubbles due to the additional hydrophobic attraction that overcomes the energy barrier of DLVO interaction. Until now the exact origin of hydrophobic interaction is still not fully understood. Nevertheless, the hydrophobic interaction is generally considered to

originate from the fact that hydrophobic moieties cannot form hydrogen bonds with adjacent water molecules, thereby resulting in specific orientation of adjacent water molecules and loss of configurational entropy.³⁵

The steric repulsion is also very important in mineral flotation, especially when water-soluble polymers are used as chemical reagents. Generally, when two mineral particles covered with polymers approach each other, the polymer chains dangle out into the solution with thermal mobility, thereby resulting in a repulsive entropic force for overlapping polymer molecules.

1.4 Direct force measurements

A complete understanding of the fundamental interaction mechanisms in mineral flotation requires the essential information on the force-distance profile of solid-solid and bubble-solid interactions. Atomic force microscopy (AFM) has been extensively used to quantify different intermolecular and surface forces, such as VDW, EDL and hydrophobic interactions, with sub-nN resolution in a wide range of systems.³⁶⁻⁴⁰ The schematic of typical AFM setup is shown in Figure 1.2. During the force measurements, the AFM probe was positioned over a solid surface and then driven to approach and retract toward the surface. The deflection of the cantilever was detected through a laser beam that was reflected from the cantilever to a photodiode detector, which was further converted to the force using the Hooke's law. Although AFM is not able to directly measure the absolute separation between two interacting surfaces, it can provide valuable and complementary information on the interaction mechanisms in complex aqueous media.

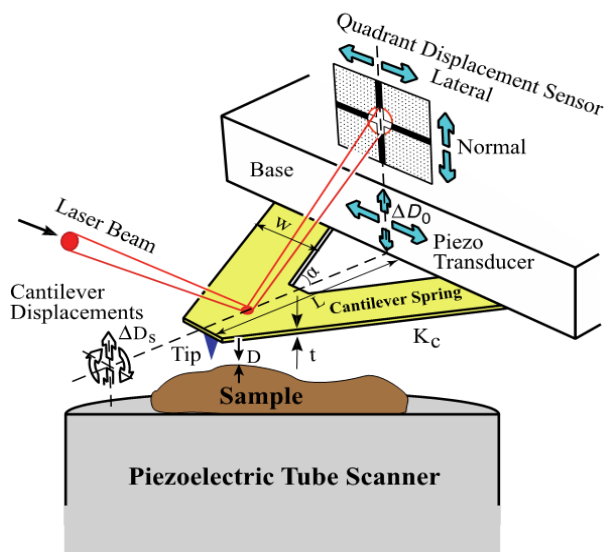


Figure 1.2 Schematic of typical AFM force measurements using AFM probe.

In 1991, AFM colloidal probe technique was developed to measure the interaction forces between a silica sphere probe and a silica surface in various aqueous solutions for the first time.⁴¹ The spherical colloidal particle, which could be silica, ZnS or other materials, was glued onto tipless cantilever and then driven to interact with all types of solid surfaces.³⁶⁻⁴⁰ In contrast, the measurements of deformable air bubbles were far more complicated than that of solid surfaces due to the practical challenge of precisely manipulating deformable objects and interpreting force results. The first force measurements between solid particles and air bubbles can be traced back to 1994, in which the colloidal probe was driven to interact with an air bubble immobilized on a hydrophobized substrate.⁴² This approach makes it possible to directly measure the interaction forces between deformable air bubbles and different solid particles.⁴²⁻⁴⁶ It was found that the repulsive VDW and EDL interactions could sustain thin water films between air bubbles and hydrophilic substrates, whereas attractive hydrophobic interaction could induce thin water film rupture and bubble attachment on hydrophobic

surfaces.⁴²⁻⁴⁶ The addition of surfactants was also found to effectively inhibit the thinning process of confined water film.⁴³⁻⁴⁶ In all of these studies, however, the bubble deformation was calculated based on the assumption that the bubble could be considered as a linear Hookean spring with an effective spring constant equal to the surface tension, which was later proven unsuitable to interpret the measured forces due to the nonlinear nature of bubble deformation in response to external forces.⁴⁷ Moreover, many materials can only be prepared as the flat surface (e.g. mica, molybdenite, graphite), which in certain cases limited the application of AFM colloidal probe technique for measuring the interaction forces between colloidal particles and air bubbles.

Recently, the AFM bubble probe technique was developed by anchoring an air bubble on the tipless cantilever, which enabled the direct force measurements between two air bubbles and between an air bubble and a solid surface.⁴⁸⁻⁵⁴ The measured force results could be successfully described by a theoretical model based on Reynolds lubrication theory and augmented Young-Laplace equation by considering the disjoining pressure and nonlinear bubble deformation, the validity of which was later verified by the simultaneous measurements of the force and separation using AFM bubble probe combined with reflection interference contrast microscopy (RICM). The repulsive VDW interaction was found to inhibit bubble attachment on smooth hydrophilic surfaces (e.g. mica, silica and gold),⁵³⁻⁵⁶ and hydrophobic interaction played a critical role in bubble attachment on hydrophobized surface.⁵⁶

1.5 Objectives

Despite much progress achieved over the past few decades, the fundamental understanding of the interaction mechanisms at the air/water/mineral interfaces in flotation still remains incomplete, particularly at the micro- and nano-scale. Therefore, the major objective of this thesis is to investigate the surface characteristics (i.e. surface heterogeneity, electrochemical properties and bubble-particle interaction) of sulfide minerals in complex aqueous media using several complementary experimental techniques, such as AFM force mapping, electrochemical AFM, and AFM bubble probe, which will help elucidate the surface interaction mechanisms attributing to the various interfacial phenomena in mineral flotation. The detailed objectives are as follows.

(1) Probe the nanoscale heterogeneity of surface hydrophobicity and surface interactions on mineral surface before/after conditioning treatment (i.e. copper activation and xanthate adsorption) using AFM force mapping, which will provide a basic understanding of the size and distribution of hydrophobic domains on mineral surfaces as well as a feasible methodology to modulate the hydrophobic domains to improve the efficiency of fine particle flotation.

(2) Combine AFM and electrochemical setup to directly measure the evolution of surface characteristics (i.e. morphological changes and surface interactions) with the simultaneous interfacial chemical reaction on mineral surface, which will provide useful information on the electrochemical reaction mechanisms and new insights into the interaction mechanisms between hydrophilic/hydrophobic surfaces (e.g. gangue particles of different hydrophobicity) and mineral surfaces with different degrees of electrochemical oxidation.

(3) Quantify the interaction forces between air bubbles and mineral surfaces in aqueous solution to elucidate the bubble attachment mechanisms in mineral flotation. AFM bubble probe technique together with theoretical modeling will be applied to investigate the interaction forces, and impacts of hydrodynamic condition, reagent conditioning, ion concentration and ion type will be studied.

(4) Characterize the morphology of mineral surfaces and their interactions with air bubbles under the effects of polymer adsorption, which will provide nanoscopic insights into the role of polymer depressants in the bubble-mineral attachment mechanisms. The parameters to investigate include polymer concentration, ion concentration, maximum force load and contact time.

1.6 Structure of the thesis

Chapter 1 introduces the principles and challenges of mineral flotation, the interactions involved in mineral flotation, and the approach to measure the interaction forces. The objectives of this thesis are also presented.

Chapter 2 describes the experiment methods which include the preparation of mineral surfaces and the working principles of experiment techniques.

Chapter 3 demonstrates the approach to probe the nanoscale heterogeneity of surface hydrophobicity and surface interactions on sphalerite surfaces using AFM force mapping, which are compared to the water contact angle and three probe liquid methods based on a statistical average of a relatively large surface area.

Chapter 4 illustrates the approach to measure the evolution of surface characteristics (i.e. morphological changes and surface interactions) with the

simultaneous modulation of interfacial chemical reaction on galena surfaces using EC-AFM, with implication on the electrochemical reaction mechanisms and interaction mechanisms in mineral flotation.

Chapter 5 studies the feasibility of AFM bubble probe technique to measure the interaction forces between air bubbles and sphalerite surfaces in aqueous solution at the nanoscale, aiming to understand the bubble attachment mechanisms in mineral flotation.

Chapter 6 investigates the impacts of polymer adsorption on the morphology of molybdenite surfaces and their interaction with air bubbles at the nanoscale, corresponding to the bubble-mineral attachment mechanisms.

Chapter 7 presents the major conclusions and original contributions of this thesis. The suggestions for future work are also provided.

1.7 References

1. Klassen, V. I.; Mokrousov, V. A., *An Introduction to the Theory of Flotation*; Butterworths, **1963**.
2. Fuerstenau, M. C.; Jameson, G. J.; Yoon, R. H., *Froth Flotation: A Century of Innovation*; SME, **2007**.
3. Leja, J., *Surface Chemistry of Froth Flotation*; Plenum Press, **1982**.
4. Fuerstenau, M. C.; Miller, J. D.; Kuhn, M. C., *Chemistry of Flotation*; Random House Trade, **1985**.
5. Chandra, A.; Gerson, A., A Review of the Fundamental Studies of the Copper Activation Mechanisms for Selective Flotation of the Sulfide Minerals, Sphalerite and Pyrite. *Adv. Colloid Interface Sci.* **2009**, *145*, 97-110.

6. Wittstock, G.; Kartio, I.; Hirsch, D.; Kunze, S.; Szargan, R., Oxidation of Galena in Acetate Buffer Investigated by Atomic Force Microscopy and Photoelectron Spectroscopy. *Langmuir* **1996**, *12*, 5709-5721.
7. Beaussart, A.; Mierczynska-Vasilev, A.; Beattie, D. A., Adsorption of Dextrin on Hydrophobic Minerals. *Langmuir* **2009**, *25*, 9913-9921.
8. Kor, M.; Korczyk, P. M.; Addai-Mensah, J.; Krasowska, M.; Beattie, D. A., Carboxymethylcellulose Adsorption on Molybdenite: The Effect of Electrolyte Composition on Adsorption, Bubble-Surface Collisions, and Flotation. *Langmuir* **2014**, *30*, 11975-11984.
9. Liu, Q.; Zhang, Y.; Laskowski, J., The Adsorption of Polysaccharides onto Mineral Surfaces: An Acid/Base Interaction. *Int. J. Miner. Process.* **2000**, *60*, 229-245
10. Chau, T.; Bruckard, W.; Koh, P.; Nguyen, A., A Review of Factors That Affect Contact Angle and Implications for Flotation Practice. *Adv. Colloid Interface Sci.* **2009**, *150*, 106-115.
11. Farrokhpay, S., The Significance of Froth Stability in Mineral Flotation-a Review. *Adv. Colloid Interface Sci.* **2011**, *166*, 1-7.
12. Nagaraj, D.; Ravishankar, S., Flotation Reagents-a Critical Overview from an Industry Perspective. *Froth Flotation: A Century of Innovation. Society for Mining, Metallurgy, and Exploration, Littleton, Colorado* **2007**, 375-424.
13. Wang, B.; Peng, Y., The Effect of Saline Water on Mineral Flotation-a Critical Review. *Miner. Eng.* **2014**, *66*, 13-24.
14. Castro, S. In *Challenges in Flotation of Cu-Mo Sulfide Ores in Sea Water*, Water in Mineral Processing-Proc. of the First International Symposium, SME, **2012**.

15. Farrokhpay, S.; Zanin, M., An Investigation into the Effect of Water Quality on Froth Stability. *Adv. Powder. Technol.* **2012**, *23*, 493-497.
16. Miettinen, T.; Ralston, J.; Fornasiero, D., The Limits of Fine Particle Flotation. *Miner. Eng.* **2010**, *23*, 420-437.
17. Rao, K.; Chernyshova, I., Challenges in Sulphide Mineral Processing. *Open. Miner. Process. J.* **2011**, *4*, 7-13.
18. Castro, S.; Laskowski, J. S., Froth Flotation in Saline Water. *KONA. Powder. Part. J.* **2011**, *29*, 4-15.
19. Moreno, P. A.; Aral, H.; Cuevas, J.; Monardes, A.; Adaro, M.; Norgate, T.; Bruckard, W., The Use of Seawater as Process Water at Las Luces Coppe-Molybdenum Beneficiation Plant in Taltal (Chile). *Miner. Eng.* **2011**, *24*, 852-858.
20. Du, H.; Miller, J. D., Interfacial Water Structure and Surface Charge of Selected Alkali Chloride Salt Crystals in Saturated Solutions: A Molecular Dynamics Modeling Study. *J. Phys. Chem. C* **2007**, *111*, 10013-10022.
21. Wang, J.; Xie, L.; Liu, Q.; Zeng, H., Effects of Salinity on Xanthate Adsorption on Sphalerite and Bubble-Sphalerite Interactions. *Miner. Eng.* **2015**, *77*, 34-41.
22. Craig, V.; Ninham, B.; Pashley, R., Effect of Electrolytes on Bubble Coalescence. *Nature* **1993**, *364*, 317-319.
23. Hewitt, D.; Fornasiero, D.; Ralston, J., Bubble Particle Attachment Efficiency. *Miner. Eng.* **1994**, *7*, 657-665.
24. Wang, W.; Zhou, Z.; Nandakumar, K.; Masliyah, J. H.; Xu, Z., An Induction Time Model for the Attachment of an Air Bubble to a Hydrophobic Sphere in Aqueous Solutions. *Int. J. Miner. Process.* **2005**, *75*, 69-82.

25. Ahmed, N.; Jameson, G., The Effect of Bubble Size on the Rate of Flotation of Fine Particles. *Int. J. Miner. Process.* **1985**, *14*, 195-215.
26. Yoon, R.; Luttrell, G., The Effect of Bubble Size on Fine Particle Flotation. *Min. Proc. Ext. Met. Rev.* **1989**, *5*, 101-122.
27. Dai, Z.; Fornasiero, D.; Ralston, J., Particle-Bubble Attachment in Mineral Flotation. *Int. J. Miner. Process.* **1999**, *217*, 70-76.
28. Matis, K.; Gallios, G.; Kydros, K., Separation of Fines by Flotation Techniques. *Separ. Technol.* **1993**, *3*, 76-90.
29. Zhou, Z.; Xu, Z.; Finch, J., On the Role of Cavitation in Particle Collection During Flotation-a Critical Review. *Miner. Eng.* **1994**, *7*, 1073-1084.
30. Mishchuk, N.; Ralston, J.; Fornasiero, D., Influence of Very Small Bubbles on Particle/Bubble Heterocoagulation. *J. Colloid Interface Sci.* **2006**, *301*, 168-175.
31. Israelachvili, J. N., *Intermolecular and Surface Forces*; Academic Press: London, **1991**.
32. Cheng, Y. T.; Rodak, D.; Wong, C.; Hayden, C., Effects of Micro-and Nano-Structures on the Self-Cleaning Behaviour of Lotus Leaves. *Nanotechnology* **2006**, *17*, 1359.
33. Sánchez-Iglesias, A.; Grzelczak, M.; Altantzis, T.; Goris, B.; Perez-Juste, J.; Bals, S.; Van Tendeloo, G.; Donaldson Jr, S. H.; Chmelka, B. F.; Israelachvili, J. N., Hydrophobic Interactions Modulate Self-Assembly of Nanoparticles. *ACS nano* **2012**, *6*, 11059-11065.
34. Meyer, E. E.; Rosenberg, K. J.; Israelachvili, J., Recent Progress in Understanding Hydrophobic Interactions. *Proc. Natl. Acad. Sci. U. S. A.* **2006**, *103*, 15739-15746.
35. Zeng, H.; Shi, C.; Huang, J.; Li, L.; Liu, G.; Zhong, H., Recent Experimental

Advances on Hydrophobic Interactions at Solid/Water and Fluid/Water Interfaces. *Biointerphases* **2016**, *11*, 018903.

36. Butt, H.-J.; Cappella, B.; Kappl, M., Force Measurements with the Atomic Force Microscope: Technique, Interpretation and Applications. *Surf. Sci. Rep.* **2005**, *59*, 1-152.

37. Binnig, G.; Quate, C. F.; Gerber, C., Atomic Force Microscope. *Phys. Rev. Lett.* **1986**, *56*, 930.

38. Cappella, B.; Dietler, G., Force-Distance Curves by Atomic Force Microscopy. *Surf. Sci. Rep.* **1999**, *34*, 1-104.

39. Hinterdorfer, P.; Dufrêne, Y. F., Detection and Localization of Single Molecular Recognition Events Using Atomic Force Microscopy. *Nature methods* **2006**, *3*, 347-355.

40. Katan, A. J.; Van Es, M. H.; Oosterkamp, T. H., Quantitative Force Versus Distance Measurements in Amplitude Modulation Afm: A Novel Force Inversion Technique. *Nanotechnology* **2009**, *20*, 165703.

41. Ducker, W. A.; Senden, T. J.; Pashley, R. M., Direct Measurement of Colloidal Forces Using an Atomic Force Microscope. *Nature* **1991**, *353*, 239-241.

42. Butt, H.-J., A Technique for Measuring the Force between a Colloidal Particle in Water and a Bubble. *J. Colloid Interface Sci.* **1994**, *166*, 109-117.

43. Gillies, G.; Kappl, M.; Butt, H.-J., Direct Measurements of Particle–Bubble Interactions. *Adv. Colloid Interface Sci.* **2005**, *114*, 165-172.

44. Johnson, D. J.; Miles, N. J.; Hilal, N., Quantification of Particle–Bubble Interactions Using Atomic Force Microscopy: A Review. *Adv. Colloid Interface Sci.* **2006**, *127*, 67-81.

45. Ducker, W. A.; Xu, Z.; Israelachvili, J. N., Measurements of Hydrophobic and DLVO Forces in Bubble-Surface Interactions in Aqueous Solutions. *Langmuir* **1994**, *10*, 3279-

3289.

46. Fielden, M. L.; Hayes, R. A.; Ralston, J., Surface and Capillary Forces Affecting Air Bubble-Particle Interactions in Aqueous Electrolyte. *Langmuir* **1996**, *12*, 3721-3727.

47. Attard, P.; Miklavcic, S. J., Effective Spring Constant of Bubbles and Droplets. *Langmuir* **2001**, *17*, 8217-8223.

48. Chan, D. Y.; Klaseboer, E.; Manica, R., Film Drainage and Coalescence between Deformable Drops and Bubbles. *Soft Matter* **2011**, *7*, 2235-2264.

49. Tabor, R. F.; Grieser, F.; Dagastine, R. R.; Chan, D. Y., Measurement and Analysis of Forces in Bubble and Droplet Systems Using Afm. *J. Colloid Interface Sci.* **2012**, *371*, 1-14.

50. Dagastine, R. R.; Manica, R.; Carnie, S. L.; Chan, D.; Stevens, G. W.; Grieser, F., Dynamic Forces between Two Deformable Oil Droplets in Water. *Science* **2006**, *313*, 210-213.

51. Vakarelski, I. U.; Manica, R.; Tang, X.; O'Shea, S. J.; Stevens, G. W.; Grieser, F.; Dagastine, R. R.; Chan, D. Y., Dynamic Interactions between Microbubbles in Water. *Proc. Natl. Acad. Sci. U. S. A.* **2010**, *107*, 11177-11182.

52. Tabor, R. F.; Chan, D. Y.; Grieser, F.; Dagastine, R. R., Anomalous Stability of Carbon Dioxide in Ph-Controlled Bubble Coalescence. *Angew. Chem., Int. Ed.* **2011**, *50*, 3454-3456.

53. Manor, O.; Vakarelski, I. U.; Tang, X.; O'Shea, S. J.; Stevens, G. W.; Grieser, F.; Dagastine, R. R.; Chan, D. Y., Hydrodynamic Boundary Conditions and Dynamic Forces between Bubbles and Surfaces. *Phys. Rev. Lett.* **2008**, *101*, 024501.

54. Tabor, R. F.; Manica, R.; Chan, D. Y.; Grieser, F.; Dagastine, R. R., Repulsive Van

Der Waals Forces in Soft Matter: Why Bubbles Do Not Stick to Walls. *Phys. Rev. Lett.* **2011**, *106*, 064501.

55. Manor, O.; Vakarelski, I. U.; Stevens, G. W.; Grieser, F.; Dagastine, R. R.; Chan, D. Y., Dynamic Forces between Bubbles and Surfaces and Hydrodynamic Boundary Conditions. *Langmuir* **2008**, *24*, 11533-11543.

56. Shi, C.; Chan, D. Y.; Liu, Q.; Zeng, H., Probing Hydrophobic Interaction between Air Bubble and Partially Hydrophobic Surfaces Using Atomic Force Microscopy. *J. Phys. Chem. C* **2014**, *118*, 25000-25008.

Chapter 2 Experimental Methods

2.1 Preparation of mineral surfaces

Sphalerite was fractured to obtain the natural cleavage surface that was then glued onto a freshly cleaved mica surface with the fractured face exposed for testing. To remove surface oxidation layer, the freshly fractured sphalerite surface was washed in 0.01 M HCl solution for 5 minutes, rinsed by Milli-Q water, and then dried using high purity nitrogen.¹⁻² Sphalerite is not sufficiently hydrophobic for spontaneous attachment to air bubbles in the absence of conditioning treatment; therefore, 0.1 mM CuSO₄ solution and 0.5 mM PAX solution were used as activator and collector, respectively, to enhance the surface hydrophobicity of sphalerite.

Galena was fractured to obtain the natural cleavage surface that was then cleaned using high purity nitrogen to remove loosely attached galena fragments. The cleaved galena surface was glued onto a conductive metal disk by silver conductive epoxy to ensure good electrical contact, and the insulating epoxy was then applied to cover the conductive metal disk with only the galena surface exposed for electrochemical experiments.

The natural cleavage surface of molybdenite was obtained by peeling off the top layers using a sticky tape. Polymer stock solutions with the concentration of 500 ppm were prepared by dissolving appropriate mass of guar gum in Milli-Q water under stirring overnight to ensure complete hydration. Solutions of desired concentration (i.e. 1 ppm, 5 ppm, 10 ppm and 50 ppm) were prepared by diluting the stock solution in Milli-Q water and fixing solution pH at 9. The freshly exfoliated molybdenite basal plane was

conditioned in the desired polymer solutions for 30 min, rinsed by Milli-Q water, and then dried using high-purity nitrogen prior to measurements.

2.2 Surface characterization

A contact angle goniometer (ramé-hart instrument Co., NJ, USA) was used to measure the static/advancing/receding water contact angle of mineral surfaces using a sessile drop method. For the same type of sample, at least two different surfaces and three different positions on each surface were tested, and the average water contact angle was reported. A water droplet was placed onto the mineral surface through a microsyringe to determine the static water contact angle with a microscope. As a small dispensation volume was continuously applied to increase/decrease the droplet volume, the water contact angle correspondingly increased/decreased with the three-phase contact line (TPCL) remaining stationary. The contact angle that the water droplet held immediately before advancing outward/inward is referred to as the advancing/receding contact angle, and the difference between the advancing contact angle and receding contact angle is referred to as contact angle hysteresis.

The elemental compositions of mineral surfaces were characterized by cryo-XPS spectra using an AXIS 165 spectroscopy system (Kratos Analytical Ltd, UK) equipped with a monochromatized Al K α X-ray source ($h\nu = 1486.6$ eV). The precooled surfaces (~ 130 K) were transferred to the analytical chamber when the vacuum in the fast entry lock was better than 2×10^{-6} Torr and the temperature in the analytical chamber was kept at ~ 130 K. During the measurements, the base pressure in the analytical chamber was lower than 1×10^{-9} Torr. The survey scans were collected for binding energy spanning

from 1100 to 0 eV with analyzer pass energy of 160 eV and a step of 0.4 eV. For high resolution spectra, the pass energy was 20 eV with a step of 0.1 eV. Surface charging was compensated by taking the C 1s peak of background hydrocarbon at 284.8 eV as an internal standard.

A Zetasizer Nano (Malvern Instruments Ltd., United Kingdom) was used to measure the zeta potential of mineral suspension under different solution conditions. A MFP-3D AFM (Asylum Research, Santa Barbara, CA, USA) was used to characterize the height and phase images of mineral surfaces.

2.3 Preparation of AFM bubble probe

The AFM bubble probe was prepared by picking up an air bubble of suitable size (typically 60-90 μm radius) with a custom-made rectangular silicon cantilever (400 \times 70 \times 2 μm). Prior to the preparation of AFM bubble probe, the glass disk of a fluid cell and AFM cantilever were hydrophobized following an established method.³⁻⁵ Specifically, the glass disk of the fluid cell was mildly hydrophobized by immersing in 10 mM octadecyltrichlorosilane (OTS) in toluene for \sim 10 s to give a water contact angle of 40 $^\circ$ -60 $^\circ$ for bubble immobilization, and AFM cantilevers with a circular gold patch (diameter 65 μm , thickness 30 nm) were strongly hydrophobized by immersing in 10 mM dodecanethiol in absolute ethanol overnight to provide higher hydrophobicity than the glass disk for bubble anchoring. The air bubbles were generated and immobilized on the glass disk by carefully purging air through a custom-made ultra-sharp glass pipette into aqueous solution. After bubble anchoring on the AFM cantilever, the cantilever-attached

bubble was positioned over mineral surface and then driven to approach the surface until a fixed deflection of the cantilever was reached or bubble attachment occurred.

2.4 References

1. Teng, F.; Liu, Q.; Zeng, H., In Situ Kinetic Study of Zinc Sulfide Activation Using a Quartz Crystal Microbalance with Dissipation (QCM-D). *J. Colloid Interface Sci.* **2012**, *368*, 512-520.
2. Deng, M., Impact of Gypsum Supersaturated Solution on the Flotation of Sphalerite. University of Alberta, **2013**.
3. Xie, L.; Shi, C.; Wang, J.; Huang, J.; Lu, Q.; Liu, Q.; Zeng, H., Probing the Interaction between Air Bubble and Sphalerite Mineral Surface Using Atomic Force Microscope. *Langmuir* **2015**, *31*, 2438-2446.
4. Shi, C.; Cui, X.; Xie, L.; Liu, Q.; Chan, D. Y.; Israelachvili, J. N.; Zeng, H., Measuring Forces and Spatiotemporal Evolution of Thin Water Films between an Air Bubble and Solid Surfaces of Different Hydrophobicity. *ACS nano* **2014**, *9*, 95-104.
5. Cui, X.; Shi, C.; Xie, L.; Liu, J.; Zeng, H., Probing Interactions between Air Bubble and Hydrophobic Polymer Surface: Impact of Solution Salinity and Interfacial Nanobubbles. *Langmuir* **2016**, *32*, 11236–11244.

Chapter 3 Mapping Nanoscale Heterogeneity of Surface Hydrophobicity on Sphalerite Mineral

3.1 Introduction

Hydrophobic effect plays an important role in a wide range of natural phenomena and engineering applications such as protein folding,¹⁻² self-assembly,³⁻⁶ and mineral flotation.⁷⁻⁸ Protein folding is an inherently heterogeneous process in which unfolded structures are connected into the unique native conformation through microscopic pathways.⁹ Most materials exhibit inherently heterogeneous nature with hydrophilic and hydrophobic compositions. Typically, the hydrophobic moieties of amphiphilic molecules can induce self-assembly in aqueous medium into structures like micelles and vesicles via hydrophobic interaction. In froth flotation in minerals engineering, the non-uniform adsorption of collectors on mineral surfaces generally leads to the heterogeneous distribution of hydrophilic and hydrophobic domains, which has a particularly important influence on surface interactions of mineral particles. Nevertheless, much attention has been focused on the average surface wettability based on a statistical average of either a large number of mineral particles or a large area of mineral surface,¹⁰⁻¹² and the basic understanding of hydrophobicity distribution on mineral surfaces still remains limited, particularly for the surface interactions on the hydrophilic and hydrophobic domains.

Surface heterogeneity of mineral particles is common in nature from macroscale to nanoscale, which may arise from the association with other minerals in ore deposits as well as the crystal defect ranging from missing or misplaced atoms to interstitial impurity atoms in crystal lattice.¹³⁻¹⁴ Sulfide minerals are an economically important class of

minerals, most of which are hydrophilic in nature. Thus, short-chain collectors (e.g. xanthates) are widely used to enhance the surface hydrophobicity of sulfide minerals. The chemical heterogeneity of sulfide minerals normally induces non-uniform adsorption of collectors on mineral surfaces, thereby resulting in the heterogeneous distribution of hydrophilic and hydrophobic domains. Over the last few decades, much effort has been made to characterize the adsorption of collectors on mineral surfaces, most of which used analytic tools such as Fourier transform infrared spectroscopy (FTIR),¹⁵⁻¹⁶ X-ray photoelectron spectroscopy (XPS),¹⁷⁻¹⁸ and Raman spectroscopy.¹⁹⁻²⁰ But such surface characterizations are generally geared towards an understanding of the bonding between the collectors and minerals, and could not directly provide spatial distribution of adsorbed xanthates and surface hydrophobicity, particularly at nanoscale.

Time of flight secondary ion mass spectrometry (ToF-SIMS) as a surface sensitive technique has been successfully applied to detect and map the heterogeneous distribution of chemical species on mineral surfaces.²¹⁻²³ Based on quantification of surface species, the hydrophilic and hydrophobic species in the different stages of mineral processing (e.g. concentrate and tail streams) were statistically compared,²⁴ and surface species contributing the most to the hydrophobicity variations (i.e. oxygen, sulfur, and collector fragment) were statistically correlated to contact angle of mineral surfaces.²⁵ Scanning electrochemical microscopy (SECM) is another technique used to probe the variation of faradaic current and surface reactivity as an ultramicroelectrode tip is moved across the substrate.²⁶ The recent application of SECM technique was able to in situ monitor the heterogeneous transformation of surface species on sphalerite during conditioning treatment, revealing that copper activation of sphalerite strongly depends on

surface heterogeneity which directly impacts the subsequent xanthate adsorption process.²⁷ However, the relatively low spatial resolution of ToF-SIMS elemental mapping and SECM imaging limits the identification of hydrophobicity distribution at nanoscale. Also, ToF-SIMS is not an in situ measurement technique so that surface alteration may occur during sample preparation.

Atomic force microscopy (AFM) has been extensively used to characterize surface properties and directly measure intermolecular and surface forces of different materials at the nanoscale.^{7-8, 28-36} The developed chemical force microscopy (CFM) technique enables direct measurements of intermolecular forces and adhesion between AFM tips and solid surfaces modified with self-assembled monolayers (SAMs) with well-defined terminal groups such as -CH₃, -CH₂OH and -COOH as well as biological surfaces.³⁷⁻⁴² Based on the CFM technique, the hydrophobized AFM tips (e.g. functionalized with -CH₃ groups) could be used to quantify the local surface hydrophobicity on mineral surfaces. To date, the distribution of surface hydrophobicity and surface interactions of the hydrophilic/hydrophobic domains on mineral surfaces at the nanoscale, to our knowledge, have not been reported.

In this work, the nanoscale heterogeneity of surface hydrophobicity (viz. distribution of hydrophilic and hydrophobic domains) on sphalerite mineral surface before/after treatment with chemical reagents (e.g. copper activation and xanthate adsorption) was directly mapped using AFM force measurements. The classical Derjaguin-Landau-Verwey-Overbeek (DLVO) model or extended DLVO model by including the hydrophobic effect was used to analyze the measured force-separation curves on different domains. The Derjaguin-Muller-Toporov (DMT) model coupled with

Van Oss-Chaudhury-Good (VCG) theory was applied to analyze the adhesion measured during retraction. Cryo-XPS analysis and water contact angle measurements were also conducted to provide complementary information for a better understanding of chemical composition and xanthate coverage on sphalerite surface. This work provides useful information on the heterogeneous distribution of surface hydrophobicity at the nanoscale, and insights into surface interaction mechanisms of different hydrophobic/hydrophilic domains of mineral surfaces in flotation process.

3.2 Materials and methods

3.2.1 Materials

Sodium chloride (NaCl, ACS reagent grade), cupric sulfate pentahydrate ($\text{CuSO}_4 \cdot 5\text{H}_2\text{O}$, ACS reagent grade), diiodomethane (CH_2I_2 , ACS reagent grade), ethylene glycol ($\text{C}_2\text{H}_6\text{O}_2$, ACS reagent grade) and glycerol ($\text{C}_3\text{H}_8\text{O}_3$, ACS reagent grade) were purchased from Fisher Scientific and used as received without further purification. Potassium amyl xanthate (PAX, $\text{C}_6\text{H}_{11}\text{OS}_2\text{K}$, Prospec Chemicals Ltd., Canada) was purified by adding 100 g of xanthate into 1 L of acetone under stirring at 40°C for several minutes and then precipitated in ether following an established method.^{7,27} Hydrochloric acid (HCl, ACS reagent grade) and sodium hydroxide (NaOH, ACS reagent grade) were purchased from Fisher Scientific and used to adjust solution pH. In this work, all the aqueous solutions were prepared using Milli-Q water (Millipore deionized, $18.2 \text{ M}\Omega \cdot \text{cm}$ resistivity) and the pH was fixed at 5.

3.2.2 Preparation of sphalerite surface

Sphalerite (Ward's Science, NY, USA) was fractured to obtain the natural cleavage surface which was then glued onto a freshly cleaved mica surface by epoxy with the fractured face exposed for measurements. The freshly fractured sphalerite surface was washed in 0.01 M HCl solution for 5 minutes, rinsed by Milli-Q water, and then dried by high purity nitrogen to remove surface oxidation layer.⁷

Chemical reagents such as copper sulfate and short-chain xanthate are widely used as activator and collector, respectively, to enhance the surface hydrophobicity of sphalerite since sphalerite is not sufficiently hydrophobic for spontaneous bubble attachment in the absence of activation and collector treatment.⁴³ Herein, sphalerite surface conditioned in 0.1 mM $\text{CuSO}_4 \cdot 5\text{H}_2\text{O}$ solution at pH 5 for 5 minutes and subsequently in 0.5 mM PAX solution at pH 5 for 5 minutes, was denoted as “conditioned sphalerite”.

3.2.3 Surface characterization

The elemental compositions of sample surfaces were characterized by cryo-XPS electron binding energy spectra using an AXIS 165 spectroscopy system (Kratos Analytical Ltd, UK) equipped with a monochromatized Al K α X-ray source ($h\nu = 1486.6$ eV). The samples precooled at ~ 130 K were transferred to the analytical chamber as the vacuum in the fast entry lock was better than 2×10^{-6} Torr and the temperature in the analytical chamber was ~ 130 K. The base pressure in the analytical chamber was lower than 1×10^{-9} Torr during the measurements. The survey scans were collected for binding energy spanning from 1100 to 0 eV with analyzer pass energy of 160 eV and a step of 0.4

eV. For high resolution spectra, the pass energy was 20 eV with a step of 0.1 eV. Due to the poor conductivity of measured surfaces, charge neutralization was applied to stabilize the spectra. Sample charging was compensated by taking the C 1s peak of background hydrocarbon at 284.8 eV as an internal standard.

A contact angle goniometer (ramé-hart instrument co., NJ, USA) was used to measure the static/advancing/receding water contact angles on sample surfaces using a sessile drop method. For each type of surface, at least two sample surfaces and three different positions on the same surface were tested, and the average water contact angle was reported. A water droplet of 3 μL was placed onto sample surfaces through a microsyringe, and the drop shape was captured and analyzed with a microscope to determine the static water contact angle. Advancing/receding contact angles were measured as a dispensation volume of 0.25 μL was applied to continuously increase/decrease the drop volume. The difference between the advancing contact angle and receding contact angle is taken as contact angle hysteresis.

3.2.4 Adhesion force mapping

The schematic of adhesion force mapping for simultaneously probing the topographic image and adhesion map of sample surfaces is shown in Figure 3.1. Prior to adhesion force mapping measurements, gold-coated AFM tips were cleaned by UV/ozone treatment and then hydrophobized by immersing in 10 mM dodecanethiol in absolute ethanol overnight. After self-assembly, the prepared AFM tips were rinsed by ethanol to remove physisorbed thiols and dried using high purity slow-flowing nitrogen. The surface hydrophobicity of the treated AFM tips was evaluated by measuring the average water

contact angle on AFM cantilevers, which showed an average water contact angle of $\sim 105^\circ$ on thiol-functionalized cantilevers. Adhesion force mapping was performed on sample surfaces with thiol-functionalized AFM tips in 0.5 M NaCl using an MFP-3D AFM (Asylum Research, Santa Barbara, CA, USA). By scanning the hydrophobic tip across sample surfaces using piezoelectric scanners, a two-dimensional array of force curves at 20×20 points (400 consecutive force-separation measurements) were acquired on at least three different positions of the sample surface with an area of $2 \times 2 \mu\text{m}^2$ and at least two sample surfaces of the same type. For each force-separation curve, the tip was driven to approach and then retract from the surface with constant velocity and loading force. The deflection of the cantilever was detected through a laser beam that was reflected from the cantilever into a split photodiode detector, which was further converted to force using the spring constant and Hooke's law. The spring constants of the cantilevers were determined to be 0.1-0.2 N/m using the Hutter and Bechhoefer method.⁴⁴

3.2.5 Force curve analysis

To interpret the measured AFM force-separation curves on the sample surfaces, theoretical analysis based on the classical DLVO model or extended DLVO model by including the hydrophobic effect was applied. As shown in previous report,⁴⁵ the pyramidal geometry of AFM tip was reasonably assumed to be conical with a spherical cap at the apex, and the geometry and parameters used for the theoretical calculations are illustrated in the inset of Figure 3.1, where α is the geometry angle for spherical cap, R is the radius of spherical cap, r is the radius of the circle of the tip at a given vertical position, and D is the distance between the tip end and mineral surface.

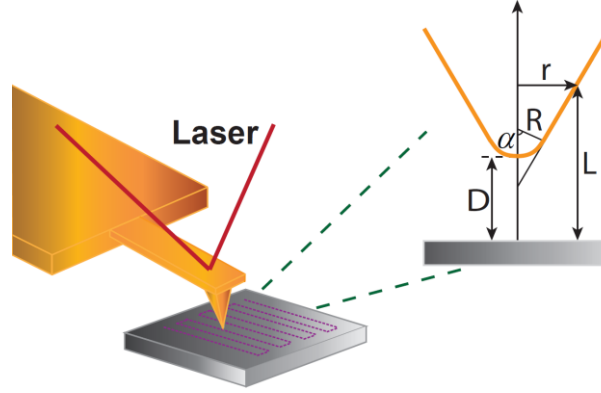


Figure 3.1 The schematic of AFM adhesion force mapping on mineral surface. Inset figure shows the geometry of conical AFM tip with a spherical cap at the apex, where α is the geometry angle for spherical cap, R is the radius of spherical cap, r is the radius of the circle of the tip at a given vertical position, D is the distance between the tip end and mineral surface.

Adhesion force mapping in this work was conducted in 0.5 M NaCl, so the contribution of electrical double layer (EDL) interaction is significantly suppressed. The van der Waals (VDW) interaction between AFM tip and flat substrate F_{VDW} can be given by Equation 3.1, where A_H is the non-retarded Hamaker constant and $L_1 = D + R(1 - \cos \alpha)$.⁴⁵

$$F_{VDW} = \frac{A_H}{6} \left[\frac{R + D - 2L_1}{L_1^2} - \frac{R - D}{D^2} \right] - \frac{A_H}{3 \tan^2 \alpha} \left(\frac{1}{L_1} + \frac{R \sin \alpha \tan \alpha - D - R(1 - \cos \alpha)}{2L_1^2} \right) \quad (3.1)$$

Hydrophobic interaction F_{HB} was reported to follow an exponential equation as shown in Equation 3.2,^{8, 46} where C is a constant (N/m) and D_0 is the decay length of hydrophobic interaction.⁴⁷

$$F_{HB} = -CRe^{-D/D_0} \quad (3.2)$$

The geometry of thiol-functionalized AFM tips was determined by JAMP-9500F Field Emission Auger Microprobe (JEOL, MA, USA) equipped with Schottky field emitter that produces electron probe diameter of 3-8 nm. Based on the analysis of FE-SEM images of the tip (illustrated in Figure 3.2) by ImageJ software following an established method,^{8, 30} the geometry angle for spherical cap α and the radius of the spherical cap R could be determined. Typical R values ranged from 26 to 32 nm. For a typical case, R was determined to be ~ 28.6 nm and α was measured as $\sim 61.2^\circ$.

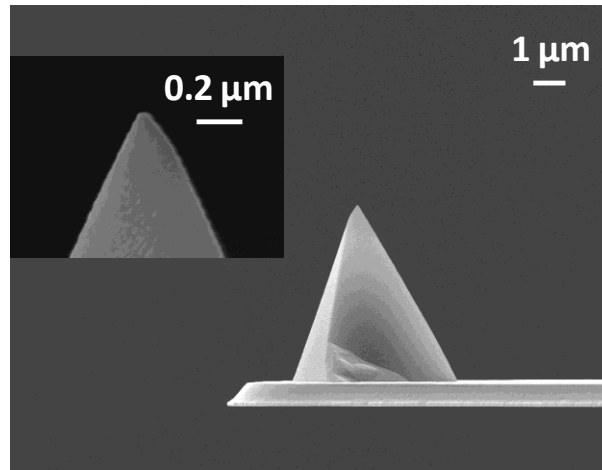


Figure 3.2 Typical FE-SEM images for analysis of the geometry of thiol-functionalized AFM tips.

3.2.6 Surface energy measurement

The surface energy of samples was determined by three-probe-liquid method.⁴⁸ Typically, a contact angle goniometer was used to measure the static contact angles of three probing liquids, including one nonpolar (i.e. diiodomethane) and two polar (i.e. ethylene glycol and glycerol) liquids, on sample surfaces. Surface energy γ with

Lifshitz-van der Waals γ^{LW} and Lewis acid-base γ^{AB} (electron acceptor γ^+ and electron donor γ^-) components can be calculated by a method developed by van Oss et al. (Equation 3.3).⁴⁸

$$\gamma = \gamma^{LW} + \gamma^{AB} = \gamma^{LW} + 2\sqrt{\gamma^+ \gamma^-} \quad (3.3)$$

By substituting contact angles of these three types of liquids on the sample surfaces θ_L into Equation 3.4, the Lewis acid-base, electron acceptor and electron donor components of the surfaces can be obtained, where the subscript *S* or *L* represents solid or liquid, respectively.⁴⁸

$$\gamma_L (\cos \theta_L + 1) = 2\sqrt{\gamma_S^{LW} \gamma_L^{LW}} + 2\sqrt{\gamma_S^+ \gamma_L^-} + 2\sqrt{\gamma_S^- \gamma_L^+} \quad (3.4)$$

3.3 Results and discussion

3.3.1. Cryo-XPS

XPS analysis is a surface sensitive technique that provides the chemical information of surface species, such as elemental composition and chemical state, with a depth of a few nanometers. The low temperature (~130 K) of cryo-XPS enables the detection of volatile species such as elemental sulfur and dixanthogen.^{8, 49} The S 2p and C 1s binding energy spectra of sphalerite and conditioned sphalerite are compared in Figure 3.3. As shown in Figures 3.3A and 3.3B, sphalerite has only one doublet with S 2p at 161.3 eV that is attributed to the sulfur in zinc sulfide. After conditioning treatment, another doublet with S 2p at 162.8 eV corresponding to the sulfur in adsorbed collector species (e.g. chemisorbed xanthate, metal-xanthate or dixanthogen) is detected, in addition to the doublet of zinc sulfide, which agrees very well with previous reports.⁴⁹

In Figure 3.3C, the C 1s spectrum of sphalerite is composed of three peaks at 284.8 eV (C 1s I), 286.5 eV (C 1s II) and 288.5 eV (C 1s III), which arise from adventitious hydrocarbon contaminations.⁴⁹ Besides these three peaks, conditioned sphalerite has the fourth peak at 287.8 eV (C 1s IV in Figure 3.3D) that was reported to originate from the carbon in adsorbed collector species (e.g. CSS⁻ or dixanthogen).⁴⁹⁻⁵¹ Therefore, it is evident from XPS spectra that xanthate adsorption during conditioning treatment has changed the surface chemistry of mineral particles.

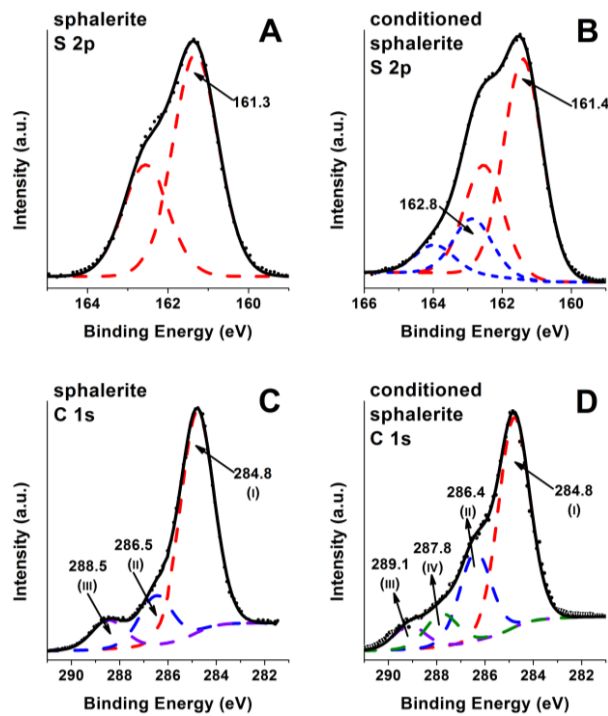


Figure 3.3 Cryo-XPS spectra of S 2p for (A) sphalerite and (B) conditioned sphalerite, and C 1s for (C) sphalerite and (D) conditioned sphalerite.

3.3.2 Contact angle measurements

The average static/advancing/receding water contact angle and contact angle hysteresis of sphalerite and conditioned sphalerite are shown in Table 3.1. Sphalerite

surface is relatively hydrophilic with static water contact angle of $\sim 34.5^\circ$, while static water contact angle of conditioned sphalerite surface rises to $\sim 84.6^\circ$, suggesting that the mineral surface becomes much more hydrophobic after conditioning treatment due to the adsorption of xanthate.⁴³

Table 3.1 The average static/advancing/receding water contact angle and contact angle hysteresis of sphalerite and conditioned sphalerite

Mineral	Static	Advancing	Receding	Hysteresis
sphalerite	34.5°	41.6°	20.5°	21.1°
conditioned sphalerite	84.6°	86.9°	40.1°	46.8°

The measurement of receding water contact angle could be considered as a process of water replacement by air at mineral-solution interfaces, which is similar to the attachment process of air bubble and mineral surface in aqueous solution. Receding water contact angle of sphalerite surface significantly increases from $\sim 20.5^\circ$ to $\sim 40.1^\circ$ after conditioning treatment, indicating that a decreased ratio of hydrophilic domain on mineral surface could facilitate the drainage of water-air-solid three-phase contact line (TPCL). The increased advancing water contact angle from $\sim 41.6^\circ$ to $\sim 86.9^\circ$, on the other hand, suggests that an increased ratio of hydrophobic domain could hold back the spreading of TPCL.

Contact angle hysteresis is closely associated with surface roughness and chemical heterogeneity.⁵² The sphalerite surface before/after conditioning treatment has a root-mean-square roughness of ~ 0.3 nm and ~ 0.5 nm, respectively. Therefore the significant rise of contact angle hysteresis from $\sim 21.1^\circ$ to $\sim 46.8^\circ$ after conditioning

treatment is most likely originated from the enhanced chemical heterogeneity. The non-uniform adsorption of xanthate results in the heterogeneous distribution of hydrophilic domain (without xanthate adsorption) and hydrophobic domain (with xanthate adsorption). Cassie-Baxter model, a widely used model to predict the apparent water contact angle of a chemically heterogeneous surface, can be applied to calculate surface coverage of xanthate on conditioned sphalerite.⁴⁶ Assuming that the region with xanthate adsorption accounts for a surface area fraction ϕ , the hydrophobic domain with water contact angle θ_{HB} has a surface area fraction ϕ , and in response, the hydrophilic domain with water contact angle θ_{HL} has a surface area fraction $1-\phi$. The apparent water contact angle $\theta_{apparent}$ for the chemically heterogeneous surface of the conditioned sphalerite can be given by Equation 3.5.⁴⁶

$$\cos \theta_{apparent} = \phi \cos \theta_{HB} + (1-\phi) \cos \theta_{HL} \quad (3.5)$$

where θ_{HL} and $\theta_{apparent}$ are the water contact angles on sphalerite and conditioned sphalerite with the measured value of 84.6° and 34.5° , respectively. θ_{HB} could be understood as the water contact angle of solid surface fully covered with xanthate. Herein, gold surface could be approximately considered to be fully covered with xanthate via the formation of SAMs. By immersing gold-coated mica surface in 0.5 mM PAX solution overnight after UV/ozone treatment, θ_{HB} was measured to be 92.5° , and thereby surface coverage of xanthate ϕ was calculated to be 84.1%. It is worth noting that contact angle measurements are based on a statistical average of a large area along water-air-solid TPCL, which are not able to precisely predict the local surface coverage of xanthate and distribution of surface hydrophobicity at the nanoscale.

3.3.3 Adhesion force mapping

The AFM adhesion force mapping, acquired as a two-dimensional array of force curves in 0.5 M NaCl using the hydrophobic AFM tip, can be demonstrated as a map of surface adhesion. The topographic images and corresponding adhesion maps of sphalerite before/after conditioning treatment are shown in Figure 3.4. The morphology and force-separation curve have been recorded simultaneously at intervals of every 100 nm to better illustrate surface roughness of the $2 \times 2 \mu\text{m}^2$ region probed by adhesion force mapping. Adhesion can be significantly affected by surface roughness due to its high dependence on the contact area between the tip and the substrate.^{46, 53} As shown in Figures 3.4A and 3.4C, the root-mean-square (rms) roughness of both sphalerite and conditioned sphalerite surfaces is lower than 0.5 nm, which is much smaller than the radius of the spherical cap of the tip (~ 28.6 nm), indicating that nanoscale surface roughness has a negligible influence on adhesion here. Hence, the measured adhesion is highly related to surface interactions including VDW interaction, EDL interaction, and possibly hydrophobic effect. In this work, the NaCl concentration was fixed at 0.5 M, under which the EDL interaction could be significantly suppressed. It is noted that the contribution of VDW interaction to the adhesion should not change significantly between the hydrophobic AFM tip and sphalerite surface before/after conditioning treatment since the adsorbed xanthate layer is very thin (~ 1 nm).⁷ Therefore, the variation of adhesion should be most likely contributed by “hydrophobic” attraction. Generally, the adhesion of the hydrophobic AFM tip on hydrophobic domain is much stronger than that on hydrophilic domain due to the hydrophobic effect.

In Figures 3.4B and 3.4D, the bright region of adhesion maps that is assigned to high adhesion corresponds to hydrophobic domain, while the dark region that is assigned to low adhesion corresponds to hydrophilic domain. The adhesion map of sphalerite surface in Figure 3.4B shows very weak adhesion over the scanned region, indicating that sphalerite has a hydrophilic surface with a homogeneous surface hydrophobicity. After conditioning treatment, the bright and dark regions of the adhesion map are unevenly distributed as shown in Figure 3.4D, suggesting that conditioned sphalerite becomes partially hydrophobic with a heterogeneous pattern due to non-uniform adsorption of xanthate.

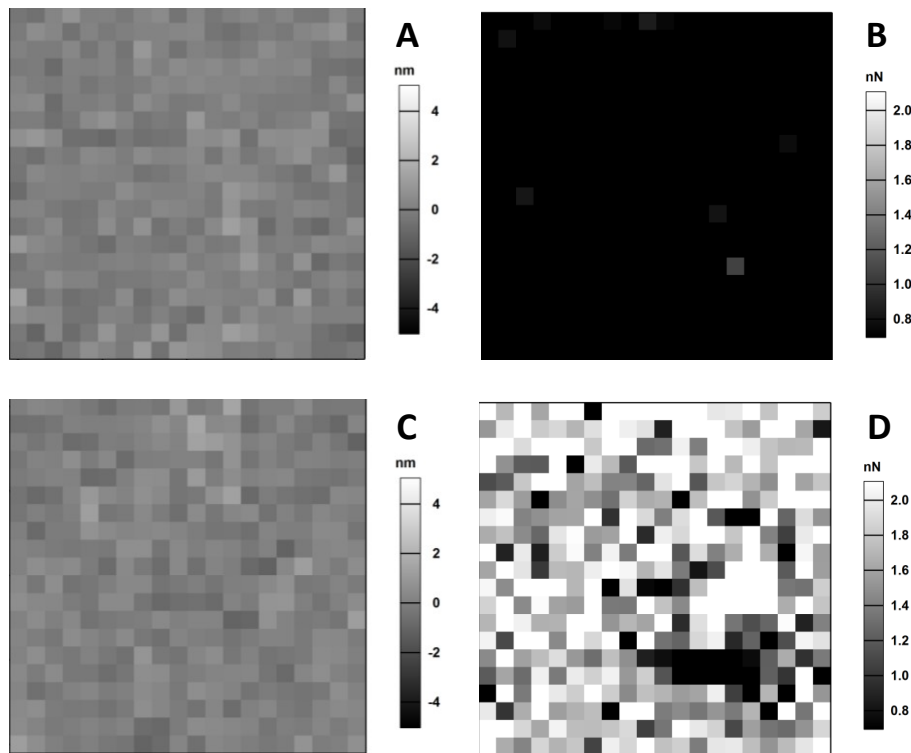


Figure 3.4 Topographic image (A) and corresponding adhesion map (B) of sphalerite surface, and topographic image (C) and corresponding adhesion map (D) of conditioned sphalerite surface.

Figure 3.5 shows the histograms of measured adhesion F_{adh}/R and the fitted Gaussian distributions (solid curve) of sphalerite before/after conditioning treatment. The adhesion distribution of sphalerite surface in Figure 3.5A falls in a very narrow range between 0 and 30 mN/m with the fitted peak centered at 16.4 mN/m. After conditioning treatment, the range of adhesion distribution is extended to 0-120 mN/m with two fitted peaks respectively centered at 15.5 mN/m and 58.1 mN/m in Figure 3.5B. It is evident that the hydrophobicity of mineral surface changes from homogeneous state to heterogeneous distribution after conditioning treatment due to non-uniform adsorption of xanthate. The small peak centered at 15.5 mN/m of conditioned sphalerite exhibits a narrow range from 0 to 30 nN (Figure 3.5B), which is comparable to the case of sphalerite in Figure 3.5A, indicating the hydrophilic domain. In contrast, the large peak centered at 58.1 mN/m exhibits a wide range from 30 to 120 nN, suggesting the hydrophobic domain. Therefore, conditioning treatment could change the chemical characteristics of mineral surface by keeping some domains unchanged while turning other domains to different degrees of hydrophobicity.

According to the fitted Gaussian distributions, surface area of hydrophobic domain, also referring to surface coverage of xanthate, accounts for around 88.9%. As compared to the coverage (84.1% xanthate coverage) based on contact angle measurements, the results from the two types of measurements are very close, while the adhesion force mapping provides more precise information on the local characteristics at the nanoscale rather than a statistical average of a relatively large surface area.

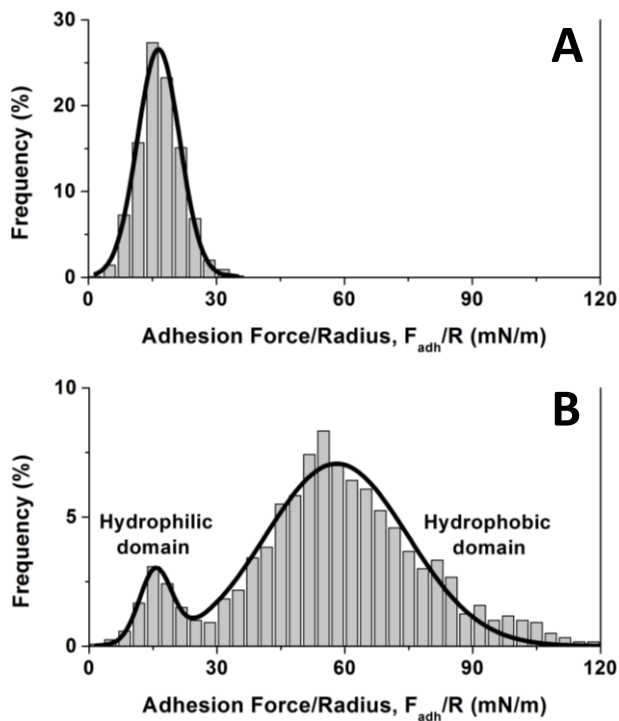


Figure 3.5 The histograms of measured adhesion F_{adh}/R and the fitted Gaussian distributions (solid curve) of (A) sphalerite and (B) conditioned sphalerite.

Figure 3.6 shows the measured forces (open symbols) and theoretical calculations (red curve) between the thiol-functionalized gold (thiol/Au) tip and sphalerite surface in 0.5 M NaCl. The measured forces show an attraction at a separation distance of ~ 6 nm during approach. As mentioned above, the EDL interaction is negligible in concentrated salt solution. The monolayer self-assembled on gold tip and xanthate layer adsorbed on sphalerite surface are very thin (1-2 nm), and their effect on the VDW interaction between the gold tip and sphalerite surface could be neglected at separation $D > 3$ nm.^{8, 46,}
⁵⁴ The Hamaker constant for Au-water-ZnS (sphalerite) is calculated to be 8.9×10^{-20} J, based on which the calculations using the classical DLVO theory agree well with the measured forces in Figure 3.6.^{46, 55} The discrepancy at separation distance below 2 nm is

mainly arising from the effects of surface roughness and hydration of the untreated sphalerite surface.^{29, 46}

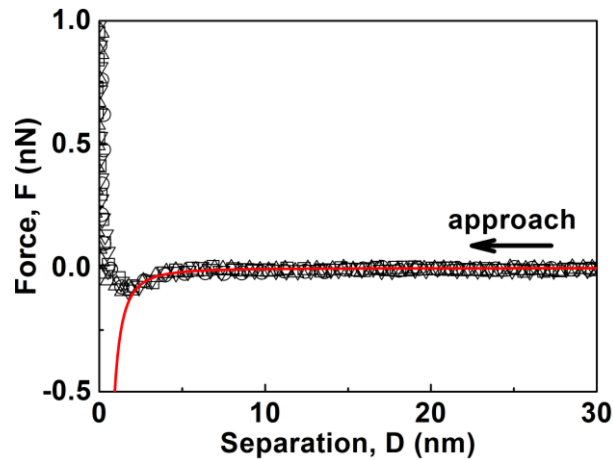


Figure 3.6 Interaction force between the hydrophobic AFM tip and sphalerite surface in 0.5 M NaCl. Experiment results are shown in open symbols, and theoretical calculations based on the classical DLVO model are shown in red curve.

Figure 3.7 shows the interaction between the thiol/Au tip and different domains (I, II, III, and IV) on conditioned sphalerite in 0.5 M NaCl. The domain I, II, III, and IV are denoted for the adhesion regions of $F_{ad}/R \sim 10\text{-}20$ mN/m, 40-50 mN/m, 70-80 mN/m and 100-110 mN/m, respectively. As illustrated in Figure 3.7A, the measured forces on domain I show the same attraction behavior as the sphalerite case (Figure 3.6), which are consistent with the calculations based on the classical DLVO theory (red curve). It is evident from Figures 3.7B, 3.7C and 3.7D that the measured attraction (open symbols) is much stronger than that contributed by the VDW interaction (red curve) for domains II, III, and IV. Thus, the additional attraction should arise from the hydrophobic interaction, which is incorporated into the extended DLVO model (green curve) to fit the measured forces. The theoretically fitted results show that the decay length D_0 of

hydrophobic interaction increases from 0.7 nm for domain II to 1.0 nm for domain III and 1.2 nm for domain IV, which coincides with the enhanced adhesion.

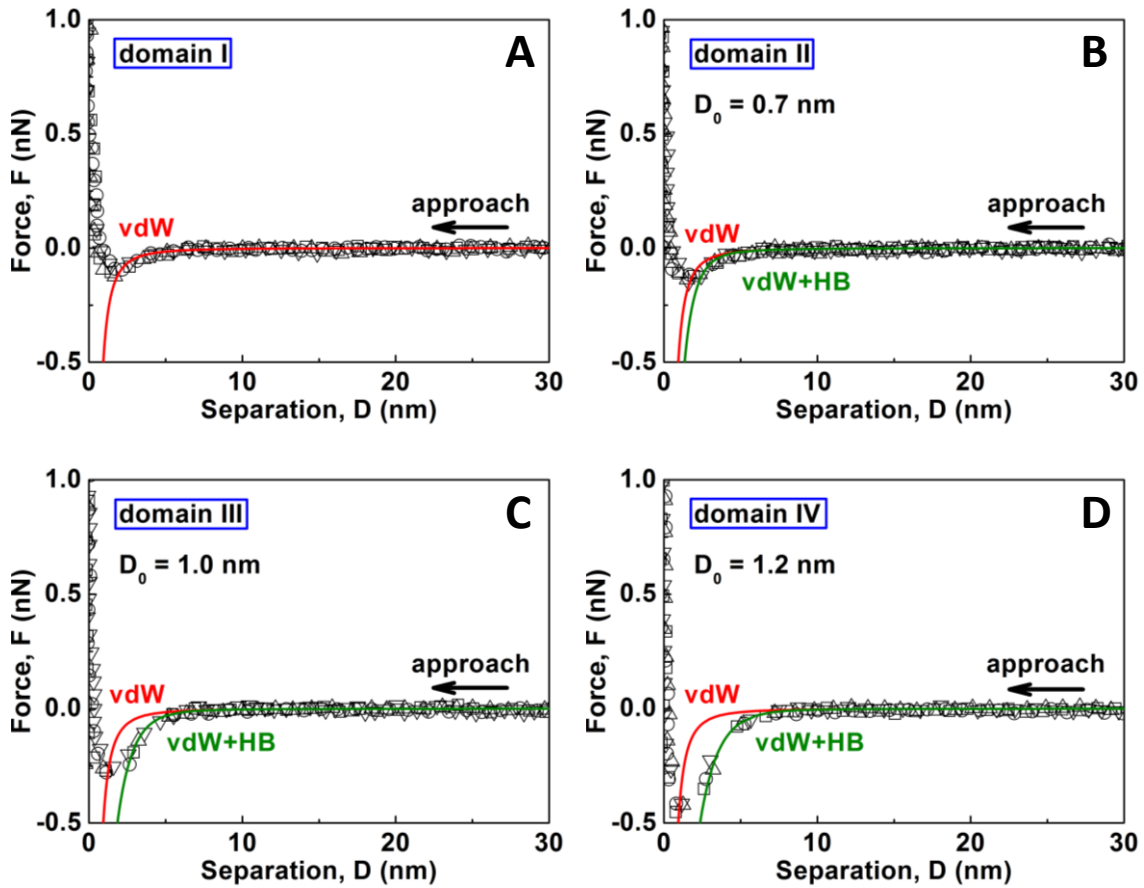


Figure 3.7 Interaction forces between the hydrophobic AFM tip and different domains (i.e. domain I, II, III, and IV) of conditioned sphalerite in 0.5 M NaCl. Experiment results are shown in open symbols, and theoretical calculations based on the classical DLVO model and extended DLVO model including the hydrophobic effect are shown in red curve and green curve, respectively.

Therefore, it is clear from the above results that hydrophobic interaction could not be detected between the hydrophobic tip and hydrophilic sphalerite. The non-uniform adsorption of xanthate during conditioning treatment of sphalerite results in the

heterogeneous force characteristics by keeping some surface domains (e.g. domain I) unchanged while endowing other domains (e.g. domains II, III, IV) different degrees of hydrophobicity.

3.3.4 Adhesion energy

The surface energies of thiol/Au, sphalerite and conditioned sphalerite were determined by measuring the static contact angles of diiodomethane, glycerol and ethylene glycol on these solid surfaces. As shown in Table 3.2, the surface energies of thiol/Au, sphalerite and conditioned sphalerite were determined to be 16.7, 49.7 and 48.4 mJ/m², respectively. The adhesion energy, or work of adhesion per unit area W_{adh} for thiol/Au-water-mineral was calculated to be 3.5 mJ/m² for sphalerite and 11.6 mJ/m² for conditioned sphalerite based on Equation 3.6.⁴⁸

$$\begin{aligned}
 W_{adh} = & 2(\sqrt{\gamma_{water}^{LW}} - \sqrt{\gamma_{thiol/Au}^{LW}})(\sqrt{\gamma_{mineral}^{LW}} - \sqrt{\gamma_{water}^{LW}}) \\
 & + 2[\sqrt{\gamma_{water}^+}(\sqrt{\gamma_{thiol/Au}^-} + \sqrt{\gamma_{mineral}^-} - \sqrt{\gamma_{water}^-}) \\
 & + \sqrt{\gamma_{water}^-}(\sqrt{\gamma_{thiol/Au}^+} + \sqrt{\gamma_{mineral}^+} - \sqrt{\gamma_{water}^+}) \\
 & - \sqrt{\gamma_{thiol/Au}^+ \gamma_{mineral}^-} - \sqrt{\gamma_{thiol/Au}^- \gamma_{mineral}^+}] \quad (3.6)
 \end{aligned}$$

The adhesion F_{adh}/R for two flat surfaces is correlated to the work of adhesion W_{adh} by the DMT model given by Equation 3.7.⁴⁶ Based on the W_{adh} values obtained from three probe liquid method, the adhesion F_{adh}/R is predicted to be 22.1 mN/m for sphalerite and 72.6 mN/m for conditioned sphalerite, both of which fall into the range of measured adhesion of sphalerite and conditioned sphalerite in Figure 3.5.

$$W_{adh} = -\frac{1}{2\pi} F_{adh} / R \quad (3.7)$$

Table 3.2 Surface energy γ with Lifshitz-van der Waals γ^{LW} and Lewis acid-base γ^{AB} (electron acceptor γ^+ and electron donor γ^-) components for different substrates, mJ/m²

Substrate	γ^{LW}	γ^+	γ^-	γ^{AB}	γ
thiol/Au	16.54	0.01	0.73	0.16	16.7
sphalerite	45.46	0.06	72.41	4.23	49.7
conditioned sphalerite	39.15	0.39	54.70	9.23	48.4

3.4 Conclusions

Surface heterogeneity has an important influence on a wide range of engineering applications, such as mineral froth flotation. In this work, using sphalerite as a model mineral, the nanoscale heterogeneity of surface hydrophobicity and surface interactions on mineral surface before/after conditioning treatment were probed using AFM force mapping, which reveals that the adhesion on sphalerite falls in a narrow range with a peak centered at 16.4 mN/m, and the adhesion on conditioned sphalerite (activated by copper sulfate and then treated by ethyl xanthate) falls in a wide range with a small peak centered at 15.5 mN/m and a large peak centered at 58.1 mN/m. It is clear that the conditioning treatment changed the chemical characteristics of mineral surface by keeping some domains unchanged while endowing other domains different degrees of hydrophobicity due to non-uniform adsorption of xanthate. The interaction forces between a hydrophobic thiol-functionalized AFM tip and the hydrophobic domains on

conditioned sphalerite showed “jump-in” behavior during approach which could not be well described by the classical DLVO model but could be well fitted by the extended DLVO theory by including the hydrophobic effect. The decay length of hydrophobic interaction was found to vary from 0.7 to 1.2 nm on the different hydrophobic domains, indicating enhanced hydrophobic attraction. This work provides a useful methodology to investigate the nanoscale heterogeneity of surface hydrophobicity and surface interaction mechanisms on different domains of solid mineral surface, which can be extended to many other inherently heterogeneous surfaces and processes such as protein folding and self-assembly of block copolymers.

3.5 Acknowledgement

We gratefully acknowledge the financial support from the Natural Sciences and Engineering Research Council of Canada (NSERC), Canadian Centre for Clean Coal/Carbon and Mineral Processing Technologies (C5MPT), the Canada Foundation for Innovation (CFI) and the Alberta Advanced Education & Technology Small Equipment Grants Program (AET/SEGP).

3.6 References

1. Zhou, R.; Huang, X.; Margulis, C. J.; Berne, B. J., Hydrophobic Collapse in Multidomain Protein Folding. *Science* **2004**, *305*, 1605-1609.
2. Dyson, H. J.; Wright, P. E.; Scheraga, H. A., The Role of Hydrophobic Interactions in Initiation and Propagation of Protein Folding. *Proc. Natl. Acad. Sci. U. S. A.* **2006**, *103*, 13057-13061.

3. Chandler, D., Interfaces and the Driving Force of Hydrophobic Assembly. *Nature* **2005**, *437*, 640-647.
4. Wang, C.-W.; Sinton, D.; Moffitt, M. G., Flow-Directed Block Copolymer Micelle Morphologies Via Microfluidic Self-Assembly. *J. Am. Chem. Soc.* **2011**, *133*, 18853-18864.
5. Mao, Z.; Xu, H.; Wang, D., Molecular Mimetic Self-Assembly of Colloidal Particles. *Adv. Funct. Mater.* **2010**, *20*, 1053-1074.
6. Ma, F.; Wang, S.; Zhao, H.; Wu, D. T.; Wu, N., Colloidal Structures of Asymmetric Dimers Via Orientation-Dependent Interactions. *Soft matter* **2014**, *10*, 8349-8357.
7. Xie, L.; Shi, C.; Wang, J.; Huang, J.; Lu, Q.; Liu, Q.; Zeng, H., Probing the Interaction between Air Bubble and Sphalerite Mineral Surface Using Atomic Force Microscope. *Langmuir* **2015**, *31*, 2438-2446.
8. Xie, L.; Wang, J.; Shi, C.; Huang, J.; Zhang, H.; Liu, Q.; Liu, Q.; Zeng, H., Probing Surface Interactions of Electrochemically Active Galena Mineral Surface Using Atomic Force Microscope. *J. Phys. Chem. C* **2016**, *120*, 22433–22442.
9. Schuler, B.; Lipman, E. A.; Eaton, W. A., Probing the Free-Energy Surface for Protein Folding with Single-Molecule Fluorescence Spectroscopy. *Nature* **2002**, *419*, 743-747.
10. Chau, T.; Bruckard, W.; Koh, P.; Nguyen, A., A Review of Factors That Affect Contact Angle and Implications for Flotation Practice. *Adv. Colloid Interface Sci.* **2009**, *150*, 106-115.
11. Chau, T., A Review of Techniques for Measurement of Contact Angles and Their Applicability on Mineral Surfaces. *Miner. Eng.* **2009**, *22*, 213-219.
12. Rao, S. R., *Surface Chemistry of Froth Flotation: Volume 1: Fundamentals*; Springer

Science & Business Media, **2013**.

13. Fuerstenau, M. C.; Jameson, G. J.; Yoon, R.-H., *Froth Flotation: A Century of Innovation*; SME, **2007**.

14. Kelly, E. G.; Spottiswood, D. J., *Introduction to Mineral Processing*; Wiley New York, **1982**.

15. Leppinen, J.; Basilio, C.; Yoon, R., In-Situ FTIR Study of Ethyl Xanthate Adsorption on Sulfide Minerals under Conditions of Controlled Potential. *Int. J. Miner. Process.* **1989**, *26*, 259-274.

16. Larsson, M.; Holmgren, A.; Forsling, W., Xanthate Adsorbed on ZnS Studied by Polarized FTIR-ATR Spectroscopy. *Langmuir* **2000**, *16*, 8129-8133.

17. Mielczarski, J., XPS Study of Ethyl Xanthate Adsorption on Oxidized Surface of Cuprous Sulfide. *J. Colloid Interface Sci.* **1987**, *120*, 201-209.

18. Page, P.; Hazell, L., X-Ray Photoelectron Spectroscopy (XPS) Studies of Potassium Amyl Xanthate (Kax) Adsorption on Precipitated PbS Related to Galena Flotation. *Int. J. Miner. Process.* **1989**, *25*, 87-100.

19. Woods, R.; Hope, G. A.; Watling, K., Surface Enhanced Raman Scattering Spectroscopic Studies of the Adsorption of Flotation Collectors. *Miner. Eng.* **2000**, *13*, 345-356.

20. Buckley, A.; Parks, T.; Vassallo, A.; Woods, R., Verification by Surface-Enhanced Raman Spectroscopy of the Integrity of Xanthate Chemisorbed on Silver. *Int. J. Miner. Process.* **1997**, *51*, 303-313.

21. Brinen, J.; Reich, F., Static Sims Imaging of the Adsorption of Diisobutyl Dithiophosphate on Galena Surfaces. *Surf. Interface Anal.* **1992**, *18*, 448-452.

22. Brinen, J.; Greenhouse, S.; Nagaraj, D.; Lee, J., Sims and Sims Imaging Studies of Adsorbed Dialkyl Dithiophosphinates on PbS Crystal Surfaces. *Int. J. Miner. Process.* **1993**, *38*, 93-109.
23. Stowe, K.; Chryssoulis, S.; Kim, J., Mapping of Composition of Mineral Surfaces by Tof-Sims. *Miner. Eng.* **1995**, *8*, 421-430.
24. Piantadosi, C.; Jasieniak, M.; Skinner, W.; Smart, R. S. C., Statistical Comparison of Surface Species in Flotation Concentrates and Tails from Tof-Sims Evidence. *Miner. Eng.* **2000**, *13*, 1377-1394..
25. Brito e Abreu, S.; Brien, C.; Skinner, W., Tof-Sims as a New Method to Determine the Contact Angle of Mineral Surfaces. *Langmuir* **2010**, *26*, 8122-8130.
26. BARD, A.; FAN, F.; Pierce, D. T.; Unwin, P. R.; Wipf, D. O.; Zhou, F., Chemical Imaging of Surfaces with the Scanning Electrochemical Microscope. *Science* **1991**, *254*, 68-74.
27. Wang, J.; Liu, Q.; Zeng, H., Understanding Copper Activation and Xanthate Adsorption on Sphalerite by Time-of-Flight Secondary Ion Mass Spectrometry, X-Ray Photoelectron Spectroscopy, and in Situ Scanning Electrochemical Microscopy. *J. Phys. Chem. C* **2013**, *117*, 20089-20097.
28. Ducker, W. A.; Senden, T. J.; Pashley, R. M., Direct Measurement of Colloidal Forces Using an Atomic Force Microscope. *Nature* **1991**, *353*, 239-241.
29. Butt, H.-J.; Cappella, B.; Kappl, M., Force Measurements with the Atomic Force Microscope: Technique, Interpretation and Applications. *Surf. Sci. Rep.* **2005**, *59*, 1-152.
30. Yang, D.; Xie, L.; Bobicki, E.; Xu, Z.; Liu, Q.; Zeng, H., Probing Anisotropic Surface Properties and Interaction Forces of Chrysotile Rods by Atomic Force Microscopy and

Rheology. *Langmuir* **2014**, *30*, 10809-10817.

31. Wang, J.; Li, J.; Xie, L.; Shi, C.; Liu, Q.; Zeng, H., Interactions between Elemental Selenium and Hydrophilic/Hydrophobic Surfaces: Direct Force Measurements Using AFM. *Chem. Eng. J.* **2016**, *303*, 646-654.

32. Shi, C.; Cui, X.; Xie, L.; Liu, Q.; Chan, D. Y.; Israelachvili, J. N.; Zeng, H., Measuring Forces and Spatiotemporal Evolution of Thin Water Films between an Air Bubble and Solid Surfaces of Different Hydrophobicity. *ACS nano* **2015**, *9*, 95-104.

33. Shi, C.; Zhang, L.; Xie, L.; Lu, X.; Liu, Q.; Mantilla, C. A.; van den Berg, F. G.; Zeng, H., Interaction Mechanism of Oil-in-Water Emulsions with Asphaltenes Determined Using Droplet Probe AFM. *Langmuir* **2016**, *32*, 2302-2310.

34. Cui, X.; Shi, C.; Xie, L.; Liu, J.; Zeng, H., Probing Interactions between Air Bubble and Hydrophobic Polymer Surface: Impact of Solution Salinity and Interfacial Nanobubbles. *Langmuir* **2016**, *32*, 11236-11244.

35. Gao, Z.; Hu, Y.; Sun, W.; Drelich, J. W., Surface Charge Anisotropy of Scheelite Crystals. *Langmuir* **2016**, *32*, 6282-6288.

36. He, Y.; Tian, Y.; Ribbe, A. E.; Mao, C., Highly Connected Two-Dimensional Crystals of DNA Six-Point-Stars. *J. Am. Chem. Soc.* **2006**, *128*, 15978-15979.

37. Frisbie, C. D.; Rozsnyai, L. F.; Noy, A.; Wrighton, M. S.; Lieber, C. M., Functional Group Imaging by Chemical Force Microscopy. *Science* **1994**, *265*, 2071-2074.

38. Noy, A.; Vezenov, D. V.; Lieber, C. M., Chemical Force Microscopy. *Annu. Rev. Mater. Sci.* **1997**, *27*, 381-421.

39. Noy, A.; Frisbie, C. D.; Rozsnyai, L. F.; Wrighton, M. S.; Lieber, C. M., Chemical Force Microscopy: Exploiting Chemically-Modified Tips to Quantify Adhesion, Friction,

and Functional Group Distributions in Molecular Assemblies. *J. Am. Chem. Soc.* **1995**, *117*, 7943-7951.

40. Vezenov, D. V.; Noy, A.; Rozsnyai, L. F.; Lieber, C. M., Force Titrations and Ionization State Sensitive Imaging of Functional Groups in Aqueous Solutions by Chemical Force Microscopy. *J. Am. Chem. Soc.* **1997**, *119*, 2006-2015.

41. Dague, E.; Alsteens, D.; Latgé, J.-P.; Verbelen, C.; Raze, D.; Baulard, A. R.; Dufrêne, Y. F., Chemical Force Microscopy of Single Live Cells. *Nano letters* **2007**, *7*, 3026-3030.

42. Alsteens, D.; Dague, E.; Rouxhet, P. G.; Baulard, A. R.; Dufrêne, Y. F., Direct Measurement of Hydrophobic Forces on Cell Surfaces Using AFM. *Langmuir* **2007**, *23*, 11977-11979.

43. Chandra, A.; Gerson, A., A Review of the Fundamental Studies of the Copper Activation Mechanisms for Selective Flotation of the Sulfide Minerals, Sphalerite and Pyrite. *Adv. Colloid Interface Sci.* **2009**, *145*, 97-110.

44. Hutter, J. L.; Bechhoefer, J., Calibration of Atomic-Force Microscope Tips. *Rev. Sci. Instrum.* **1993**, *64*, 1868-1873.

45. Drelich, J.; Long, J.; Yeung, A., Determining Surface Potential of the Bitume-Water Interface at Nanoscale Resolution Using Atomic Force Microscopy. *Can. J. Chem. Eng.* **2007**, *85*, 625-634.

46. Israelachvili, J. N., *Intermolecular and Surface Forces: Revised Third Edition*; Academic press, **2011**.

47. Shi, C.; Chan, D. Y.; Liu, Q.; Zeng, H., Probing the Hydrophobic Interaction between Air Bubbles and Partially Hydrophobic Surfaces Using Atomic Force Microscopy. *J. Phys. Chem. C* **2014**, *118*, 25000-25008.

48. Van Oss, C. J., *Interfacial Forces in Aqueous Media*; CRC press, **2006**.
49. Wang, J.; Xie, L.; Liu, Q.; Zeng, H., Effects of Salinity on Xanthate Adsorption on Sphalerite and Bubble-Sphalerite Interactions. *Miner. Eng.* **2015**, *77*, 34-41.
50. Szargan, R.; Karthe, S.; Suoninen, E., XPS Studies of Xanthate Adsorption on Pyrite. *Appl. Surf. Sci.* **1992**, *55*, 227-232.
51. Ranta, L.; Minni, E.; Suoninen, E.; Heimala, S.; Hintikka, V.; Saari, M.; Rastas, J., XPS Studies of Adsorption of Xanthate on Sulfide Surfaces. *Appl. Surf. Sci.* **1992**, *55*, 227-232
52. Somasundaran, P., *Encyclopedia of Surface and Colloid Science*; CRC press, **2006**; Vol. 2.
53. Teng, F.; Liu, Q.; Zeng, H., In Situ Kinetic Study of Zinc Sulfide Activation Using a Quartz Crystal Microbalance with Dissipation (QCMD). *J. Colloid Interface Sci.* **2012**, *368*, 512-520.
54. Love, J. C.; Estroff, L. A.; Kriebel, J. K.; Nuzzo, R. G.; Whitesides, G. M., Self-Assembled Monolayers of Thiolates on Metals as a Form of Nanotechnology. *Chem. Rev.* **2005**, *105*, 1103-1170.
55. Toikka, G.; Hayes, R. A.; Ralston, J., Surface Forces between Spherical ZnS Particles in Aqueous Electrolyte. *Langmuir* **1996**, *12*, 3783-3788.

Chapter 4 Probing Surface Interactions of Electrochemically Active Galena Mineral Surface using Atomic Force Microscopy

4.1 Introduction

The colloidal stability governed by various surface interactions including van der Waals (VDW) interaction, electrical double layer (EDL) interaction, hydrophobic interaction, and some other interactions, plays an important role in a wide range of interfacial processes such as catalysis,¹⁻² energy storage,³⁻⁴ and froth flotation.⁵⁻⁶ Interfacial electrochemical processes can change the physical and chemical characteristics of the solid/water interface, and in certain cases could pose challenging issues such as nanoparticle aggregation that limits the performance and durability of electrocatalysis and electrochemical energy storage.⁷⁻⁸ The electrochemical oxidation of mineral surface is particularly important in froth flotation, where the formed hydrophobic species during the electrochemical process can effectively enhance the attachment efficiency of mineral particles to air bubbles but adversely cause clay slime coating on mineral surfaces.⁹⁻¹⁰ Consequently, a fundamental understanding of the interfacial properties and surface interaction mechanisms of mineral surfaces during the associated electrochemical process in froth flotation is critical to modulate the interactions and optimize the processing conditions towards the development of more cost-effective and environment-friendly flotation technology.

Over the last few decades, much effort and significant progress have been made on the reaction mechanisms and characterizations of products associated with the interfacial electrochemical processes of sulfide minerals in mineral processing. Different surface analytical tools such as X-ray photoelectron spectroscopy (XPS),¹¹⁻¹² Raman spectroscopy,¹³⁻¹⁴ Fourier transform infrared spectroscopy (FTIR),¹⁵⁻¹⁶ and Time-of-flight secondary ion mass spectrometry (ToF-SIMS)¹⁷⁻¹⁸ have been used to characterize the surface chemical compositions of electrochemically oxidized sulfide minerals. It is widely accepted that hydrophobic sulfur-rich species are generally formed after mild electrochemical oxidation of sulfide minerals, which may consist of elemental sulfur (S^0), metal-deficient sulfides ($M_{1-x}S$), and polysulfides (S_n^{2-}) based on solution conditions (e.g. solution pH and electrochemical potential).¹¹⁻²⁰ Nevertheless, many of these conventional techniques are not able to characterize the mineral surfaces *in situ* during the electrochemical processes, which may result in change of surface properties after long-term exposure to air or aqueous solution. Moreover, the relatively low spatial resolution limits the characterization of electrochemically active mineral surfaces at the atomic level and nanoscale.

Surface forces apparatus (SFA) and atomic force microscopy (AFM) have been extensively employed to characterize the surface properties and directly measure different intermolecular and surface forces at the nanoscale.²¹⁻³⁴ Combined with the electrochemical setup, SFA and AFM have realized the simultaneous measurements of surface properties and forces during electrochemical processes.³⁵⁻³⁷ Valtiner et al.³⁵ applied an electrochemical surface forces apparatus (EC-SFA) to measure the thickness of anodic oxide layer on gold surfaces and the forces between the oxide layer and APTES

coated mica surface at high electrochemical potentials. In the studies by Wittstock et al.³⁶ and Hampton et al.,³⁷ the morphological changes of potentiostatically oxidized galena surface were monitored in acetate buffer at pH 4-5 using the electrochemical atomic force microscopy (EC-AFM), which showed that surface oxidation was observed at a lower electrochemical potential and the surface became considerably rougher with the increase of the applied potential. Preferential deposition of oxidation products at impurities and crystal defects was found by Hampton et al.,³⁷ while such preferential formation was not observed in the work by Wittstock et al.,³⁶ which makes it difficult to draw a general conclusion about the surface oxidation mechanisms of sulfide minerals. Herein, the combined capabilities of EC-AFM to control the interfacial chemical reaction and simultaneously probe the evolution of morphological changes and surface forces facilitate direct characterization of the surface properties of electrochemically active mineral surface at the nanoscale, which, to our knowledge, has not been reported.

The conductive AFM as a current-sensing technique has been widely applied in the characterization of conductive polymers and nanomaterials,³⁸⁻³⁹ dielectric and ferroelectric films,⁴⁰⁻⁴¹ and biomaterials⁴² to map the electrical conductivity. The current distribution on electrochemically active mineral surface and the current variation with changing the electrochemical potential respectively indicate if the electrochemical redox reactions are homogeneous over the surface and if the oxidation products are formed on the surface. Thus, conductive AFM coupled with the measurements such as water contact angle and surface chemistry analysis using cryo-XPS can provide useful and complementary information on the physical and chemical characteristics of electrochemically active mineral surfaces.

In this work, galena (natural mineral form of lead sulfide) was chosen as a model sulfide mineral which has semi-metallic conductivity and perfect cubic cleavage. Galena is a semiconductor material with a small band gap of about 0.4 eV, and galena crystal with a face-centered cubic structure can be easily cleaved along the (100) crystal plane, which allows the preparation of conductive mineral surface with molecular-scale roughness.³⁶ The EC-AFM was employed, for the first time, to probe the morphological changes and surface forces on galena mineral surface potentiostatically treated at various electrochemical potentials in aqueous solution. The extended Derjaguin–Landau–Verwey–Overbeek (DLVO) theory by including the effect of hydrophobic interaction was applied to interpret the measured forces between hydrophilic/hydrophobic AFM tip and galena surface under varying potential. Water contact angle measurements, cryo-XPS analysis, and conductive AFM characterizations were also conducted to provide complementary information for a better understanding of the physical and chemical characteristics of galena surface. This work provides useful information on the electrochemical reaction mechanisms and related products of electrochemically polarized mineral surface, and new insights into the surface interaction mechanisms between hydrophilic/hydrophobic surfaces (e.g. gangue particles of different hydrophobicity) and mineral surfaces with different degrees of electrochemical oxidation.

4.2 Materials and methods

4.2.1 Materials

Sodium chloride (NaCl, ACS reagent grade, Fisher Scientific), sulfuric acid (H₂SO₄, 95-98%, ACS reagent grade, Fisher Scientific), hydrogen peroxide (H₂O₂, 30%

w/w in water, ACS reagent grade, Fisher Scientific), octadecyltrichlorosilane (OTS, $C_{18}H_{37}Cl_3Si$, 95%, ACROS organics), hexane (C_6H_{14} , ACS reagent grade, Fisher Scientific), and chloroform ($CHCl_3$, ACS reagent grade, Fisher Scientific) were used as received without further purification. The electrolyte solution (i.e. 0.5 M NaCl) was prepared using Milli-Q water (Millipore deionized, 18.2 $M\Omega\cdot cm$ resistivity) and the solution pH was measured to be 5.6. In this work, the NaCl concentration was fixed at 0.5 M, under which the EDL could be significantly compressed, to investigate the effects of other factors (e.g. electrochemical treatment). Meanwhile, water of high salinity has attracted tremendous interest in mineral industry due to the shortage of fresh water sources available.

Galena (Ward's Science, NY, USA) was fractured to obtain the natural cleavage surface that was then cleaned using high purity nitrogen to remove loosely attached galena fragments. The cleaved galena surface was glued onto a conductive metal disk by silver conductive epoxy to ensure good electrical contact, and the insulating epoxy was then applied to cover the conductive metal disk with only the galena surface exposed for electrochemical experiments. The prepared galena working electrode was immediately transferred into the electrochemical cell for electrochemical experiments.

4.2.2 Electrochemical experiments

Electrochemical experiments were performed on the prepared galena working electrode in 0.5 M NaCl using the electrochemical cell of MFP-3D AFM (Asylum Research, Santa Barbara, CA, USA) coupled with a CHI 920c Scanning Electrochemical Microscope (CH Instruments, Inc., TX, USA). The three electrode cell was constructed

by using a carbon electrode as the counter electrode and an Ag/AgCl/3.4 M KCl microelectrode as the reference electrode (0.206 V vs standard hydrogen electrode (SHE)). All potentials quoted in this work were referred to the Ag/AgCl/3.4 M KCl reference electrode unless otherwise specified.

Cyclic Voltammetry (CV) was initiated at the open circuit potential (OCP) of 0.02 V at a potential sweep rate of 0.02 V/s in the negative direction with the cathodic limit of -0.7 V and the anodic limit of 0.45 V. To potentiostatically control the interfacial chemical reaction, a series of successive potentials (i.e. -0.7, -0.3, 0, 0.1, 0.2, 0.3 and 0.45 V) were respectively held for 20 s on galena surface, which was then subjected to various surface characterizations.

4.2.3 Electrochemical atomic force microscopy (EC-AFM)

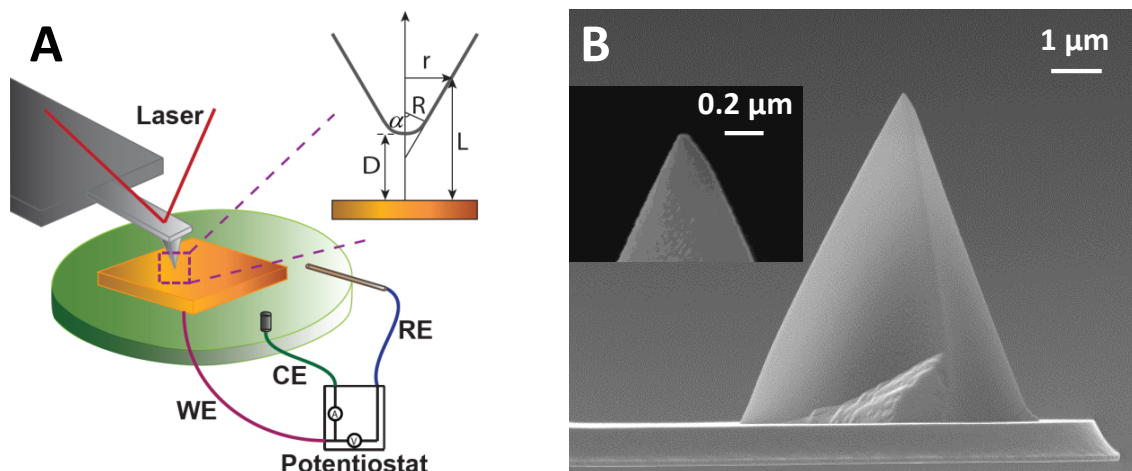


Figure 4.1 (A) The schematic of EC-AFM for the topographic imaging and force measurements on galena mineral surface during a typical electrochemical AFM experiment. Inset figure shows the geometry of conical AFM tip with a spherical cap at the apex, where α is the geometry angle for spherical cap, R is the radius of spherical cap, r is the radius of the circle of the tip at a given vertical position, D is the distance

between the tip end and galena surface, and L is the distance between a differential surface section of the tip and galena surface. (B) Typical FE-SEM images for analysis of the geometry of AFM tips.

The schematic of EC-AFM for controlling the interfacial chemical reaction and simultaneously probing the evolution of surface characteristics such as morphological changes and surface forces is shown in Figure 4.1A. After each electrochemical potential was applied on galena surface for 20 s, the AFM probe was immediately used to image the surface topography and measure the forces.

The in situ evolution of morphology and roughness of galena surface at different electrochemical potentials in 0.5 M NaCl was characterized with a silicon nitride AFM tip in contact mode. The force measurements were performed on at least ten different positions of the sample surface and at least two samples surfaces under the same experimental condition with hydrophilic silicon nitride AFM tip or hydrophobic OTS functionalized AFM tip at different electrochemical potentials in 0.5 M NaCl. The OTS hydrophobized AFM tips were prepared by immersing silicon nitride AFM tips in a freshly prepared piranha solution for 30 min and then in 2 mM OTS in a mixture of hexane/chloroform (4:1 vol/vol) overnight following an established method.⁴³ The prepared OTS hydrophobized AFM tips were rinsed by chloroform and dried using high purity nitrogen prior to the force measurements. The surface hydrophobicity of AFM tips was evaluated by measuring the average water contact angle on AFM cantilever, which showed the wetting behavior of silicon nitride cantilevers and the average water contact angle of $\sim 95^\circ$ on OTS hydrophobized cantilevers. During the force measurements, the tip

was driven to approach and then retract from the surface with constant velocity and loading force. The deflection of the cantilever was detected through a laser beam that was reflected from the cantilever to a split photodiode detector, which was further converted to force using the spring constant and Hooke's law. The spring constants of the cantilevers were determined to be 0.1-0.2 N/m using the Hutter and Bechhoefer method.⁴⁴

4.2.4 Surface characterization

Galena surface was first potentiostatically treated by the electrochemical setup in Figure 4.1A and then used to characterize surface wettability through water contact angle measurements, elemental composition by cryo-XPS analysis and current distribution using conductive AFM.

A contact angle goniometer (ramé-hart instrument Co., NJ, USA) was used to measure the static water contact angle on potentiostatically treated galena surface using a sessile drop method. For each type of surface, at least three different positions on the same surface and two sample surfaces were tested, and the average water contact angle was reported.

The elemental compositions of sample surfaces were characterized by cryo-XPS spectra using an AXIS 165 spectroscopy system (Kratos Analytical Ltd, UK) equipped with a monochromatized Al K α X-ray source ($h\nu = 1486.6$ eV). The samples were precooled to ~ 130 K and then transferred to the analytical chamber when the vacuum in the fast entry lock was better than 2×10^{-6} Torr, and the temperature in the analytical chamber was kept at ~ 130 K. The base pressure in the analytical chamber was lower than 1×10^{-9} Torr during the measurements. The survey scans were collected for binding

energy spanning from 1100 to 0 eV with analyzer pass energy of 160 eV and a step of 0.4 eV. For high resolution spectra, the pass energy was 20 eV with a step of 0.1 eV. Sample charging was compensated by taking the C 1s peak of background hydrocarbon at 284.8 eV as an internal standard.

Conductive AFM was performed on potentiostatically treated galena surface with a conductive probe to obtain the topographic image simultaneously with the local current map in air. The conductive AFM equipped with the extended TUNA module provides extremely sensitive current detection in the pA range.

4.2.5 Force curve analysis

To interpret the measured forces between AFM tip and solid mineral surface, theoretical analysis was conducted based on the extended DLVO model by including the effect of hydrophobic interaction. Herein, as shown in previous study,⁴⁵ the pyramidal geometry of AFM tip was reasonably assumed to be conical with a spherical cap at the apex, and the geometry and parameters used for the theoretical calculations are illustrated in Figure 4.1A. The geometry of AFM tips was determined by JAMP-9500F Field Emission Auger Microprobe (JEOL, MA, USA) equipped with Schottky field emitter. Based on the analysis of FE-SEM images of the tip (illustrated in Figure 4.1B) by ImageJ software following an established method,^{35, 51-52} the radius of spherical cap R and the geometry angle for spherical cap α could be determined. Typical R values ranged from 28 to 35 nm. For a typical case, R was determined to be ~ 30.6 nm, and α was measured as $\sim 60.8^\circ$.

In this work, the force measurements were conducted in concentrated salt solution (i.e. 0.5 M NaCl), of which the contribution of EDL force is significantly suppressed. The VDW force between AFM tip and flat substrate F_{VDW} can be given by Equation 4.1, where A_H is the non-retarded Hamaker constant and $L_1 = D + R(1 - \cos \alpha)$.⁴⁵

$$F_{VDW} = \frac{A_H}{6} \left[\frac{R + D - 2L_1}{L_1^2} - \frac{R - D}{D^2} \right] - \frac{A_H}{3 \tan^2 \alpha} \left(\frac{1}{L_1} + \frac{R \sin \alpha \tan \alpha - D - R(1 - \cos \alpha)}{2L_1^2} \right) \quad (4.1)$$

Hydrophobic force F_{HB} was reported to follow an exponential equation (Equation 4.2),²⁴ where D_0 is the decay length of hydrophobic interaction and C is a constant (N/m).^{30, 46-47}

$$F_{HB} = -CRe^{-D/D_0} \quad (4.2)$$

4.3 Results and discussion

4.3.1 Cyclic voltammetry (CV)

The typical CV curve of the prepared galena working electrode in 0.5 M NaCl is shown in Figure 4.2. The potential swept from the OCP of 0.02 V (0.226 V vs SHE) towards the negative direction with the cathodic limit of -0.7 V and the anodic limit of 0.45 V. The observed redox peaks (marked as peaks 1, 2 and 3) in Figure 4.2 agree well with previous reports.³⁶⁻³⁷

The cathodic reaction at -0.563 V (illustrated as peak 1) is due to the reduction of elemental sulfur to lead sulfide. The anodic reaction at 0.45 V (indicated as peak 3) is the reverse of the cathodic reaction, which arises from the formation of elemental sulfur and the solvation of lead ions (Equation 4.3).



It was reported that the oxidation of galena to metal-deficient lead sulfide can be observed at the potential of ~ 0.2 V vs SHE or at the OCP in aerated solutions, probably due to the slow oxidation rate at the OCP that allows lead ions to migrate from bulk galena to the surface and compensate for the lead vacancies.^{36, 48-49} In Figure 4.2, the anodic reaction shown as peak 2 occurs at the potential of -0.029 V (0.177 V vs SHE), which is close to the potentials to form metal-deficient lead sulfide. Thus, the anodic oxidation at peak 2 is believed to originate from the formation of metal-deficient lead sulfide and the reaction can be given in Equation 4.4.

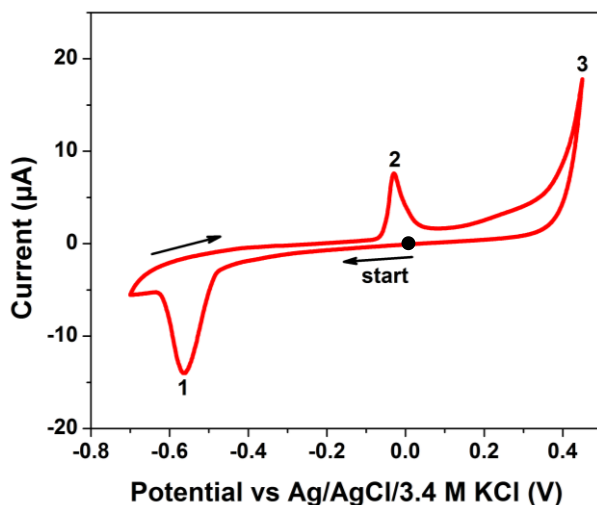
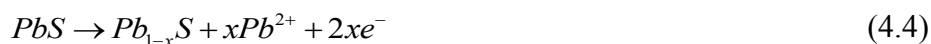


Figure 4.2 CV curve of galena surface in 0.5 M NaCl at a potential sweep rate of 0.02 V/s.

4.3.2 Contact angle measurements

Figure 4.3 shows the static water contact angles on galena surfaces potentiostatically treated at different electrochemical potentials. Galena surface is slightly

hydrophobic with a water contact angle of $\sim 48^\circ$ at -0.7 V, which is consistent with the reported water contact angle of 48° - 52° on galena surface.⁵⁰ As the applied potential increased to -0.3 V, the water contact angle rose to $\sim 54^\circ$, which suggested that galena surface might have been slightly oxidized. With the potential increasing to 0 V, the water contact angle dramatically rose to $\sim 79^\circ$, indicating that galena surface has been moderately oxidized to form a hydrophobic sulfur-rich layer, which agrees well with the anodic oxidation of peak 2 in CV curve (Figure 4.2). The hydrophobic sulfur-rich layer formed at 0 V is believed to be composed of metal-deficient lead sulfide. The continuous rise of potential to 0.3 V and 0.45 V slightly increased the water contact angle to $\sim 82^\circ$ and $\sim 84^\circ$, respectively, revealing that metal-deficient lead sulfide formed at 0 V is a compact layer and elemental sulfur formed within the metal-deficient lead sulfide layer at higher potentials does not significantly change surface hydrophobicity.

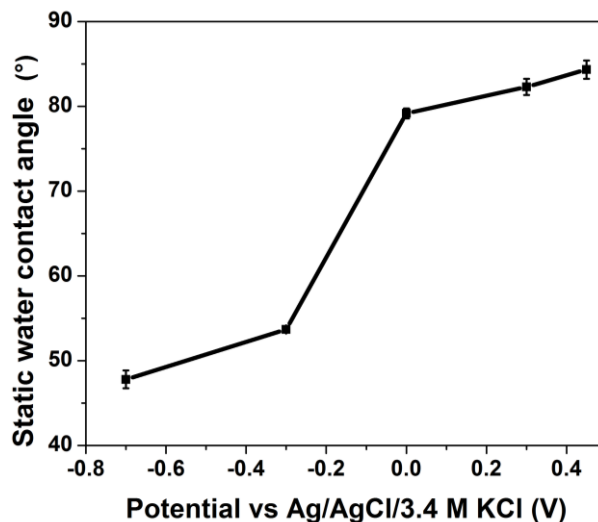


Figure 4.3 Static water contact angle on galena surface as a function of electrochemical potential.

4.3.3 In situ topographic imaging

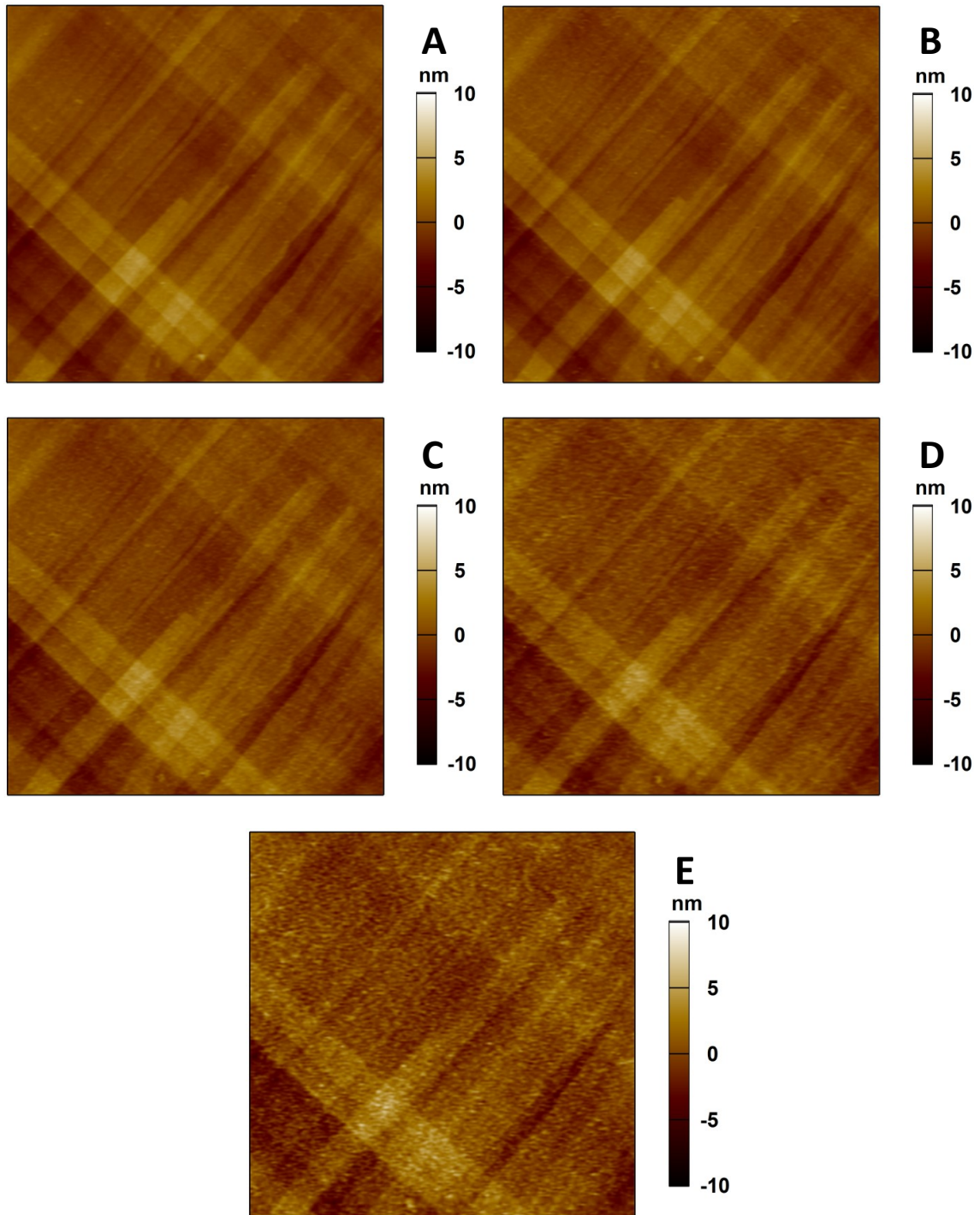


Figure 4.4 AFM topographic images ($5 \times 5 \mu\text{m}^2$) of galena surface at the electrochemical potential of (A) -0.7 V, (B) -0.3 V, (C) 0 V, (D) 0.3 V, and (E) 0.45 V for 20 s in 0.5 M NaCl.

The AFM topographic images of galena surfaces potentiostatically treated at different electrochemical potentials in 0.5 M NaCl are shown in Figure 4.4. All the images have been scanned at the same $5 \times 5 \mu\text{m}^2$ region to better illustrate the morphological variation with the electrochemical potential. Galena can be readily cleaved to generate a molecularly smooth surface with a face-centered cubic structure, and AFM images in Figure 4.4 show that the cleavage steps divide the $5 \times 5 \mu\text{m}^2$ region to a number of small square regions of different sizes.

Figures 4.4A and 4.4B show a freshly cleaved galena surface at -0.7 V and -0.3 V, respectively, with root-mean-square (rms) roughness of 1.18 nm. With increasing the potential from -0.7 V to -0.3 V, the surface morphology had negligible variation. As the applied potential increased to 0 V, the surface morphology changed as shown in Figure 4.4C with rms roughness increased slightly to 1.22 nm, which coincided with the anodic oxidation at peak 2 in CV curve (Figure 4.2). The changes in morphology and chemical compositions contributed to the significantly increased water contact angle at this potential (Figure 4.3). The morphology change and increased surface roughness of galena surface at 0 V (0.206 V vs SHE) here agree with a previous study reported by Hampton et al.³⁷ that the appearance of raised domains and increased surface roughness were observed on galena surface at a potential of 0.258 V (vs SHE).

The continuous increase of potential to 0.3 V and 0.45 V led to significant surface oxidation and thereby more pronounced surface roughening could be observed, as shown in Figures 4.4D and 4.4E, respectively. The rms roughness was determined to be 1.28 nm at 0.3 V and 1.48 nm at 0.45 V. Hampton et al.³⁷ proposed that electrochemical oxidation of galena surface is a two-step process involving releasing sulfur to the solution and

depositing sulfur on favorable sites, based on the observation that the raised domains (< 8 nm in height) were heterogeneously distributed on galena surface. However, in this work, it is evident that the oxidation occurs more homogeneously across the galena surface. It is worthy noticing that the rms roughness of the galena surface cleaved by Hampton et al.³⁷ was ~5 nm, which is dramatically higher than the galena surface with the rms roughness of only ~1 nm in this work. Therefore, it is very likely that the heterogeneous distribution of surface defects and cleavage steps enables the more heterogeneous aggregation of oxidation products in the previous study by Hampton et al.³⁷

It is evident from Figures 4.2 to 4.4 that the CV curve, water contact angle and surface morphology measurements show excellent agreement as electrochemical potential increases from -0.7 V to 0.45 V. Electrochemical treatment under potential of 0 V, that is close to the anodic oxidation of peak 2 in CV curve (Figure 4.2), resulted in significant rise of water contact angle and slight surface roughening due to the formation of a uniform layer of hydrophobic metal-deficient lead sulfide. Electrochemical treatment under potential of 0.45 V, corresponding to the anodic oxidation of peak 3 in CV curve (Figure 4.2), led to slight rise of water contact angle but more pronounced surface roughening which could be likely due to the continuous generation of elemental sulfur in the metal-deficient lead sulfide layer.

4.3.4 Cryo-XPS and conductive AFM

Cryo-XPS and conductive AFM were employed to investigate the elemental composition and current distribution of potentiostatically treated galena surfaces at

typical potential of -0.7 V, 0 V and 0.45 V to further understand the electrochemical reaction mechanisms and related products on galena surfaces.

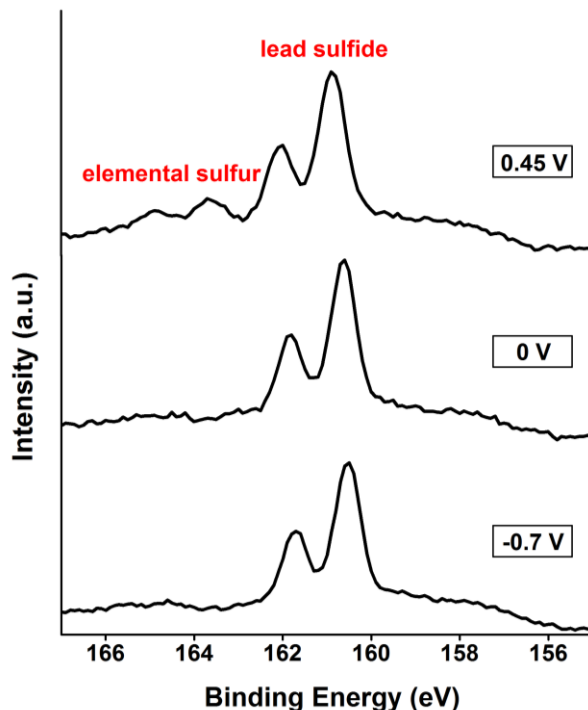


Figure 4.5 XPS spectra of S 2p for potentiostatically treated galena surfaces at electrochemical potential of -0.7 V, 0 V and 0.45 V.

The low temperature ~ 130 K of cryo-XPS enables the detection of volatile species such as elemental sulfur. The S 2p spectra of potentiostatically treated galena surface at -0.7 V, 0 V and 0.3 V are compared in Figure 4.5. Galena surface at -0.7 V had only one doublet with S 2p at 160.5 eV that is attributed to the sulfur in lead sulfide. As the applied potential increased to 0 V, a similar doublet at 160.6 eV was found while the metal-deficient lead sulfide was not observed most likely because the formation of thin layer of metal-deficient lead sulfide (much less than 1 nm based on the morphological variation) was not significant under such electrochemical treatment, which was not easily detected

by XPS. At 0.45 V, another doublet with S 2p at 163.7 eV corresponding to the elemental sulfur was detected, in addition to the doublet of lead sulfide, which agrees very well with previous reports.³⁶⁻³⁷ It is worth noting that the doublet at 163.7 eV was not detected by regular XPS analysis at ambient temperature, which further confirms the formation of elemental sulfur as elemental sulfur is unstable in ultrahigh vacuum at ambient temperature. Therefore, the oxidation product at the potential of 0.45 V is mainly elemental sulfur, but the presence of metal-deficient lead sulfide or polysulfides cannot be ruled out.

The typical topographic images and corresponding current distributions of potentiostatically treated galena surface at -0.7 V, 0 V and 0.3 V are shown in Figures 4.6A, 4.6B and 4.6C, respectively, which were obtained at the same region to illustrate the variation of current distribution with the electrochemical potential. At -0.7 V, the surface composition is lead sulfide as confirmed by cryo-XPS in Figure 4.5. It is well known that lead sulfide is a semiconductor material with a small band gap of about 0.4 eV,³⁶ so there would be a current flow between the conductive tip and galena surface. It is worth noting that the higher current in certain locations on the surface is due to the deep cleavage steps (as also reflected in the corresponding topographic images in Figure 4.6) that enhance the electrical contact area between the conductive tip and galena surface. The current strength decreased with increasing the potential from -0.7 V to 0 V and 0.45 V, suggesting that the increased thickness of sulfur-rich layer due to oxidation with poor electrical conductivity limited the current flow. With the solvation of lead ions under the applied potential of 0 V, sulfur atoms would still occupy their original lattice positions, leading to the formation of compact metal-deficient lead sulfide layer. Due to the reduced

content of lead atoms in the lattice, the electric conductivity decreased. With the applied potential increasing to 0.45 V, the nonconductive elemental sulfur formed within the metal-deficient lead sulfide layer, thereby further decreasing the electric conductivity. The uniform current distribution images obtained by conductive AFM over the surface at each potential indicate homogeneous electrochemical reactions, which is consistent with the topographic imaging results in Figures 4.4 and 4.6.

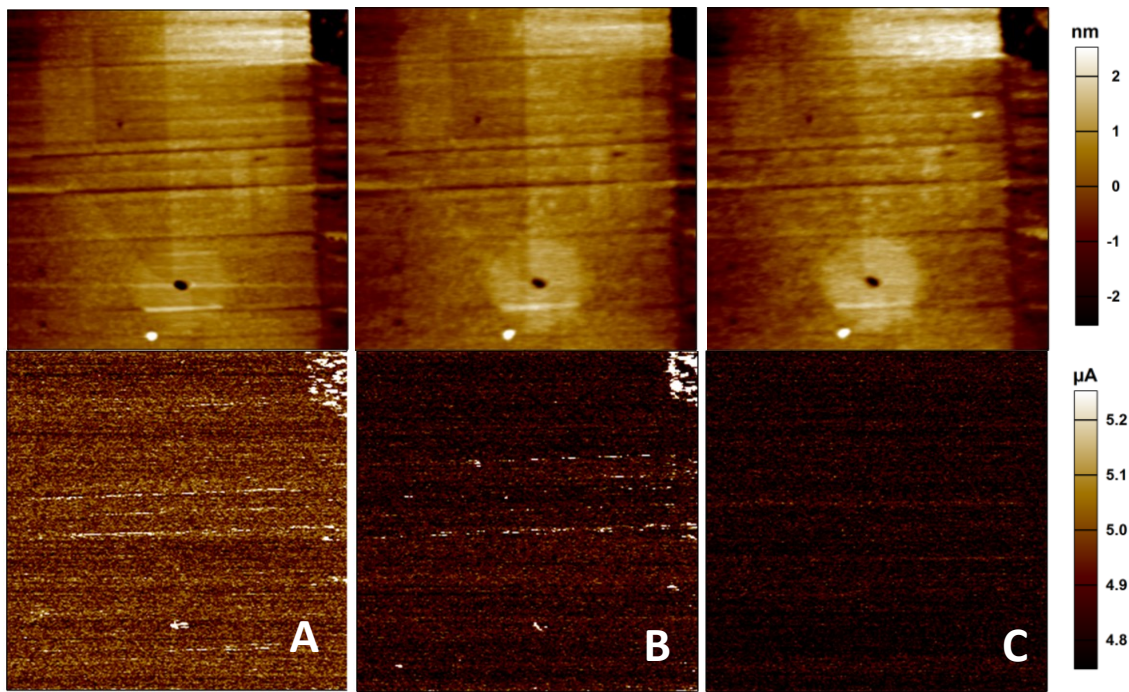


Figure 4.6 The topographic images and corresponding current distributions ($2 \times 2 \mu\text{m}^2$) of potentiostatically treated galena surface at the electrochemical potential of (A) -0.7 V, (B) 0 V and (C) 0.45 V.

4.3.5 AFM force measurements

Figure 4.7 shows the interaction force profile between silicon nitride AFM tip and galena surface potentiostatically treated at various electrochemical potentials in 0.5 M NaCl. The wetting behavior of water on silicon nitride cantilevers indicates that the

silicon nitride cantilevers are hydrophilic with a water contact angle less than 5° . In concentrated salt solution, the EDL is significantly suppressed and EDL force is negligible. Hence, the hydrophilic AFM tip-galena surface interaction is governed by VDW force. The Hamaker constant for Si_3N_4 -water-PbS was calculated as 6.3×10^{-20} J which was used to analyze the measured forces between silicon nitride tip and galena surface.^{27, 53-55} The measured force curves at electrochemical potential ranging from -0.7 V to 0.45 V (open symbols) almost overlap and show the same attraction at a separation distance of ~ 6 nm during approach, which agree well with the calculations based on the classical DLVO theory (red curve), indicating that the effect of thin sulfur-rich oxidation layer on VDW interaction between hydrophilic silicon nitride tip and galena surface can be neglected. The discrepancy at separation distance below 2 nm is mainly due to the effects of surface roughness and hydration.^{21, 28}

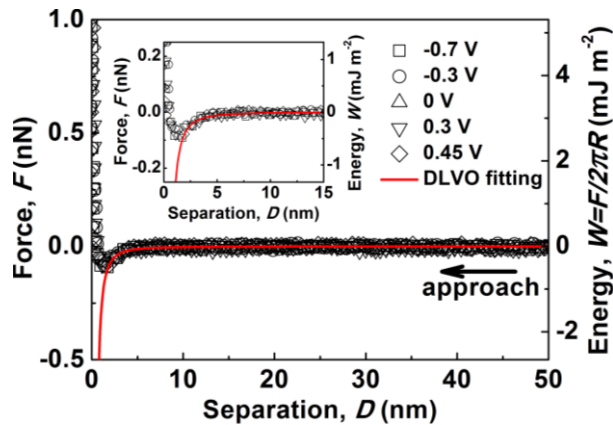


Figure 4.7 The interaction force F (left axis) between silicon nitride AFM tip and galena surface potentiostatically treated at various electrochemical potentials in 0.5 M NaCl and the corresponding interaction energy (W) per unit area between two flat surfaces (right axis) given by $W = F/2\pi R$ as a function of separation distance (D). The inset shows zoomed-in view

at short separation. Experiment results are shown in open symbols, and DLVO calculations are shown in red curve.

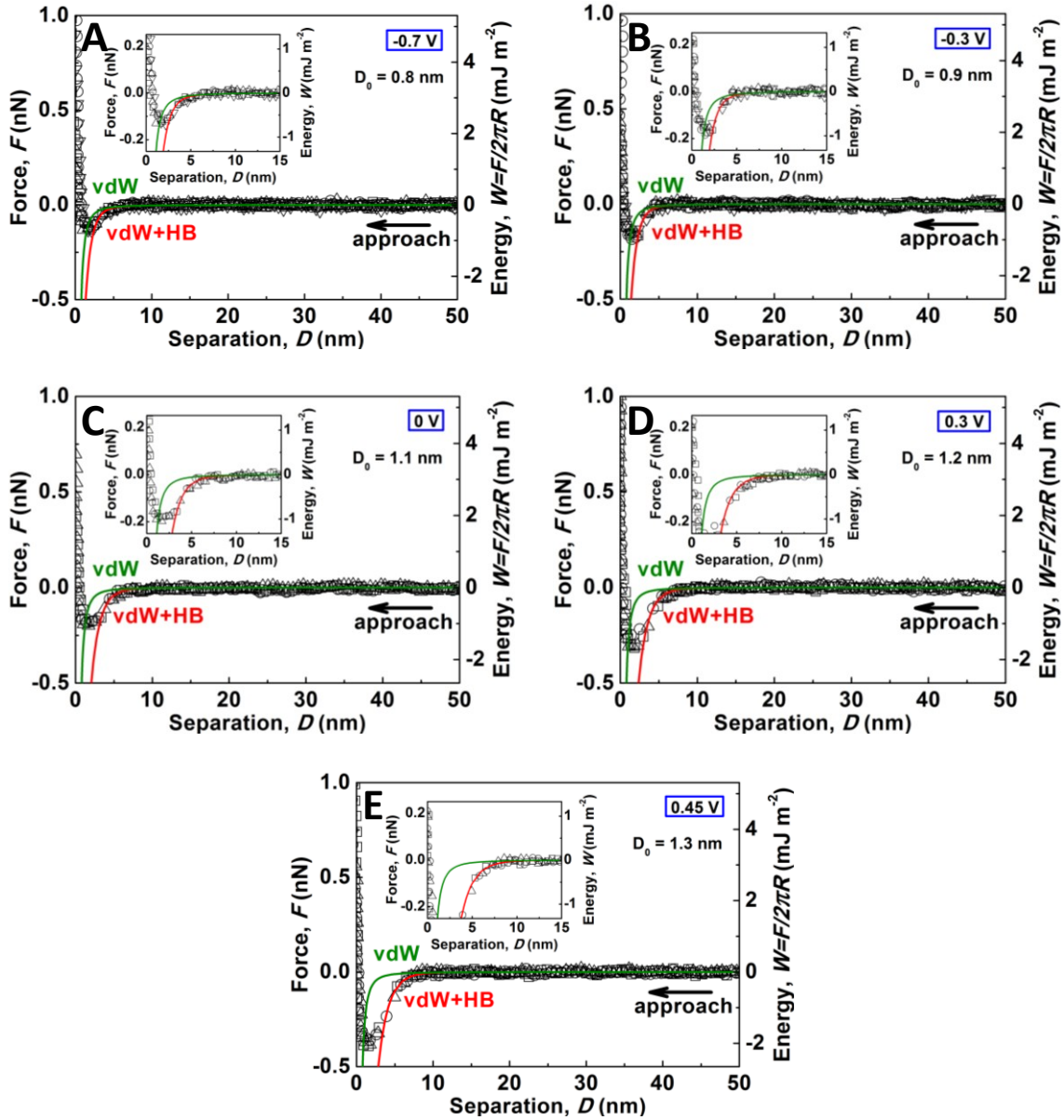


Figure 4.8 The interaction force F (left axis) between the hydrophobic OTS modified tip and galena surface potentiostatically treated at the electrochemical potential of (A) -0.7 V, (B) -0.3 V, (C) 0 V, (D) 0.3 V, and (E) 0.45 V in 0.5 M NaCl, and the corresponding interaction energy (W) per unit area between two flat surfaces (right axis) given by $W = F/2\pi R$

as a function of separation distance (D). The inset shows zoomed-in view at short separation. Experiment results are shown in open symbols, and theoretical calculations based on VDW interaction and the extended DLVO model including the effect of hydrophobic interaction (HB) are shown in green curves and red curves, respectively.

Figure 4.8 shows the interaction between OTS functionalized AFM tip and galena surface potentiostatically treated at various electrochemical potentials in 0.5 M NaCl. As illustrated in Figure 4.8A, the hydrophobic tip jumped into contact with galena surface at a separation distance of ~ 6.2 nm during approach at -0.7 V. The coated OTS layer was very thin (1-2 nm as reported previously), and the effect of OTS layer on VDW interaction could be neglected at separation larger than 3 nm.^{31, 51} It is evident that the measured attraction (open symbols) is much stronger than that contributed by the VDW interaction (green curve). Therefore, the attractive interaction that led to the “jump-in” behavior should arise from the hydrophobic interaction. By fitting the measured force profile with the extended DLVO theory by including the effect of hydrophobic interaction (red curve), the decay length D_0 of hydrophobic force was determined to be 0.8 nm.

As the electrochemical potential rose to -0.3 V (Figure 4.8B), 0 V (Figure 4.8C), 0.3 V (Figure 4.8D) and 0.45 V (Figure 4.8E) for the treatment of galena surface, the “jump-in” distance increased to ~ 6.7 , ~ 7.9 , ~ 8.4 and ~ 9.2 nm, from which the decay length D_0 of hydrophobic interaction was determined to be 0.9, 1.1, 1.2 and 1.3 nm, respectively. The enhanced “jump-in” distance and fitted decay length D_0 of hydrophobic interaction indicate that the attraction became stronger and extended to longer range,

which agrees with the results in Figure 4.3 that the galena surface became more hydrophobic by contact angle measurements with increasing the electrochemical potential. Although the exact physical origin of hydrophobic interaction is still under debate, it is generally accepted that the hydrophobic interaction is closely related to the entropic effect originating from the disruption of the hydrogen bonding network between water molecules near the hydrophobic surface.^{21, 24, 52} The increased decay length of hydrophobic interaction with increasing the electrochemical potential may suggest that the mobility of more water molecules is restricted and water correlations at the vicinity of mineral solid/water interface become longer-range due to the oxidation of lead sulfide to metal-deficient lead sulfide and elemental sulfur.

Figure 4.9 shows the histograms of measured adhesion F_{adh}/R during separation of the hydrophobic AFM tip and galena surface potentiostatically treated at different electrochemical potentials. With the potential increasing from -0.7 V to -0.3, 0, 0.3 and 0.45 V, the average adhesion increased from 63.00 mN/m to 69.94, 98.95, 117.25 and 146.17 mN/m, respectively. The work of adhesion per unit area W_{adh} for two flat surfaces is correlated to the measured adhesion F_{adh}/R by the Derjaguin-Muller-Toporov (DMT) model given by Equation 4.5.

$$W_{adh} = -\frac{1}{2\pi} F_{adh} / R \quad (4.5)$$

The adhesion measured could be contributed by various factors including VDW interactions and possibly hydrophobic effects. It is noted that the contribution of VDW interaction to the work of adhesion should not change significantly between the hydrophobic AFM tip and galena surface potentiostatically treated at different electrochemical potentials. Therefore, the enhanced adhesion with increasing applied

potential (Figure 4.9) should be most likely contributed by “hydrophobic” attraction.⁵³⁻⁵⁴ As a first approximation, the contribution of hydrophobic attraction to the work of adhesion $W_{\text{HB,adh}}$ can be estimated by taking distance $D = 0$ in Equation 4.2: $W_{\text{HB,adh}} = -(F_{\text{adh}}/R)/2\pi = -C/2\pi$. Therefore, in this work, the constant C of hydrophobic interaction in Equation 4.2 would be closely related to the adhesion F_{adh}/R measured, as also evident from the results that the increased values of the fitted constant C with increasing applied potential in Figure 4.8 show the same trend as the adhesion F_{adh}/R measured shown in Figure 4.9. The above results demonstrate that increasing the applied potential, within the range tested, in electrochemical treatment of galena surface can significantly enhance its hydrophobic interaction with other hydrophobic surfaces or molecules, which have implications in mineral flotation.

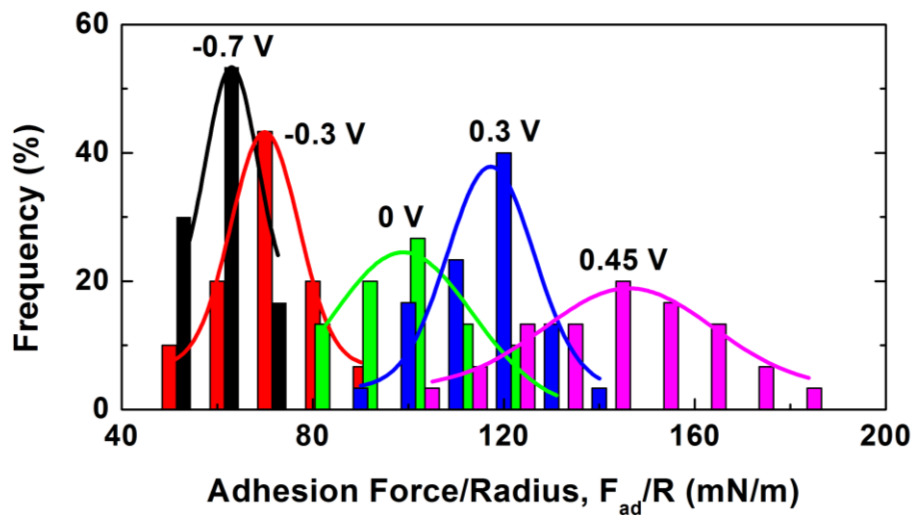


Figure 4.9 The histograms of measured adhesion F_{ad}/R and the fitted Gaussian distributions between the hydrophobic OTS modified AFM tip and galena surface potentiostatically treated at different electrochemical potentials.

4.4 Conclusions

Interfacial electrochemical processes play important roles in a wide range of engineering applications, such as base metal sulfide flotation. In this work, the evolution of surface characteristics (e.g. morphological changes and surface interactions) of a model mineral galena were probed at the nanoscale with simultaneous modulation of interfacial chemical reaction using an EC-AFM. In situ topographic imaging revealed the slight surface roughening of galena at an applied potential of 0 V (0.206 V vs SHE) and more pronounced surface roughening at higher potentials such as 0.3 V and 0.45 V. The interaction forces between electrochemically treated galena and a hydrophobic OTS functionalized AFM tip showed long-range attraction with “jump-in” distance increasing with increasing applied potential from -0.7 V to 0.45 V due to the enhanced surface hydrophobicity as confirmed by contact angle measurements, which can be well fitted by the extended DLVO theory by including the effect of hydrophobic force. It was found that the decay length of hydrophobic interaction increased from 0.8 nm to 1.3 nm with increasing applied potential from -0.7 V to 0.45 V. The electrochemical oxidation at 0 V arose from the formation of metal-deficient lead sulfide, while the formation of elemental sulfur at 0.45 V (0.656 V vs SHE) was further confirmed by cryo-XPS. This work shows a useful methodology for probing the interfacial properties and surface interaction mechanisms on electrochemically polarized mineral surfaces at nanoscale, which can be extended to many other interfacial electrochemical processes such as electrocatalysis and electrochemical energy storage.

4.5 Acknowledgements

We gratefully acknowledge the financial support from the Natural Sciences and Engineering Research Council of Canada (NSERC), Canadian Centre for Clean Coal/Carbon and Mineral Processing Technologies (C⁵MPT), the Canada Foundation for Innovation (CFI) and the Alberta Advanced Education & Technology Small Equipment Grants Program (AET/SEGP).

4.6 References

1. Park, J. Y. *Current Trends of Surface Science and Catalysis*; Springer Science & Business Media: New York, **2014**.
2. Roucoux, A.; Schulz, J.; Patin, H. Reduced Transition Metal Colloids: A Novel Family of Reusable Catalysts? *Chem. Rev.* **2002**, *102*, 3757-3778.
3. Frey, N. A.; Peng, S.; Cheng, K.; Sun, S. Magnetic Nanoparticles: Synthesis, Functionalization, and Applications in Bioimaging and Magnetic Energy Storage. *Chem. Soc. Rev.* **2009**, *38*, 2532-2542.
4. Feng, X. *Nanocarbons for Advanced Energy Storage*; John Wiley & Sons: Weinheim, **2015**.
5. Leja, J. *Surface Chemistry of Froth Flotation*; Plenum Press: New York, **1982**.
6. Farrokhpay, S. The Significance of Froth Stability in Mineral Flotation-a Review. *Adv. Colloid Interface Sci.* **2011**, *166*, 1-7.
7. Smith, M. C.; Gilbert, J. A.; Mawdsley, J. R.; Seifert, S. N.; Myers, D. J. In Situ Small-Angle X-Ray Scattering Observation of Pt Catalyst Particle Growth During Potential Cycling. *J. Am. Chem. Soc.* **2008**, *130*, 8112-8113.

8. Raimondi, F.; Scherer, G. G.; Kötzt, R.; Wokaun, A. Nanoparticles in Energy Technology: Examples from Electrochemistry and Catalysis. *Angew. Chem. Int. Ed.* **2005**, *44*, 2190-2209.
9. Hu, Y.; Sun, W.; Wang, D. *Electrochemistry of Flotation of Sulphide Minerals*; Springer Science & Business Media: Berlin, **2009**.
10. Tolley, W.; Kotlyar, D.; Van Wagoner, R. Fundamental Electrochemical Studies of Sulfide Mineral Flotation. *Miner. Eng.* **1996**, *9*, 603-637.
11. Buckley, A.; Woods, R. X-Ray Photoelectron Spectroscopic and Electrochemical Studies of the Interaction of Xanthate with Galena in Relation to the Mechanism Proposed by Page and Hazell. *Int. J. Miner. Process.* **1990**, *28*, 301-311.
12. Nowak, P.; Laajalehto, K.; Kartio, I. A Flotation Related X-Ray Photoelectron Spectroscopy Study of the Oxidation of Galena Surface. *Colloids Surf., A* **2000**, *161*, 447-460.
13. Shapter, J.; Brooker, M.; Skinner, W. M. Observation of the Oxidation of Galena using Raman Spectroscopy. *Int. J. Miner. Process.* **2000**, *60*, 199-211.
14. Turcotte, S.; Benner, R.; Riley, A.; Li, J.; Wadsworth, M.; Bodily, D. Surface Analysis of Electrochemically Oxidized Metal Sulfides using Raman Spectroscopy. *J. Electroanal. Chem.* **1993**, *347*, 195-205.
15. Leppinen, J.; Basilio, C.; Yoon, R.-H. In-Situ FTIR Study of Ethyl Xanthate Adsorption on Sulfide Minerals under Conditions of Controlled Potential. *Int. J. Miner. Process.* **1989**, *26*, 259-274.
16. Chernyshova, I. In Situ FTIR-Spectroelectrochemical Study of the Anodic Processes on a Galena (PbS) Electrode under Open-Air Conditions in the Absence and Presence of

N-Butyl Xanthate. *Langmuir* **2002**, *18*, 6962-6968.

17. Brinen, J.; Greenhouse, S.; Nagaraj, D.; Lee, J. SIMS and SIMS Imaging Studies of Adsorbed Dialkyl Dithiophosphinates on PbS Crystal Surfaces. *Int. J. Miner. Process.* **1993**, *38*, 93-109.

18. Smart, R. S. C.; Jasieniak, M.; Prince, K.; Skinner, W. SIMS Studies of Oxidation Mechanisms and Polysulfide Formation in Reacted Sulfide Surfaces. *Miner. Eng.* **2000**, *13*, 857-870.

19. Eggleston, C. M.; Hochella, M. F. Scanning Tunneling Microscopy of Galena (100) Surface Oxidation and Sorption of Aqueous Gold. *Science* **1991**, *254*, 983-986.

20. Kim, B. S.; Hayes, R. A.; Prestidge, C. A.; Ralston, J.; Smart, R. S. C. Scanning Tunneling Microscopy Studies of Galena: The Mechanisms of Oxidation in Aqueous Solution. *Langmuir* **1995**, *11*, 2554-2562.

21. Israelachvili, J. N. *Intermolecular and Surface Forces, revised 3rd ed.*; Academic press: New York, **2011**.

22. Israelachvili, J.; Min, Y.; Akbulut, M.; Alig, A.; Carver, G.; Greene, W.; Kristiansen, K.; Meyer, E.; Pesika, N.; Rosenberg, K. Recent Advances in the Surface Forces Apparatus (SFA) Technique. *Rep. Prog. Phys.* **2010**, *73*, 036601.

23. Zeng, H.; Tian, Y.; Anderson, T. H.; Tirrell, M.; Israelachvili, J. N. New SFA Techniques for Studying Surface Forces and Thin Film Patterns Induced by Electric Fields. *Langmuir* **2008**, *24*, 1173-1182.

24. Israelachvili, J.; Pashley, R. The Hydrophobic Interaction Is Long Range, Decaying Exponentially with Distance. *Nature* **1982**, *300*, 341-342.

25. Israelachvili, J. N.; Pashley, R. M. Molecular Layering of Water at Surfaces and

- Origin of Repulsive Hydration Forces. *Nature* **1983**, *306*,249-250.
26. Israelachvili, J. N.; McGuiggan, P. M. Forces between Surfaces in Liquids. *Science* **1988**, *241*, 795-800.
27. Ducker, W. A.; Senden, T. J.; Pashley, R. M. Direct Measurement of Colloidal Forces using an Atomic Force Microscope. *Nature* **1991**, *353*, 239-241.
28. Butt, H.-J.; Cappella, B.; Kappl, M. Force Measurements with the Atomic Force Microscope: Technique, Interpretation and Applications. *Surf. Sci. Rep.* **2005**, *59*, 1-152.
29. Yang, D.; Xie, L.; Bobicki, E.; Xu, Z.; Liu, Q.; Zeng, H. Probing Anisotropic Surface Properties and Interaction Forces of Chrysotile Rods by Atomic Force Microscopy and Rheology. *Langmuir* **2014**, *30*, 10809-10817.
30. Xie, L.; Shi, C.; Wang, J.; Huang, J.; Lu, Q.; Liu, Q.; Zeng, H. Probing the Interaction between Air Bubble and Sphalerite Mineral Surface using Atomic Force Microscope. *Langmuir* **2015**, *31*, 2438-2446.
31. Shi, C.; Cui, X.; Xie, L.; Liu, Q.; Chan, D. Y.; Israelachvili, J. N.; Zeng, H. Measuring Forces and Spatiotemporal Evolution of Thin Water Films between an Air Bubble and Solid Surfaces of Different Hydrophobicity. *ACS nano* **2014**, *9*, 95-104.
32. Shi, C.; Zhang, L.; Xie, L.; Lu, X.; Liu, Q.; Mantilla, C. A.; van den Berg, F. G.; Zeng, H. Interaction Mechanism of Oil-in-Water Emulsions with Asphaltenes Determined using Droplet Probe AFM. *Langmuir* **2016**, *32*, 2302-2310.
33. Wang, J.; Li, J.; Xie, L.; Shi, C.; Liu, Q.; Zeng, H. Interactions between Elemental Selenium and Hydrophilic/Hydrophobic Surfaces: Direct Force Measurements Using AFM. *Chem. Eng. J.* **2016**, *303*, 646-654.
34. Cui, X.; Shi, C.; Xie, L.; Liu, J.; Zeng, H. Probing Interactions between Air Bubble

and Hydrophobic Polymer Surface: Impact of Solution Salinity and Interfacial Nanobubbles. *Langmuir* **2016**, *32*, 11236-11244.

35. Valtiner, M.; Banquy, X.; Kristiansen, K.; Greene, G. W.; Israelachvili, J. N. The Electrochemical Surface Forces Apparatus: The Effect of Surface Roughness, Electrostatic Surface Potentials, and Anodic Oxide Growth on Interaction Forces, and Friction between Dissimilar Surfaces in Aqueous Solutions. *Langmuir* **2012**, *28*, 13080-13093.

36. Wittstock, G.; Kartio, I.; Hirsch, D.; Kunze, S.; Szargan, R. Oxidation of Galena in Acetate Buffer Investigated by Atomic Force Microscopy and Photoelectron Spectroscopy. *Langmuir* **1996**, *12*, 5709-5721.

37. Hampton, M. A.; Plackowski, C.; Nguyen, A. V. Physical and Chemical Analysis of Elemental Sulfur Formation During Galena Surface Oxidation. *Langmuir* **2011**, *27*, 4190-4201.

38. Reid, O. G.; Munechika, K.; Ginger, D. S. Space Charge Limited Current Measurements on Conjugated Polymer Films using Conductive Atomic Force Microscopy. *Nano letters* **2008**, *8*, 1602-1609.

39. Tan, S.; Tang, Z.; Liang, X.; Kotov, N. A. Resonance Tunneling Diode Structures on CdTe Nanowires Made by Conductive AFM. *Nano Letters* **2004**, *4*, 1637-1641.

40. Zhang, L.; Mitani, Y. Structural and Electrical Evolution of Gate Dielectric Breakdown Observed by Conductive Atomic Force Microscopy. *Appl. Phys. Lett.* **2006**, *88*, 032906.

41. Balke, N.; Winchester, B.; Ren, W.; Chu, Y. H.; Morozovska, A. N.; Eliseev, E. A.; Huijben, M.; Vasudevan, R. K.; Maksymovych, P.; Britson, J. Enhanced Electric

- Conductivity at Ferroelectric Vortex Cores in BiFeO₃. *Nature Physics* **2012**, *8*, 81-88.
42. Xu, D.; Watt, G. D.; Harb, J. N.; Davis, R. C. Electrical Conductivity of Ferritin Proteins by Conductive AFM. *Nano letters* **2005**, *5*, 571-577.
43. Headrick, J. E.; Berrie, C. L. Alternative Method for Fabricating Chemically Functionalized Afm Tips: Silane Modification of HF-Treated Si₃N₄ Probes. *Langmuir* **2004**, *20*, 4124-4131.
44. Hutter, J. L.; Bechhoefer, J. Calibration of Atomic - Force Microscope Tips. *Rev. Sci. Instrum.* **1993**, *64*, 1868-1873.
45. Drelich, J.; Long, J.; Yeung, A. Determining Surface Potential of the Bitumen - Water Interface at Nanoscale Resolution Using Atomic Force Microscopy. *Can. J. Chem. Eng.* **2007**, *85*, 625-634.
46. Shi, C.; Chan, D. Y.; Liu, Q.; Zeng, H. Probing the Hydrophobic Interaction between Air Bubbles and Partially Hydrophobic Surfaces Using Atomic Force Microscopy. *J. Phys. Chem. C* **2014**, *118*, 25000-25008.
47. Shi, C.; Cui, X.; Xie, L.; Liu, Q.; Chan, D. Y.; Israelachvili, J. N.; Zeng, H. Measuring Forces and Spatiotemporal Evolution of Thin Water Films between an Air Bubble and Solid Surfaces of Different Hydrophobicity. *ACS nano* **2014**, *9*, 95-104.
48. Buckley, A. N.; Woods, R. An X-Ray Photoelectron Spectroscopic Study of the Oxidation of Galena. *Appl. Surf. Sci.* **1984**, *17*, 401-414.
49. Richardson, P.; Yoon, R.-H.; Woods, R.; Buckley, A. The Photoelectrochemistry of Galena. *Int. J. Miner. Process.* **1994**, *41*, 77-97.
50. Chen, J.; Long, X.; Chen, Y. Comparison of Multilayer Water Adsorption on the Hydrophobic Galena (PbS) and Hydrophilic Pyrite (FeS₂) Surfaces: A DFT Study. *J. Phys.*

Chem. C **2014**, *118*, 11657-11665.

51. Tsukruk, V. V.; Bliznyuk, V. N. Adhesive and Friction Forces between Chemically Modified Silicon and Silicon Nitride Surfaces. *Langmuir* **1998**, *14*, 446-455.

52. Meyer, E. E.; Rosenberg, K. J.; Israelachvili, J. Recent Progress in Understanding Hydrophobic Interactions. *Proc. Natl. Acad. Sci. U. S. A.* **2006**, *103*, 15739-15746.

53. Christenson, H. K.; Claesson, P. M. Direct Measurements of the Force between Hydrophobic Surfaces in Water. *Adv. Colloid Interface Sci.* **2001**, *91*, 391-436.

54. Zeng, H.; Shi, C.; Huang, J.; Li, L.; Liu, G.; Zhong, H. Recent Experimental Advances on Hydrophobic Interactions at Solid/Water and Fluid/Water Interfaces. *Biointerphases* **2016**, *11*, 018903.

Chapter 5 Probing the Interaction between Air Bubble and Sphalerite Mineral Surface using Atomic Force Microscopy

5.1 Introduction

The interaction between air bubbles and solid surfaces determines the bubble-solid attachment efficiency in many engineering processes,¹⁻² such as mining and froth flotation,³ wastewater treatment,⁴ and flotation deinking.⁵ In mineral flotation, mineral particles with varying surface hydrophobicity are selectively separated based on their attachment propensities to air bubbles.¹⁻² The bubble-solid attachment is governed by the drainage process of the intervening liquid film under the combined influence of hydrodynamic pressure and disjoining pressure arising from different surface forces including van der Waals (VDW), electrical double layer (EDL), and hydrophobic interactions.⁶⁻⁸ The bubble-mineral attachment process has attracted much attention,⁹⁻¹¹ yet the basic understanding of the surface interaction mechanism and thin film drainage process still remains limited, particularly for the interaction between air bubbles and mineral surfaces of different hydrophobicity under various hydrodynamic conditions, which might be probed by direct force measurements.

Over the last few decades, significant progress has been achieved with respect to the force measurements between two solid surfaces using surface forces apparatus (SFA) and atomic force microscopy (AFM).¹²⁻²³ However, direct force measurements involving deformable objects such as air bubbles were far more complicated than that of solid

surfaces due to the experimental difficulties and interpretation of the results.²⁴⁻²⁶ In early studies by Ducker et al.²⁷ and Fielden et al.²⁸, a silica colloidal probe was driven towards a large air bubble immobilized on a hydrophobic substrate at a very low approaching velocity, in which the impact of hydrodynamic force was assumed to be negligible as compared to surface forces. Strong attraction was observed between air bubble and hydrophobic particle, while hydrophilic particle was strongly repelled by air bubble.²⁸ The deformation of the bubble was calculated based on the assumption that air bubble behaves as a linear Hookean spring with an effective spring constant equal to surface tension of water,²⁷ which was later proven to actually follow a nonlinear nature especially under high interaction force.^{8, 29-32}

The recently developed AFM bubble probe technique enables direct force measurements between two air bubbles or between an air bubble and solid surfaces.^{8, 29-30, 33-40} The measured forces could be successfully described by a theoretical model based on Reynolds lubrication theory and augmented Young-Laplace equation.³³⁻³⁵ It was found that repulsive VDW force could successfully inhibit bubble attachment onto smooth hydrophilic surfaces (e.g. mica, silica and gold),^{36-37, 39-40} and hydrophobic interaction plays a critical role in bubble attachment onto hydrophobized mica surface.³⁹⁻⁴⁰

To date, no study has been reported on direct force measurements between air bubbles and mineral surfaces (e.g. sulfide minerals) except mica and silica aforementioned, especially under different bubble approaching velocities or hydrodynamic conditions. Mineral particles typically have irregular shapes and rough surfaces, which limits the application of the conventional colloidal probe method for measuring the interaction forces between mineral particles and surface-supported bubbles.

Nevertheless, many minerals exhibit almost perfect cleavage which allows the preparation of smooth surfaces by fracturing along the cleavage plane, therefore it is possible to extend the AFM bubble probe technique to directly probe their interaction forces with cantilever-attached bubbles.

In this work, sphalerite, consisting largely of zinc sulfide, was chosen as a model sulfide mineral with perfect dodecahedral cleavage on the (110) crystal plane for generating molecularly smooth surface to be used for force measurements with a cantilever-attached bubble.⁴¹ The interaction between air bubble and sphalerite surfaces under various hydrodynamic conditions is directly probed using the AFM bubble probe technique. A theoretical model was used to first fit the interaction force under a low approaching velocity of the bubble to determine the fitting parameter, and then applied to predict the interaction forces under other hydrodynamic conditions for comparison with experiment results. The effects of conditioning treatment (e.g. copper activation and xanthate adsorption) and solution conditions (e.g. solution ionic strength) on the bubble-mineral interaction were also investigated. This work provides useful information and new insights into the understanding of basic interaction mechanism between air bubbles and mineral particles in mineral flotation at the nanoscale.

5.2 Materials and methods

5.2.1 Materials

Sodium chloride (NaCl, ACS reagent grade), calcium chloride (CaCl₂, ACS reagent grade), calcium sulfate hemihydrates (CaSO₄·0.5H₂O, ACS reagent grade), magnesium chloride hexahydrate (MgCl₂·6H₂O, ACS reagent grade), sodium sulfate

(Na_2SO_4 , ACS reagent grade), potassium chloride (KCl, ACS reagent grade) and cupric sulfate pentahydrate ($\text{CuSO}_4 \cdot 5\text{H}_2\text{O}$, ACS reagent grade) were purchased from Fisher Scientific and used as received without further purification. Potassium amyl xanthate (PAX, $\text{C}_6\text{H}_{11}\text{OS}_2\text{K}$, Prospec Chemicals Ltd., Canada) was purified by adding 100 g of xanthate into 1 L of acetone under stirring at 40 °C for several minutes, and then precipitated in ether following an established method.⁴² All aqueous solutions were prepared using Milli-Q water (Millipore deionized, 18.2 $\text{M}\Omega \cdot \text{cm}$ resistivity). Hydrochloric acid (HCl, ACS reagent grade) and sodium hydroxide (NaOH, ACS reagent grade) were purchased from Fisher Scientific and used to adjust solution pH. In this study, the pH of all the aqueous solutions was fixed at pH = 5.

5.2.2 Preparation of sphalerite surface

Sphalerite (Ward's Science, NY, USA) was fractured to obtain the natural cleavage surface that was then glued onto a freshly cleaved mica surface by epoxy with the fractured face exposed for testing. To remove surface oxidation layer, the freshly fractured sphalerite surface was washed in 0.01 M HCl solution for 5 minutes, rinsed by Milli-Q water, and then dried using high purity nitrogen.⁴³

Sphalerite is not sufficiently hydrophobic for spontaneous attachment to air bubbles in the absence of conditioning treatment, so chemical reagents such as copper sulfate and short-chain xanthate are widely used as activator and collector, respectively, to enhance the surface hydrophobicity of sphalerite.^{42, 44} Herein, sphalerite surface conditioned in 0.1 mM CuSO_4 solution at pH 5 for 5 minutes and subsequently in 0.5

mM PAX solution at pH 5 for 5 minutes, denoted as “conditioned sphalerite”, was used to investigate the effect of conditioning treatment on the bubble-sphalerite interaction.

5.2.3 Surface characterization

A contact angle goniometer (ramé-hart instrument Co., NJ, USA) was used to measure the static water contact angle of sample surfaces using a sessile drop method. For the same type of sample, at least two different surfaces and three different positions on each surface were tested, and the average water contact angle was reported. A MFP-3D AFM (Asylum Research, Santa Barbara, CA, USA) was used to characterize the surface topography and roughness of the samples. A Zetasizer Nano (Malvern Instruments Ltd., United Kingdom) was used to measure the zeta potential of sphalerite suspension under different solution conditions at pH 5.

5.2.4 Force measurements

Prior to the force measurements, the glass disk of a fluid cell was mildly hydrophobized by immersing in 10 mM octadecyltrichlorosilane (OTS) in toluene for ~10 s to give a water contact angle of 40°-60° for bubble immobilization. Custom-made rectangular silicon cantilevers (400×70×2 μm) with a circular gold patch (diameter 65 μm, thickness 30 nm) were strongly hydrophobized by immersing in 10 mM dodecanethiol in absolute ethanol overnight to provide higher hydrophobicity than the glass disk for bubble anchoring.³³ Air bubbles were immobilized on the glass disk of the fluid cell in aqueous solution by carefully purging air through a custom-made ultra-sharp glass pipette into the solution, and a bubble probe was then prepared by picking up an air bubble of

suitable size on the glass disk with the AFM cantilever. The spring constants of the cantilevers were determined to be 0.3-0.4 N/m using the Hutter and Bechhoefer method.⁴⁵ Figure 5.1A shows a typical optical microscope image (bottom-view) of a cantilever-attached bubble.

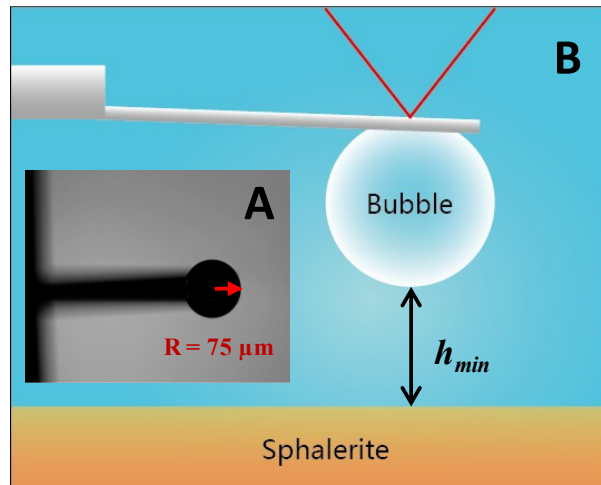


Figure 5.1 (A) Optical microscope image of a cantilever-attached bubble with radius of 75 μm which is used as an AFM bubble probe. (B) Schematic of force measurements between air bubble and sphalerite surface in aqueous solution using the AFM bubble probe. h_{min} is the minimum separation or minimum film thickness of the confined water film between air bubble and solid surface.

The interaction forces between the anchored air bubble and sample surfaces were measured in aqueous solutions (illustrated in Figure 5.1B) under a range of approaching velocity of the bubble from 1 to 50 $\mu\text{m/s}$. During the force measurements, the cantilever-attached bubble was positioned over a sample surface and then driven to approach the surface until a fixed deflection of the cantilever was reached or bubble attachment occurred. The deflection of the cantilever was detected through a laser beam that was

reflected from the cantilever to a photodiode detector, which was further converted to force using the spring constant and Hooke's law. The movement of the cantilever (viz. air bubble) and the corresponding interaction force were recorded as a function of time by AFM software.

5.2.5 Theoretical model

To describe the interaction between air bubble and solid surface, a theoretical model based on Reynolds lubrication theory coupled with augmented Young-Laplace equation was applied.^{8, 29-30, 33-40}

Assuming immobile boundary conditions at the air-water and water-substrate interfaces, the evolution of confined liquid film thickness $h(r, t)$ as a bubble approaches or retracts from the solid surface is governed by the Reynolds equation (also referred as Stefan-Reynolds equation⁴⁶⁻⁴⁷) shown in Equation 5.1.^{8, 29-30, 33-40}

$$\frac{\partial h}{\partial t} = \frac{1}{12\mu r} \frac{\partial}{\partial r} \left(rh^3 \frac{\partial p}{\partial r} \right) \quad (5.1)$$

where μ is the dynamic viscosity of water, r is the radial coordinate and $p(r, t)$ is the excess hydrodynamic pressure in the film relative to the bulk liquid. The immobile boundary condition was applied here as it is supported by the recent results of AFM force measurements involving air bubbles and also agrees with the experiment results in this work.^{8, 29-30, 33-40}

Assuming a constant interfacial tension, the deformation of the bubble under combined influence of hydrodynamic and disjoining pressure is described by the augmented Young-Laplace equation (Equation 5.2) that was derived by balancing the normal stress with the local curvature of the air-water interface.^{8, 29-30, 33-40}

$$\frac{\gamma}{r} \frac{\partial}{\partial r} \left(r \frac{\partial h}{\partial r} \right) = \frac{2\gamma}{R} - p - \Pi \quad (5.2)$$

where γ is the air-water interfacial tension, R is the radius of air bubble, and $\Pi(r, t)$ is the disjoining pressure that arises from various contributions of surface forces such as VDW, EDL and hydrophobic interactions.

The disjoining pressure component arising from VDW interaction Π_{VDW} and EDL interaction Π_{EDL} can be given by Equation 5.3 and Equation 5.4, respectively, where A_H is the non-retarded Hamaker constant for air-water-sphalerite,^{15, 48-49} κ^{-1} is the Debye length, and ψ_b and ψ_s are the surface potential of air bubble and the substrate, respectively.

$$\Pi_{VDW} = -\frac{A_H}{6\pi h^3} \quad (5.3)$$

$$\Pi_{EDL} = \frac{2\varepsilon_0\varepsilon\kappa^2 \left[(e^{+\kappa h} + e^{-\kappa h})\psi_b\psi_s - (\psi_b^2 + \psi_s^2) \right]}{(e^{+\kappa h} - e^{-\kappa h})^2} \quad (5.4)$$

The contribution of hydrophobic interaction to the disjoining pressure, Π_{HB} , was reported as an exponential expression (Equation 5.5),¹⁸ where D_0 is the decay length of hydrophobic interaction, and C is a constant (N/m) related to the static water contact angle θ on the substrate and water surface tension by Equation 5.6.³⁹⁻⁴⁰

$$\Pi_{HB} = -\frac{C}{2\pi D_0} e^{-h/D_0} \quad (5.5)$$

$$C = 2\pi\gamma(1 - \cos\theta) \quad (5.6)$$

The overall interaction force between air bubble and solid surface $F(t)$ is theoretically calculated by integrating the excess hydrodynamic pressure $p(r, t)$ and

disjoining pressure $\Pi(r, t)$ (Equation 5.7) based on an approach similar to the Derjaguin approximation.^{8, 29-30, 33-40}

$$F(t) = 2\pi \int_0^{\infty} (p(r, t) + \Pi(h(r, t))) r dr \quad (5.7)$$

5.3 Results and discussion

5.3.1 Surface characterization

Sphalerite surface is relatively hydrophilic with the static water contact angle of $\sim 35^\circ$. After conditioning treatment, the water contact angle rises to $\sim 85^\circ$, suggesting that the conditioned sphalerite surface becomes much more hydrophobic. The increased surface hydrophobicity is mainly due to the adsorption of xanthate as well as formation of hydrophobic species such as polysulfides and elemental sulfur on the surface after reagent treatment,⁴⁴ which allows the conditioned sphalerite particles more readily to attach to air bubbles in the flotation.

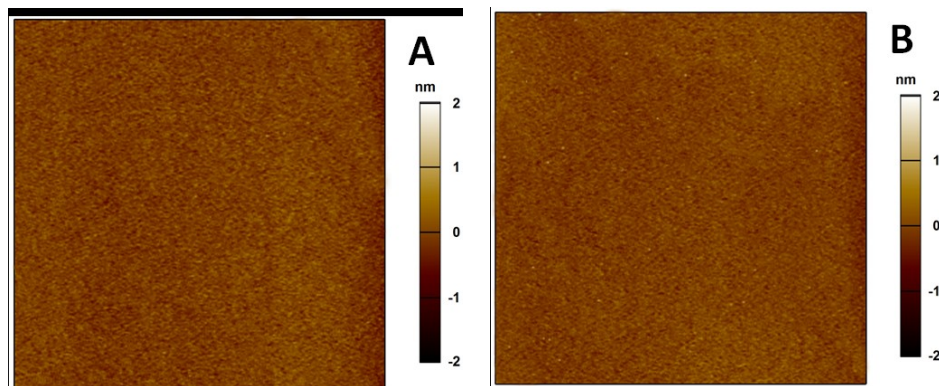


Figure 5.2 AFM topographic images ($5 \times 5 \mu\text{m}^2$) of (A) sphalerite surface and (B) conditioned sphalerite surface.

Typical AFM topographic images of sphalerite before and after conditioning treatment are shown in Figures 5.2A and 5.2B, respectively. The root-mean-square (rms) roughness is about 0.3 nm for sphalerite surface and slightly increases to 0.5 nm for the conditioned sphalerite surface, which indicates that a very smooth sphalerite surface was obtained by fracturing along the cleavage plane and the reagent conditioning treatment did not significantly change the roughness of the mineral surface.

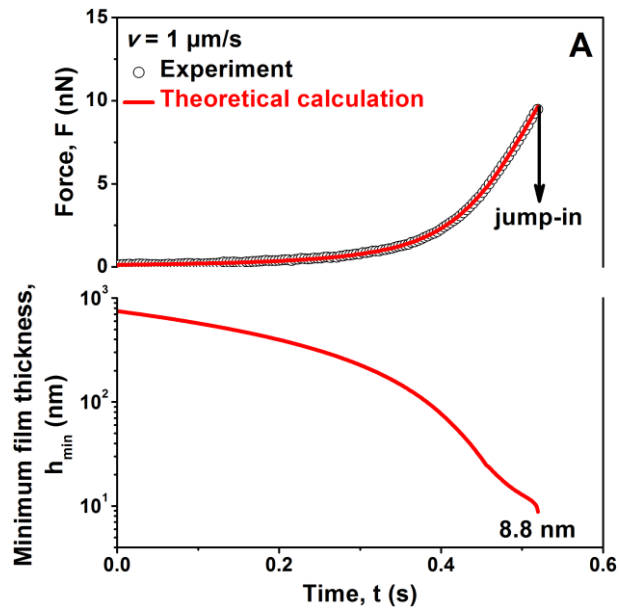
5.3.2 Bubble-sphalerite interaction in 500 mM NaCl solution

Figure 5.3 (open symbols) shows the measured interaction forces between an air bubble of radius 75 μm and a sphalerite surface in 500 mM NaCl solution under different bubble approaching velocities (i.e. $v = 1, 10$ and $30 \mu\text{m/s}$). The force curves show “jump-in” behavior under a lower approaching velocity where the force drastically turns from positive (repulsion) to negative (attraction) and no “jump-in” occurs under a higher approaching velocity. The “jump-in” indicates that the bubble is attached onto solid surface.

The interaction between air bubble and sphalerite surface was first measured under a low approaching velocity ($v = 1 \mu\text{m/s}$) with negligible hydrodynamic force to understand the effects of surface forces. Figure 5.3A shows that the confined water film kept thinning until the bubble suddenly jumped into contact with sphalerite surface during approach. For the bubble-water-sphalerite system, the non-retarded Hamaker constant between air bubble and sphalerite in water is negative, and thus the VDW interaction is repulsive at any separation.^{15, 37} The EDL is significantly suppressed in 500 mM NaCl solution and EDL interaction can be neglected. Hence, the attractive force that

led to bubble attachment arises from hydrophobic interaction which is incorporated into the theoretical model by using Equations 5.5 and 5.6.

The constant C in Equation 5.6 is calculated to be 0.08 N/m for sphalerite surface with a water contact angle of 35° . By fitting the measured interaction force (shown as open symbols in Figure 5.3A) with the theoretical prediction based on Reynolds lubrication theory coupled with augmented Young-Laplace equation, the decay length D_0 of hydrophobic interaction is determined to be 1.0 ± 0.1 nm, and the theoretically fitted results are shown as the solid curve in Figure 5.3A. The corresponding minimum film thickness of the confined water film varying with time is also calculated and shown in Figure 5.3A, and the critical water film thickness right before the “jump-in” is calculated to be 8.8 nm.



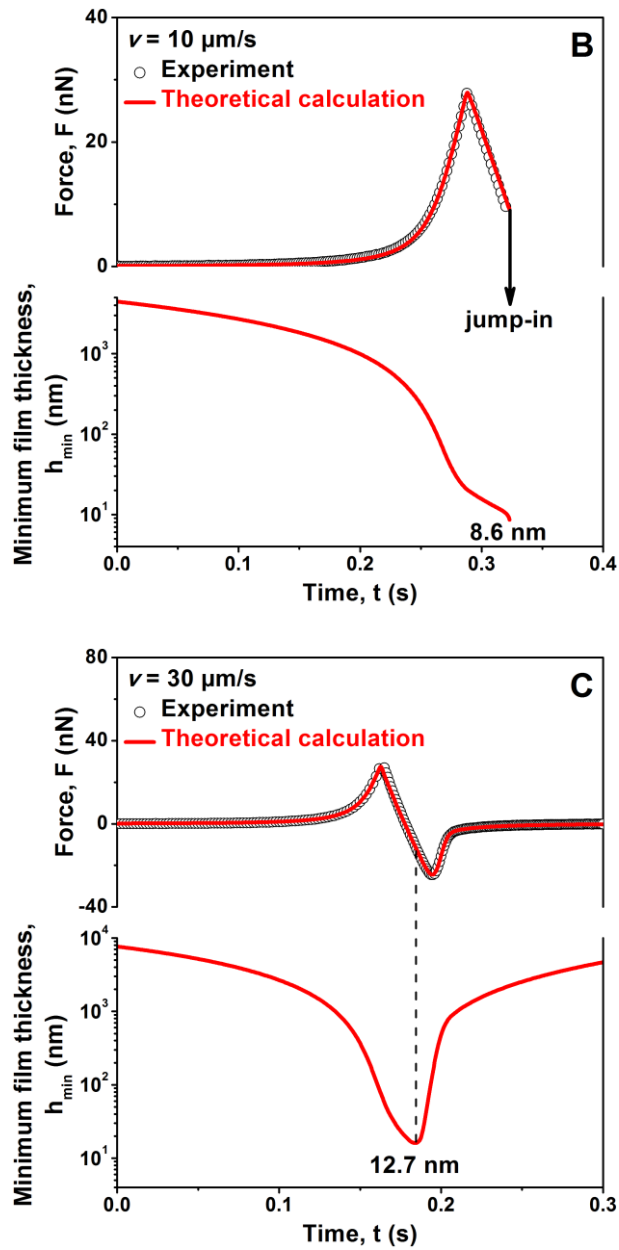


Figure 5.3 The interaction and the corresponding minimum film thickness of the confined water film as a function of time between an air bubble of radius $75 \mu\text{m}$ and a sphalerite surface in 500 mM NaCl solution under approaching velocity of (A) $v = 1 \mu\text{m/s}$, (B) $v = 10 \mu\text{m/s}$, and (C) $v = 30 \mu\text{m/s}$. Experiment results are shown in open symbols, and theoretical calculations are shown in solid curves. For all these figures, the constant C and the decay length D_0 used are 0.08 N/m and $1.0 \pm 0.1 \text{ nm}$, respectively.

With the velocity increasing to $v = 10 \mu\text{m/s}$ on approach of the bubble and sphalerite surface, the repulsion measured was stronger and increased more sharply than the $v = 1 \mu\text{m/s}$ case (Figure 5.3B), and the hydrodynamic force cannot be neglected and thus the film drainage process is governed by both the hydrodynamic force and surface forces. No “jump-in” occurred during approach, but interestingly bubble-sphalerite attachment was observed during retraction of the cantilever. The fitted decay length $D_0 = 1.0 \pm 0.1 \text{ nm}$ at $v = 1 \mu\text{m/s}$ is used to predict the interaction force and bubble attachment behavior at $v = 10 \mu\text{m/s}$, and theoretical calculation results for the force and minimum water film thickness are shown as solid curves in Figure 5.3B. It is evident that the theoretical prediction (solid curve) agrees very well with the experiment results (open symbols), which supports the feasibility of the theoretical model and prediction. The results on minimum water film thickness show that after the commencement of retraction, the confined water film continued thinning until it reached a critical thickness of 8.6 nm and the bubble suddenly jumped into contact with sphalerite surface. This phenomenon can be interpreted by the hydrodynamic suction effect as the water in the confined film continues to be drained out even after the retraction, which draws the bubble closer to solid surface.⁵⁰⁻⁵¹

Figure 5.3C shows the measured (open symbols) and theoretically predicted (solid curve) forces when the approaching velocity increases to $v = 30 \mu\text{m/s}$ for the bubble interacting with sphalerite surface. No bubble attachment was observed during the approach-retraction cycle. On approach, the repulsion increased as the water film thinned. On retraction, the repulsion decreased and then turned to attraction, while the confined water film continued thinning until a minimal film thickness of 12.7 nm was achieved, at

some point where the net force lied between the maximal repulsion during approach and the maximum attraction during retraction shown in Figure 5.3C, which is due to the hydrodynamic suction effect.⁵⁰⁻⁵¹ Therefore, at a high bubble approaching velocity, the hydrodynamic interaction plays an important role, and the attractive hydrophobic interaction is relatively too weak to induce rupture of the confined water film even at the minimum film thickness. Nevertheless, the theoretical prediction based on the classic Derjaguin–Landau–Verwey–Overbeek (DLVO) theory by including the hydrophobic interaction (Equations 5.5 and 5.6 using a decay length of $D_0 = 1.0 \pm 0.1$ nm) agrees well with the experimental measurements.

Therefore, it is evident from the above results that the approaching velocity of the bubble significantly affects the hydrodynamic force which together with surface forces play the critical role in bubble-mineral interaction and attachment.

5.3.3 The effect of conditioning treatment

The interaction forces between an air bubble of radius 75 μm and a conditioned sphalerite surface in 500 mM NaCl solution under different approaching velocities ($v = 1$ and 30 $\mu\text{m/s}$) are shown in Figure 5.4. The force curves show “jump-in” behavior even at a high approaching velocity (e.g. $v = 30$ $\mu\text{m/s}$) as compared to no “jump-in” at the same approaching velocity for the case of sphalerite surface, indicating that the bubble is more readily attached to the mineral surface after conditioning treatment. The adsorbed xanthate layer is very thin (~ 1 nm),⁵²⁻⁵⁴ and the effect of adsorbed xanthate on VDW interaction can be neglected at separation $D > 3$ nm. Thus the VDW interaction here is taken to be that of bubble-water-sphalerite system. The constant C in Equation 5.6 is

calculated to be 0.41 N/m for the conditioned sphalerite surface with a water contact angle of 85° . The decay length of hydrophobic interaction is determined as $D_0 = 1.5 \pm 0.1$ nm by fitting the experimental force results at a low approaching velocity $v = 1 \mu\text{m/s}$, and the calculated critical water film thickness before bubble attachment is 18.0 nm. The decay length of hydrophobic interaction and critical water film thickness are larger than that of the sphalerite case, indicating a stronger hydrophobic attraction for conditioned sphalerite with higher hydrophobicity ($\theta = 85^\circ$) as compared to that of sphalerite ($\theta = 35^\circ$). Figure 5.4 also shows that the theoretical prediction using the decay length of hydrophobic interaction $D_0 = 1.5 \pm 0.1$ nm agrees excellently with the experimental measurement at a high approaching velocity (e.g. $v = 30 \mu\text{m/s}$), in which bubble attachment did not occur on approach but was observed during retraction.

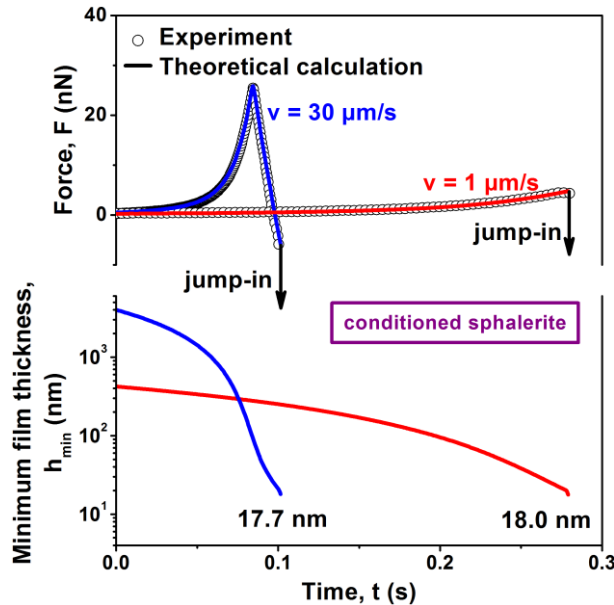


Figure 5.4 The interaction and the corresponding minimum film thickness of the confined water film as a function of time between an air bubble of radius $75 \mu\text{m}$ and a conditioned sphalerite surface in 500 mM NaCl solution under different approaching velocities $v = 1$ and $30 \mu\text{m/s}$ (open symbols for experiment results, and solid curves for

theoretical calculations). The constant C and the decay length D_0 used are 0.41 N/m and 1.5 ± 0.1 nm, respectively.

It is evident from the above results that hydrophobic attraction plays the critical role in bubble-mineral attachment. For the bubble-mineral interaction in 500 mM NaCl here, the overall disjoining pressure includes the repulsive VDW disjoining pressure and attractive hydrophobic disjoining pressure. Figure 5.5 shows the VDW disjoining pressure, hydrophobic disjoining pressure and the overall disjoining pressure for the interactions of bubble-water-sphalerite and bubble-water-conditioned sphalerite in Figures 5.3 and 5.4, which clearly shows that conditioned sphalerite exhibits stronger and longer range attractive disjoining pressure and bubble attachment occurs when the overall disjoining pressure just exceeds the Laplace pressure of the bubble.

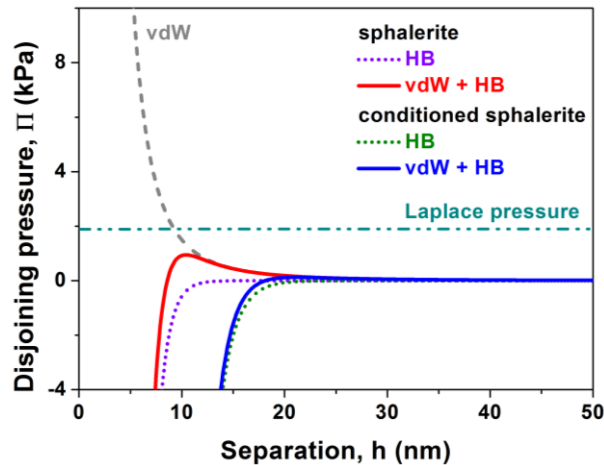
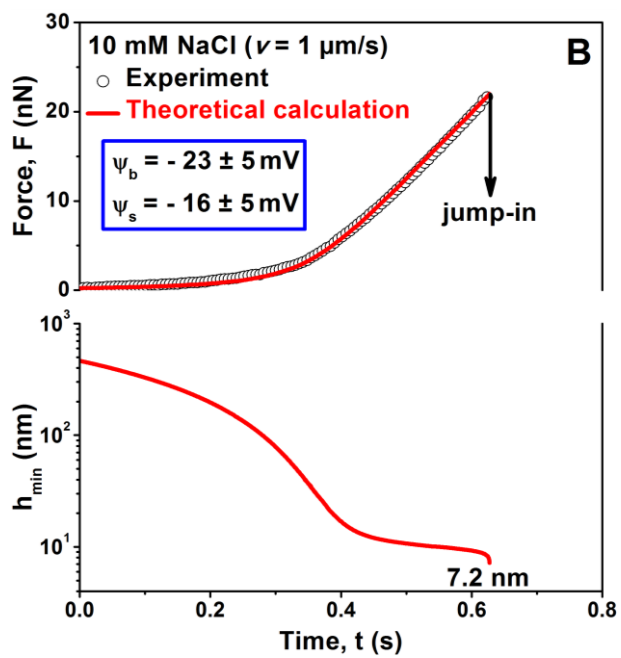
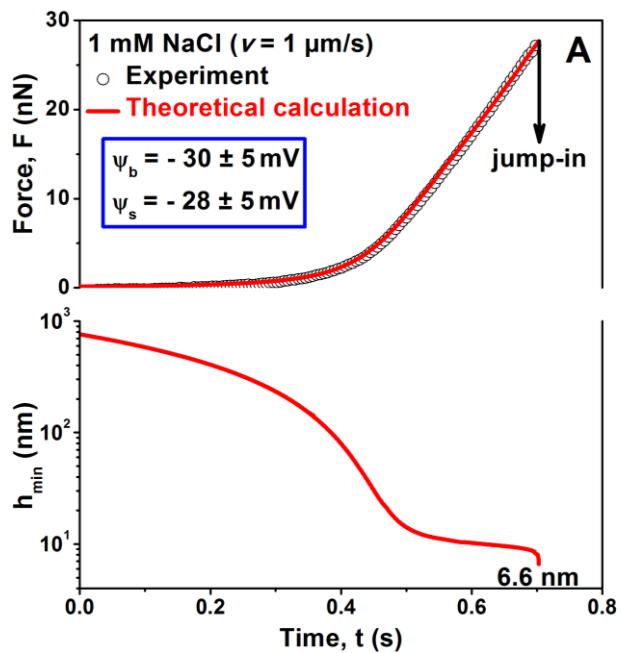


Figure 5.5 The VDW disjoining pressure Π_{VDW} , hydrophobic disjoining pressure Π_{HB} and the overall disjoining pressure Π for the interactions of bubble-water-sphalerite and bubble-water-conditioned sphalerite in 500 mM NaCl solution (air bubble radius ~ 75 μm).

5.3.4 The effects of solution ionic strength

The interaction forces between an air bubble of radius 75 μm and sphalerite surface measured in NaCl solutions of different concentrations (i.e. 1, 10 and 500 mM) and 10 mM CaCl_2 under a low approaching velocity ($v = 1 \mu\text{m/s}$) are shown as open symbols in Figures 5.6A, 5.6B, 5.3A and 5.6C, respectively. The constant $C = 0.08 \text{ N/m}$ and decay length of hydrophobic interaction $D_0 = 1.0 \pm 0.1 \text{ nm}$ was used to fit the interaction forces in Figure 5.6 and determine surface potentials of air bubble and sphalerite surface in the low salt concentration conditions by incorporating the EDL disjoining pressure using Equation 5.4. The theoretically fitted results for the force and minimum water film thickness are shown as solid curves in Figure 5.6, and the fitted surface potential values of the air bubble and sphalerite surface under the different solution conditions are shown in Table 5.1 and Table 5.2 respectively, which agree with the literature values and experimental measurements.⁵⁵⁻⁵⁷ As the NaCl concentration increases from 1, 10 to 500 mM, the critical water film thickness right before the “jump-in” increases from ~ 6.6 , ~ 7.2 to $\sim 8.8 \text{ nm}$ as shown in Figures 5.6A, 5.6B and 5.3A, indicating that the bubble is more readily attached to sphalerite surface with increasing the salt concentration as the repulsive EDL force between negatively charged air bubble and sphalerite surface is weakened.¹⁵ The presence of Ca^{2+} has a more significant effect on suppressing the EDL as compared to Na^+ of the same ionic concentration (e.g. 10 mM), as evident from the slightly higher critical water film thickness shown in Figure 5.6C. Thus, the EDL force also plays an important role in bubble-mineral attachment, particularly at low ionic concentration conditions, which follows the classical DLVO theory.



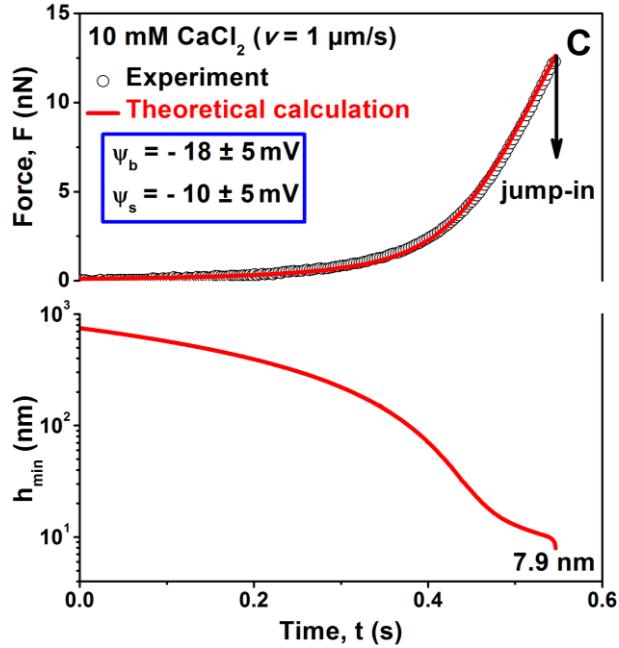


Figure 5.6 The interaction and the corresponding minimum film thickness of the confined water film as a function of time between an air bubble of radius $75 \mu\text{m}$ and a sphalerite surface at low ionic concentration solutions: (A) 1 mM NaCl, (B) 10 mM NaCl and (C) 10 mM CaCl_2 , under a low approaching velocity $v = 1 \mu\text{m/s}$ (open symbols for experiment results, and solid curves for theoretical calculations). The constant C and the decay length D_0 used are 0.08 N/m and $1.0 \pm 0.1 \text{ nm}$, respectively.

Figure 5.7 summarizes the overall disjoining pressure (including contributions from repulsive VDW, repulsive EDL and attractive hydrophobic interactions) for the bubble-water-sphalerite interaction in various solution conditions, which clearly shows weaker and shorter-range repulsive disjoining pressure with increasing the salt concentration (i.e. NaCl, CaCl_2) to facilitate the bubble attachment.

Table 5.1 Comparison of theoretically fitted surface potential values of air bubble and the literature values⁵⁵⁻⁵⁷

Solution condition	Fitted value (mV)	Literature value (mV) ⁵⁵⁻⁵⁷
NaCl (1 mM)	-30 ± 5	-25
		-26
NaCl (10 mM)	-23 ± 5	-18
		-22
		-30
CaCl ₂ (10 mM)	-18 ± 5	-15
		-17

Table 5.2 Comparison of theoretically fitted surface potential values of sphalerite and the measured zeta potential values of sphalerite particles

Solution condition	Fitted value (mV)	Measured value (mV)
NaCl (1 mM)	-28 ± 5	-25.1 ± 1.3
NaCl (10 mM)	-16 ± 5	-12.6 ± 1.1
CaCl ₂ (10 mM)	-10 ± 5	-8.5 ± 0.3

Recycled water of high salinity and seawater have been recently applied for mineral flotation by mineral processing industry due to the shortage of available fresh water sources and restrictions for disposal of used water to the environment. It is important to understand the interaction between air bubble and sphalerite surface in complex aqueous media containing mixed types of salts (e.g. monovalent and divalent

ions). Herein, a saline water solution (viz. a mixture of simulated seawater and process water based on a recipe from a previous report⁵⁸ as shown in Table 5.3) was used to mimic the complex aqueous medium in real mineral industrial process to study its influence on bubble-mineral interaction and attachment.

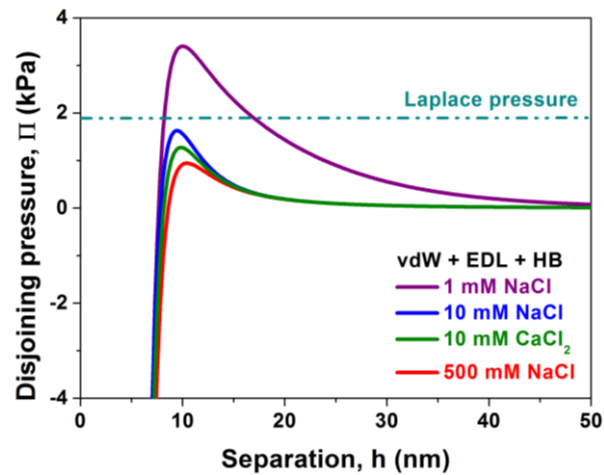


Figure 5.7 The overall disjoining pressure Π for the bubble-water-sphalerite interaction in various solution conditions (air bubble radius $\sim 75 \mu\text{m}$).

The overall ionic strength of the saline water above is close to that of 500 mM NaCl solution, suggesting that the repulsive EDL force is significantly screened and bubble-sphalerite attachment is expected under the same approaching velocity as observed in the 500 mM NaCl solution (Figures 5.3A and 5.3B). Interestingly, Figure 5.8 shows that no bubble attachment was observed in the saline water even at a low approaching velocity $v = 1 \mu\text{m/s}$, which demonstrates that the saline water of mixed types of salts inhibits the bubble-sphalerite attachment and has a more complex influence on bubble-mineral interaction than simple monovalent salt NaCl or divalent salt CaCl_2 . Such anomalous impact of the saline water could not be interpreted by the classical DLVO theory even including the hydrophobic interaction, and it is likely due to the synergistic

influence of the presence of various divalent ions such as Ca^{2+} (7.7 mM), Mg^{2+} (41.1 mM), and SO_4^{2-} (22.5 mM). One possibility is that repulsive hydration interaction prevents bubble attachment on sphalerite surface by overcoming the attractive hydrophobic interaction,^{20, 59} and another possibility is that the formation of CaSO_4 in bulk solution and on mineral surface may affect the interaction between air bubble and sphalerite surface.⁶⁰

Table 5.3 Ion composition of the saline water

Ion composition	Na^+	K^+	Ca^{2+}	Mg^{2+}	Cl^-	SO_4^{2-}
Ionic concentration (mM)	359.6	10.8	7.7	41.1	423.0	22.5
Ionic strength (mM)	539.3					

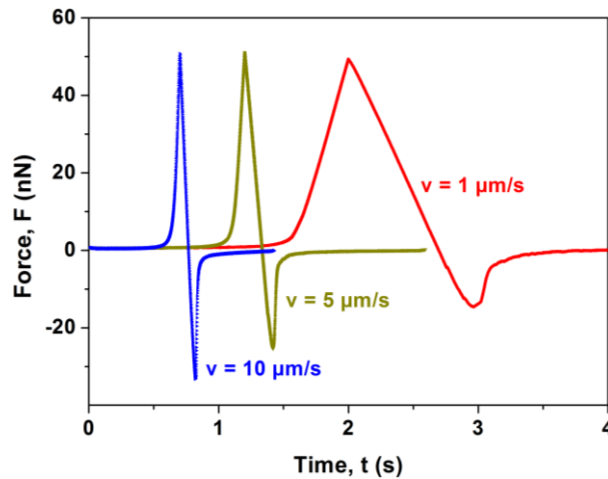


Figure 5.8 The measured interaction forces between an air bubble of radius $75 \mu\text{m}$ and a sphalerite surface under different approaching velocities in saline water (mixture of simulated seawater and process water⁵⁸ as shown in Table 5.3).

It is noted that the ion specificity like the Hofmeister series effect has been shown to affect surface interactions of various systems such as bubble coalescence⁶¹⁻⁶² and hydrophobic polymers⁶³⁻⁶⁴, and ion specificity would also likely play a role in the bubble-mineral interactions, which will be reported in a separate work.

5.4 Conclusions

The interaction forces between an air bubble and sphalerite mineral surfaces were systematically probed, for the first time, using an AFM bubble probe technique under different hydrodynamic conditions, and the effects of conditioning treatment and aqueous solution conditions were investigated. The direct force measurements reveal the critical role of the hydrodynamic force and surface forces in bubble-mineral interaction and attachment. The theoretical calculations based on Reynolds lubrication theory and augmented Young-Laplace equation by including the effect of disjoining pressure show excellent agreement with the AFM experiment results. It was found that hydrophobic disjoining pressure described by $\Pi_{HB} = -\gamma(1 - \cos\theta)e^{-h/D_0}/D_0$ was stronger for the bubble-water-conditioned sphalerite interaction with a larger hydrophobic decay length D_0 , which enables the bubble attachment on conditioned sphalerite (with water contact angle $\theta \sim 85^\circ$) at relatively higher bubble approaching velocities than that of unconditioned sphalerite (with $\theta \sim 35^\circ$). With increasing the ionic concentration of a pure monovalent or divalent salt, EDL force could be compressed which facilitates the bubble-mineral attachment, following the classical DLVO theory by including the effects of hydrophobic interaction. This study provides a useful and versatile research methodology to quantitatively probe the bubble-mineral interaction forces at the nanoscale that could

offer valuable information for the fundamental understanding of the interaction mechanisms between bubbles and minerals in many mineral flotation processes and other related engineering operations.

5.5 Acknowledgement

We gratefully acknowledge the financial support from the Natural Sciences and Engineering Research Council of Canada (NSERC), Canadian Centre for Clean Coal/Carbon and Mineral Processing Technologies (C5MPT), the Canada Foundation for Innovation (CFI) and the Alberta Advanced Education & Technology Small Equipment Grants Program (AET/SEGP).

5.6 References

1. Klassen, V. I.; Mokrousov, V. A., *An Introduction to the Theory of Flotation*; Butterworths, **1963**.
2. Leja, J., *Surface Chemistry of Froth Flotation*; Plenum Press, **1982**.
3. Kelly, E. G.; Spottiswood, D. J., *Introduction to Mineral Processing*; Wiley, **1982**.
4. Rubio, J.; Souza, M.; Smith, R., Overview of Flotation as a Wastewater Treatment Technique. *Miner. Eng.* **2002**, *15*, 139-155.
5. Kemper, M., State-of-the-Art and New Technologies in Flotation Deinking. *Int. J. Miner. Process.* **1999**, *56*, 317-333.
6. Ralston, J.; Fornasiero, D.; Hayes, R., Bubble-Particle Attachment and Detachment in Flotation. *Int. J. Miner. Process.* **1999**, *56*, 133-164.
7. Horn, R. G.; Asadullah, M.; Connor, J. N., Thin Film Drainage: Hydrodynamic and

Disjoining Pressures Determined from Experimental Measurements of the Shape of a Fluid Drop Approaching a Solid Wall. *Langmuir* **2006**, *22*, 2610-2619.

8. Chan, D. Y.; Klaseboer, E.; Manica, R., Film Drainage and Coalescence between Deformable Drops and Bubbles. *Soft Matter* **2011**, *7*, 2235-2264.

9. Albijanic, B.; Ozdemir, O.; Nguyen, A. V.; Bradshaw, D., A Review of Induction and Attachment Times of Wetting Thin Films between Air Bubbles and Particles and Its Relevance in the Separation of Particles by Flotation. *Adv. Colloid Interface Sci.* **2010**, *159*, 1-21.

10. Schulze, H., Hydrodynamics of Bubble-Mineral Particle Collisions. *Miner. Process. Extr. Metall. Rev.* **1989**, *5*, 43-76.

11. Dai, Z.; Fornasiero, D.; Ralston, J., Particle–Bubble Attachment in Mineral Flotation. *J. Colloid Interface Sci.* **1999**, *217*, 70-76.

12. Tian, Y.; Pesika, N.; Zeng, H.; Rosenberg, K.; Zhao, B.; McGuiggan, P.; Autumn, K.; Israelachvili, J., Adhesion and Friction in Gecko Toe Attachment and Detachment. *Proc. Natl. Acad. Sci. U. S. A.* **2006**, *103*, 19320-19325.

13. Zhang, X.; Kumar, A.; Scales, P. J., Effects of Solvency and Interfacial Nanobubbles on Surface Forces and Bubble Attachment at Solid Surfaces. *Langmuir* **2011**, *27*, 2484-2491.

14. Alcantar, N.; Israelachvili, J.; Boles, J., Forces and Ionic Transport between Mica Surfaces: Implications for Pressure Solution. *Geochim. Cosmochim. Acta* **2003**, *67*, 1289-1304.

15. Israelachvili, J. N., *Intermolecular and Surface Forces: Revised Third Edition*; Academic press, **2011**.

16. Israelachvili, J.; Min, Y.; Akbulut, M.; Alig, A.; Carver, G.; Greene, W.; Kristiansen, K.; Meyer, E.; Pesika, N.; Rosenberg, K., Recent Advances in the Surface Forces Apparatus (Sfa) Technique. *Rep. Prog. Phys.* **2010**, *73*, 036601.
17. Zeng, H.; Tian, Y.; Anderson, T. H.; Tirrell, M.; Israelachvili, J. N., New Sfa Techniques for Studying Surface Forces and Thin Film Patterns Induced by Electric Fields. *Langmuir* **2008**, *24*, 1173-1182.
18. Israelachvili, J.; Pashley, R., The Hydrophobic Interaction Is Long Range, Decaying Exponentially with Distance. *Nature* **1982**, *300*, 341-342.
19. Israelachvili, J. N.; Pashley, R. M., Molecular Layering of Water at Surfaces and Origin of Repulsive Hydration Forces. *Nature* **1983**, *306*, 249-250.
20. Israelachvili, J. N.; McGuiggan, P. M., Forces between Surfaces in Liquids. *Science* **1988**, *241*, 795-800.
21. Ducker, W. A.; Senden, T. J.; Pashley, R. M., Direct Measurement of Colloidal Forces Using an Atomic Force Microscope. *Nature* **1991**, *353*, 239-241.
22. Butt, H.-J.; Cappella, B.; Kappl, M., Force Measurements with the Atomic Force Microscope: Technique, Interpretation and Applications. *Surf. Sci. Rep.* **2005**, *59*, 1-152.
23. Yang, D.; Xie, L.; Bobicki, E.; Xu, Z.; Liu, Q.; Zeng, H., Probing Anisotropic Surface Properties and Interaction Forces of Chrysotile Rods by Atomic Force Microscopy and Rheology. *Langmuir* **2014**, *30*, 10809-10817.
24. Gillies, G.; Kappl, M.; Butt, H.-J., Direct Measurements of Particle–Bubble Interactions. *Adv. Colloid Interface Sci.* **2005**, *114*, 165-172.
25. Johnson, D. J.; Miles, N. J.; Hilal, N., Quantification of Particle–Bubble Interactions Using Atomic Force Microscopy: A Review. *Adv. Colloid Interface Sci.* **2006**, *127*, 67-81.

26. Butt, H.-J., A Technique for Measuring the Force between a Colloidal Particle in Water and a Bubble. *J. Colloid Interface Sci.* **1994**, *166*, 109-117.
27. Ducker, W. A.; Xu, Z.; Israelachvili, J. N., Measurements of Hydrophobic and DLVO Forces in Bubble-Surface Interactions in Aqueous Solutions. *Langmuir* **1994**, *10*, 3279-3289.
28. Fielden, M. L.; Hayes, R. A.; Ralston, J., Surface and Capillary Forces Affecting Air Bubble-Particle Interactions in Aqueous Electrolyte. *Langmuir* **1996**, *12*, 3721-3727.
29. Chan, D. Y.; Klaseboer, E.; Manica, R., Theory of Non-Equilibrium Force Measurements Involving Deformable Drops and Bubbles. *Adv. Colloid Interface Sci.* **2011**, *165*, 70-90.
30. Tabor, R. F.; Grieser, F.; Dagastine, R. R.; Chan, D. Y., Measurement and Analysis of Forces in Bubble and Droplet Systems Using Afm. *J. Colloid Interface Sci.* **2012**, *371*, 1-14.
31. Dagastine, R. R.; Manica, R.; Carnie, S. L.; Chan, D.; Stevens, G. W.; Grieser, F., Dynamic Forces between Two Deformable Oil Droplets in Water. *Science* **2006**, *313*, 210-213.
32. Attard, P.; Miklavcic, S. J., Effective Spring Constant of Bubbles and Droplets. *Langmuir* **2001**, *17*, 8217-8223.
33. Vakarelski, I. U.; Lee, J.; Dagastine, R. R.; Chan, D. Y.; Stevens, G. W.; Grieser, F., Bubble Colloidal Afm Probes Formed from Ultrasonically Generated Bubbles. *Langmuir* **2008**, *24*, 603-605.
34. Vakarelski, I. U.; Manica, R.; Tang, X.; O'Shea, S. J.; Stevens, G. W.; Grieser, F.; Dagastine, R. R.; Chan, D. Y., Dynamic Interactions between Microbubbles in Water.

Proc. Natl. Acad. Sci. U. S. A. **2010**, *107*, 11177-11182.

35. Tabor, R. F.; Chan, D. Y.; Grieser, F.; Dagastine, R. R., Anomalous Stability of Carbon Dioxide in Ph - Controlled Bubble Coalescence. *Angew. Chem., Int. Ed.* **2011**, *123*, 3516-3518.

36. Manor, O.; Vakarelski, I. U.; Tang, X.; O'Shea, S. J.; Stevens, G. W.; Grieser, F.; Dagastine, R. R.; Chan, D. Y., Hydrodynamic Boundary Conditions and Dynamic Forces between Bubbles and Surfaces. *Phys. Rev. Lett.* **2008**, *101*, 024501.

37. Tabor, R. F.; Manica, R.; Chan, D. Y.; Grieser, F.; Dagastine, R. R., Repulsive Van Der Waals Forces in Soft Matter: Why Bubbles Do Not Stick to Walls. *Phys. Rev. Lett.* **2011**, *106*, 064501.

38. Manor, O.; Vakarelski, I. U.; Stevens, G. W.; Grieser, F.; Dagastine, R. R.; Chan, D. Y., Dynamic Forces between Bubbles and Surfaces and Hydrodynamic Boundary Conditions. *Langmuir* **2008**, *24*, 11533-11543.

39. Shi, C.; Chan, D. Y.; Liu, Q.; Zeng, H., Probing Hydrophobic Interaction between Air Bubble and Partially Hydrophobic Surfaces Using Atomic Force Microscopy. *J. Phys. Chem. C* **2014**, *118*, 25000-25008.

40. Shi, C.; Cui, X.; Xie, L.; Liu, Q.; Chan, D. Y.; Israelachvili, J. N.; Zeng, H., Measuring Forces and Spatiotemporal Evolution of Thin Water Films between an Air Bubble and Solid Surfaces of Different Hydrophobicity. *ACS nano* **2014**.

41. Duke, C.; Wang, Y., Surface Structure and Bonding of the Cleavage Faces of Tetrahedrally Coordinated II-VI Compounds. *J. Vac. Sci. Technol., B* **1988**, *6*, 1440-1443.

42. Wang, J.; Liu, Q.; Zeng, H., Understanding Copper Activation and Xanthate Adsorption on Sphalerite by ToF-SIMS, XPS and in-Situ SEM. *J. Phys. Chem. C* **2013**,

117, 20089-20097.

43. Teng, F.; Liu, Q.; Zeng, H., In Situ Kinetic Study of Zinc Sulfide Activation Using a Quartz Crystal Microbalance with Dissipation (Qcm-D). *J. Colloid Interface Sci.* **2012**, *368*, 512-520.

44. Chandra, A.; Gerson, A., A Review of the Fundamental Studies of the Copper Activation Mechanisms for Selective Flotation of the Sulfide Minerals, Sphalerite and Pyrite. *Adv. Colloid Interface Sci.* **2009**, *145*, 97-110.

45. Hutter, J. L.; Bechhoefer, J., Calibration of Atomic-Force Microscope Tips. *Rev. Sci. Instrum.* **1993**, *64*, 1868-1873.

46. Nguyen, A., Historical Note on the Stefan–Reynolds Equations. *J. Colloid Interface Sci.* **2000**, *231*, 195.

47. Nguyen, A.; Schulze, H. J., *Colloidal Science of Flotation*; CRC Press, **2003**.

48. Toikka, G.; Hayes, R. A.; Ralston, J., Surface Forces between Spherical Zns Particles in Aqueous Electrolyte. *Langmuir* **1996**, *12*, 3783-3788.

49. Yaminsky, V. V.; Ohnishi, S.; Vogler, E. A.; Horn, R. G., Stability of Aqueous Films between Bubbles. Part 1. The Effect of Speed on Bubble Coalescence in Purified Water and Simple Electrolyte Solutions. *Langmuir* **2010**, *26*, 8061-8074.

50. Christenson, H. K.; Claesson, P. M., Cavitation and the Interaction between Macroscopic Hydrophobic Surfaces. *Science* **1988**, *239*, 390-392.

51. Tsao, Y.-H.; Evans, D. F.; Wennerstrom, H., Long-Range Attractive Force between Hydrophobic Surfaces Observed by Atomic Force Microscopy. *Science* **1993**, *262*, 547-550.

52. Mielczarski, J.; Mielczarski, E.; Cases, J., Interaction of Amyl Xanthate with

Chalcopyrite, Tetrahedrite, and Tennantite at Controlled Potentials. Simulation and Spectroelectrochemical Results for Two-Component Adsorption Layers. *Langmuir* **1996**, *12*, 6521-6529.

53. Mielczarski, J. A.; Mielczarski, E.; Zachwieja, J.; Cases, J., In Situ and Ex Situ Infrared Studies of Nature and Structure of Thiol Monolayers Adsorbed on Cuprous Sulfide at Controlled Potential. *Langmuir* **1995**, *11*, 2787-2799.

54. Somasundaran, P., *Encyclopedia of Surface and Colloid Science*; CRC Press, **2006**.

55. Yang, C.; Dabros, T.; Li, D.; Czarnecki, J.; Masliyah, J. H., Measurement of the Zeta Potential of Gas Bubbles in Aqueous Solutions by Microelectrophoresis Method. *J. Colloid Interface Sci.* **2001**, *243*, 128-135.

56. Cho, S.-H.; Kim, J.-Y.; Chun, J.-H.; Kim, J.-D., Ultrasonic Formation of Nanobubbles and Their Zeta-Potentials in Aqueous Electrolyte and Surfactant Solutions. *Colloids Surf., A* **2005**, *269*, 28-34.

57. Han, M.; Kim, M.; Shin, M., Generation of a Positively Charged Bubble and Its Possible Mechanism of Formation. *J. Water Supply Res. Technol. AQUA* **2006**, *55*, 471-478.

58. Ji, Y.; Lu, Q.; Liu, Q.; Zeng, H., Effect of Solution Salinity on Settling of Mineral Tailings by Polymer Flocculants. *Colloids Surf., A* **2013**, *430*, 29-38.

59. Pashley, R.; Israelachvili, J., Dlvo and Hydration Forces between Mica Surfaces in Mg^{2+} , Ca^{2+} , Sr^{2+} , and Ba^{2+} Chloride Solutions. *J. Colloid Interface Sci.* **1984**, *97*, 446-455.

60. Teng, F.; Zeng, H.; Liu, Q., Understanding the Deposition and Surface Interactions of Gypsum. *J. Phys. Chem. C* **2011**, *115*, 17485-17494.

61. Craig, V.; Ninham, B.; Pashley, R., Effect of Electrolytes on Bubble Coalescence.

Nature **1993**, 364, 317-319.

62. Craig, V. S.; Ninham, B. W.; Pashley, R. M., The Effect of Electrolytes on Bubble Coalescence in Water. *The Journal of Physical Chemistry* **1993**, 97, 10192-10197.

63. Faghihnejad, A.; Zeng, H., Hydrophobic Interactions between Polymer Surfaces: Using Polystyrene as a Model System. *Soft Matter* **2012**, 8, 2746-2759.

64. Faghihnejad, A.; Zeng, H., Interaction Mechanism between Hydrophobic and Hydrophilic Surfaces: Using Polystyrene and Mica as a Model System. *Langmuir* **2013**, 29, 12443-12451.

Chapter 6 Interaction Mechanisms between Air Bubble and Molybdenite Surface: Impact of Solution Salinity and Polymer Adsorption

6.1 Introduction

Molybdenite, the mineral form of molybdenum disulfide (MoS_2), is the most important source of molybdenum. Due to the excellent electronic and optical properties, MoS_2 has attracted tremendous research interest in a wide range of engineering applications,¹⁻⁴ such as electronics,⁵⁻⁶ catalysis,⁷⁻⁸ energy storage,⁹⁻¹⁰ and clinical devices.¹¹⁻¹² The consecutive MoS_2 layers held by weak van der Waals (VDW) interaction can be readily exfoliated to expose the atomic layer with a low coefficient of friction, making it an excellent candidate as solid lubricant in tribological applications.¹³ The surface characteristics of MoS_2 such as wettability and surface interactions, which in certain cases can significantly impact its adhesion and friction behaviors, play important roles in its applications in electronic and optical devices, tribology and froth flotation.¹⁴⁻¹⁷ In flotation process, MoS_2 minerals can be selectively separated from other mineral particles based on their attachment propensities to air bubbles.¹⁸⁻²⁰ Understanding the effect of surface properties on the bubble-molybdenite interactions is of both fundamental and practical importance. Generally, the drainage process of the intervening water film during the bubble-solid attachment is governed by the combined influences of hydrodynamic pressure and disjoining pressure contributed from VDW, electrical double layer (EDL), hydrophobic, and steric interactions.²¹⁻²⁴ Strong hydrophobic attraction can

result in rupture of confined water film and bubble-mineral attachment, while EDL and steric repulsion can inhibit the drainage process and prevent bubble attachment.²¹⁻²³

Molybdenite exhibits inherently hydrophobic nature on its freshly exfoliated basal plane, and water-soluble polymeric depressants used in the processing of molybdenum ores could adsorb on molybdenite surface and reduce its floatability due to the increased surface hydrophilicity.²⁵⁻²⁷ Over the past few decades, considerable progress has been made to unravel the polymer adsorption mechanism and bubble collision interactions on naturally hydrophobic minerals (e.g. molybdenite, talc and graphite).²⁸⁻³³ The single bubble-surface collision study by Beattie and co-workers³³ showed that the polymer depressants adsorbed on naturally hydrophobic minerals resulted in longer time of wetting film drainage and slower rate of dewetting process. In addition, a lower degree of carboxyl group substitution within carboxymethyl cellulose (CMC) and higher salt concentration led to a thicker adsorbed polymer layer and an increased polymer coverage on molybdenite surface, which had a profound influence on slowing down wetting film rupture and three-phase contact line (TPCL) movement.³⁴ To date, no study has been reported on quantitative measurements of interaction forces between air bubbles and naturally hydrophobic minerals, especially in the presence of adsorbed polymer depressant, probably due to the practical difficulties in precise manipulation of air bubble and interpretation of measured forces.

Recently, the bubble probe AFM technique has been developed and applied to quantitatively measure the surface interactions involving deformable air bubbles, such as bubble-bubble interaction and bubble-solid interaction.^{20, 23, 35-45} The combinatory effects of surface forces, hydrodynamic interaction and bubble deformation could be

successfully described by a theoretical model based on Reynolds lubrication theory and augmented Young-Laplace equation.^{20, 23, 35-45} Therefore, the surface forces (e.g. VDW, EDL and hydrophobic interactions) involving deformable objects (e.g. bubbles) can be precisely quantified with sub-nN resolution and the drainage process of confined liquid film can be synchronously determined with nm resolution, which has been verified by our recent experimental measurements using the bubble probe AFM combined with reflection interference contrast microscopy (RICM).³⁶

In this work, the bubble probe AFM technique was employed to directly measure the interaction forces between an air bubble and a molybdenite surface in aqueous solutions, and the results were analyzed using the theoretical model based on Reynolds lubrication theory and augmented Young-Laplace equation. The effects of adsorbed polymer (i.e. guar gum) on the morphology of molybdenite surface and the bubble-molybdenite interaction were also investigated. This work provides useful information regarding the interaction mechanisms between air bubbles and naturally hydrophobic minerals before/after polymer adsorption at the nanoscale, with implications for the design and performance evaluation of novel polymers to depress the bubble attachment efficiency for many flotation processes.

6.2 Materials and methods

6.2.1 Materials

Sodium chloride (NaCl, ACS reagent grade) and guar gum with a molecular weight of $\sim 2.5 \times 10^5$ g/mol were purchased from Fisher Scientific and used as received without further purification. Hydrochloric acid (HCl, ACS reagent grade) and sodium

hydroxide (NaOH, ACS reagent grade) purchased from Fisher Scientific were used to adjust solution pH. In this work, all aqueous solutions were prepared using Milli-Q water (Millipore deionized, 18.2 M Ω -cm resistivity), and the solution pH was fixed at 9.

6.2.2 Preparation of molybdenite surface

The natural cleavage surface of molybdenite (Ward's Science, Rochester, NY) was obtained by peeling off the top layers using a sticky tape. Polymer stock solutions (500 ppm) were prepared by dissolving a desired amount of guar gum in Milli-Q water under stirring overnight to ensure complete hydration. Solutions of desired concentration (i.e. 1, 5, 10 and 50 ppm) were prepared by diluting the stock solution in Milli-Q water and fixing solution pH at 9. Thereafter, freshly exfoliated molybdenite basal plane was conditioned in the desired polymer solutions for 30 min, rinsed by Milli-Q water, and then dried using high-purity nitrogen prior to measurements. Herein, molybdenite conditioned in 1, 5, 10 and 50 ppm guar gum solution were used to investigate the effect of polymer concentration on the adsorption of polymer on molybdenite surface as well as the bubble-molybdenite interaction.

6.2.3 Surface characterization

A contact angle goniometer (ramé-hart instrument Co., NJ, USA) was used to measure the static water contact angle on mineral surfaces using a sessile drop method. For the same type of sample, at least two different surfaces and three different positions on each surface were tested, and the average water contact angle was reported. The height

and phase images of mineral surfaces were obtained using the tapping mode in water with a MFP-3D AFM system (Asylum Research, Santa Barbara, CA, USA).

6.2.4 Force measurements

The interaction between an air bubble and mineral surface was measured using bubble probe AFM technique. By carefully purging air through a custom-made ultra-sharp glass pipette into aqueous solution, air bubbles were generated and immobilized on the glass disk of a fluid cell. The bubble probe was then prepared by picking up an air bubble of suitable size (typically 60-90 μm radius) with a custom-made rectangular silicon cantilever (400 \times 70 \times 2 μm). The glass disk and AFM cantilever were hydrophobized in advance following an established method.³⁶ Briefly, the glass disk of the fluid cell was mildly hydrophobized by immersing in 10 mM octadecyltrichlorosilane (OTS) in toluene for \sim 10 s, followed by thorough rinsing with toluene, ethanol and water, to give a water contact angle of 40 $^\circ$ -60 $^\circ$ for bubble immobilization, and AFM cantilevers with a circular gold patch (diameter 65 μm , thickness 30 nm) were strongly hydrophobized by immersing in 10 mM dodecanethiol in absolute ethanol overnight to provide higher hydrophobicity than the glass disk for bubble anchoring. The spring constant of the cantilever was determined to be 0.3-0.4 N/m using the Hutter and Bechhoefer method.⁴⁶ The cantilever-anchored air bubble was positioned over mineral surface and then driven to approach the surface until a fixed deflection of the cantilever was reached or bubble attachment occurred. The force measurements were conducted at a fixed driving velocity of 1 $\mu\text{m/s}$ at pH 9 with minimized hydrodynamic effect. A schematic of typical experiment setup for force measurements using the bubble probe

AFM is shown in Figure 6.1. The movement of the cantilever (anchored with air bubble) and the corresponding interaction forces were recorded as a function of time by AFM software.

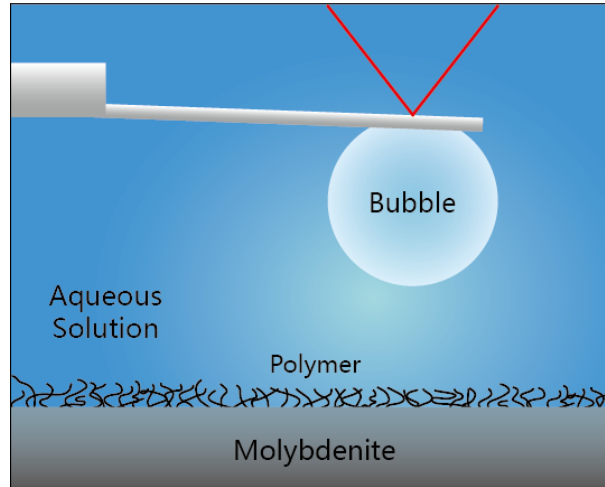


Figure 6.1 Schematic of force measurements between air bubble and molybdenite surface in aqueous solution using the bubble probe AFM.

6.2.5 Theoretical model

A theoretical model based on Reynolds lubrication theory coupled with augmented Young-Laplace equation was applied to analyze the measured forces between air bubbles and mineral surfaces.

The drainage process of thin water film confined between air bubble and mineral surface is described by the Reynolds lubrication theory:^{20, 23, 35-44}

$$\frac{\partial h}{\partial t} = \frac{1}{12\mu r} \frac{\partial}{\partial r} \left(rh^3 \frac{\partial p}{\partial r} \right) \quad (6.1)$$

where μ is the dynamic viscosity of water, $h(r, t)$ is the thickness of confined thin liquid film, and $p(r, t)$ is the excess hydrodynamic pressure in the liquid film relative to the bulk

solution. Immobile boundary condition was assumed at air/water and water/mineral interfaces, which is consistent with recent reports.^{20, 23, 35-44}

The deformation of the bubble under combined influence of hydrodynamic and disjoining pressure is described by the augmented Young-Laplace equation.^{20, 23, 35-44}

$$\frac{\gamma}{r} \frac{\partial}{\partial r} \left(r \frac{\partial h}{\partial r} \right) = \frac{2\gamma}{R} - p - \Pi \quad (6.2)$$

where γ is the water/air interfacial tension, R is the radius of air bubble, and $\Pi(r, t)$ is the overall disjoining pressure due to surface forces such as VDW, EDL, and hydrophobic interactions.

The contributions of VDW, EDL and hydrophobic interactions to the disjoining pressure Π_{VDW} , Π_{EDL} and Π_{HB} can be given by Equations 6.3, 6.4 and 6.5, respectively, where A_{A-W-M} is the Hamaker constant for air-water-molybdenite, κ^{-1} is the Debye length, ψ_{Air} and ψ_{Moly} are the surface potential of air bubble and molybdenite surface, respectively, D_0 is the decay length of hydrophobic interaction and C is a constant (N/m).^{20, 47}

$$\Pi_{VDW} = -\frac{A_{A-W-M}}{6\pi h^3} \quad (6.3)$$

$$\Pi_{EDL} = \frac{2\varepsilon_0 \varepsilon \kappa^2 \left[(e^{+\kappa h} + e^{-\kappa h}) \psi_{Air} \psi_{Moly} - (\psi_{Air}^2 + \psi_{Moly}^2) \right]}{(e^{+\kappa h} - e^{-\kappa h})^2} \quad (6.4)$$

$$\Pi_{HB} = -\frac{C}{2\pi D_0} e^{-h/D_0} \quad (6.5)$$

The overall interaction force between an air bubble and a mineral surface $F(t)$ is theoretically calculated by integrating $p(r, t)$ and $\Pi(r, t)$ based on Derjaguin approximation as shown in Equation 6.6.^{20, 23, 35-44}

$$F(t) = 2\pi \int_0^{\infty} (p(r,t) + \Pi(h(r,t)))rdr \quad (6.6)$$

6.2.6 Microflotation tests

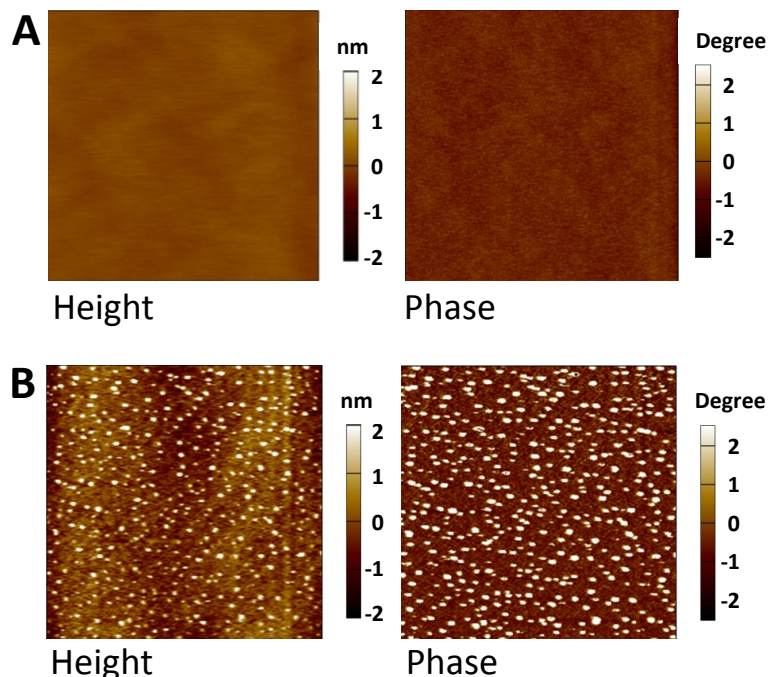
The single mineral microflotation tests were carried out in a custom-made Hallimond tube. In each microflotation test, 1.5 g molybdenite mineral particles with the size of 74 μm to 150 μm were added into 150 mL NaCl solution (100 mM) with the addition of different concentrations of polymer (i.e. guar gum). The obtained suspension was conditioned for 5 minutes, during which the solution pH was adjusted to 9. Thereafter, the frother 4-Methyl-2-pentanol (MIBC) was added into the suspension and transferred to the microflotation tube for flotation using high purity compressed air with a flow rate of 20 cm^3/min . After 8 minutes, the floated mineral particles were collected to analyze the recovery of molybdenite and each test was repeated for at least three times to obtain the average recovery.

6.3 Results and discussion

6.3.1. Surface morphology

The topographic AFM images of molybdenite surfaces conditioned at different polymer concentrations are shown in Figure 6.2. Molybdenite can be readily exfoliated along the VDW gap to generate a molecularly smooth basal plane, which shows a root-mean-square (rms) roughness of ~ 0.2 nm in Figure 6.2A. After polymer adsorption, obvious variations in surface morphology of molybdenite could be observed in the height images in Figures 6.2B, 6.2C, 6.2D and 6.2E. Molybdenite conditioned at very low polymer concentration (~ 1 ppm) in Figure 6.2B exhibited randomly and sparsely

distributed “particles” or aggregates with height up to ~ 3 nm and average diameter of ~ 150 nm. The apparent phase difference between the formed aggregates (bright spots in Figure 6.2B) and surrounding areas indicates that these aggregates were polymers adsorbed on molybdenite surface while the surrounding areas were not covered with polymer. The polymer-covered domains only accounted for $\sim 5.6\%$ of molybdenite surface area. After conditioned in 5 ppm polymer solution, both the height image and phase image in Figure 6.2C show that an interconnected network structure formed by the adsorbed polymers, covering $\sim 44.5\%$ of the molybdenite surface. As shown in Figure 6.2D, with polymer concentration increasing to 10 ppm, molybdenite was covered with a relatively compact and smooth polymer film, and the homogeneous phase distribution suggested almost 100% full polymer coverage. In Figure 6.2E, the continuous increase of polymer concentration to 50 ppm resulted in a more compact and smooth polymer film that fully covered the molybdenite surface. It is evident that the polymer concentration significantly affects the adsorption of polymer on molybdenite surface.



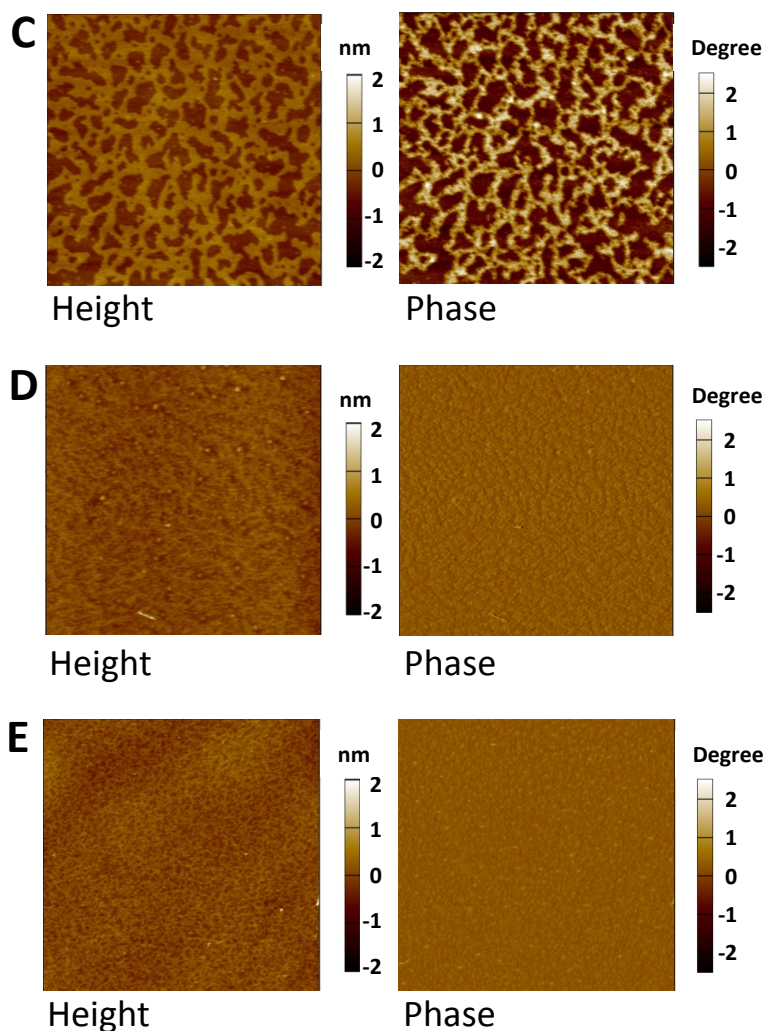


Figure 6.2 AFM height (Left) and phase (Right) images ($5 \times 5 \mu\text{m}^2$) of molybdenite surface conditioned at different polymer concentrations: (A) 0 ppm, (B) 1 ppm, (C) 5 ppm, (D) 10 ppm, and (E) 50 ppm at pH 9.

Molybdenite was also conditioned at very low polymer concentration (~ 1 ppm) with the addition of different concentrations of NaCl to investigate the impact of salt on the polymer adsorption. Figures 6.3A and 6.3B show the AFM height images of molybdenite conditioned in 1 ppm polymer solution with the addition of 10 mM and 100 mM NaCl, respectively. Polymer aggregates are visible on the molybdenite surface with

height up to 3 nm and average diameter of ~ 150 nm, similar to the polymer patterns adsorbed on molybdenite surface conditioned without NaCl addition (Figure 6.2B). It is evident from AFM imaging that adsorbed polymer aggregation patterns on molybdenite become more densely distributed with increasing the NaCl concentration from 0 to 10 mM and further to 100 mM in the polymer solution. From the AFM images, the polymer coverage on molybdenite surface can be determined to be $\sim 11.7\%$ with 10 mM NaCl addition (Figure 6.3A) and $\sim 23.8\%$ with 100 mM NaCl addition (Figure 6.3B), much higher than $\sim 5.6\%$ without NaCl addition (Figure 6.2B). The enhanced adsorption of polymer (i.e. guar gum) on molybdenite was attributed to the suppressed electrical double layer repulsion with increased salinity between negatively charged molybdenite surface and slightly negatively charged polymer at pH 9.⁴⁸⁻⁵¹ The zeta potential values of guar gum and molybdenite have been summarized in Figure 6.4.⁴⁸⁻⁵¹

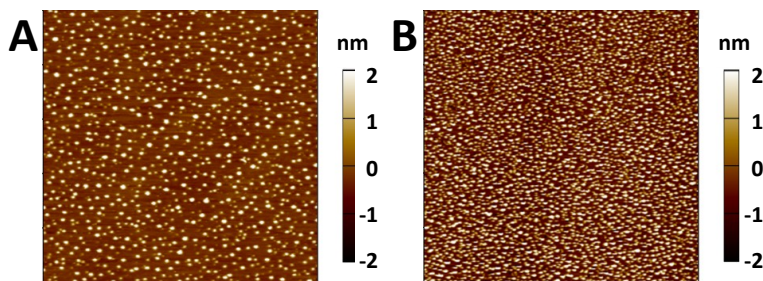


Figure 6.3 AFM height images ($5 \times 5 \mu\text{m}^2$) of molybdenite surface conditioned in 1 ppm polymer solution with the addition of (A) 10 mM and (B) 100 mM NaCl at pH 9.

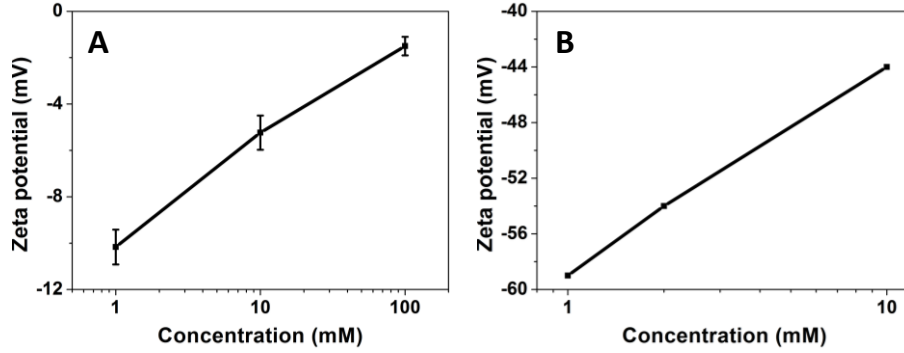


Figure 6.4 Zeta potential of (A) guar gum (measured values) and (B) molybdenite (literature values) at different salt concentrations at pH 9.⁴⁸⁻⁵¹

6.3.2. Surface wettability

Figure 6.5 shows the average water contact angle of molybdenite surface conditioned at different polymer concentrations. The freshly exfoliated molybdenite basal plane exhibits inherently hydrophobic nature with the measured water contact angle of 75°, which slightly decreased to 73° after conditioned in 1 ppm polymer (i.e. guar gum) solution. With polymer concentration increasing to 5 ppm and 10 ppm, the water contact angle significantly decreased to 65° and 56°, respectively. Further increasing the polymer concentration to 50 ppm could only slightly reduce the water contact angle to 55°, indicating that 10 ppm is very close to the critical polymer concentration for a full polymer coverage on molybdenite surface. The Cassie-Baxter model, a generally accepted model for correlating the contact angle with surface area fraction, could be applied to predict the polymer coverage ϕ on molybdenite surface using Equation 6.7,⁴⁷

$$\cos \theta = \phi \cos \theta_{Moly-poly} + (1 - \phi) \cos \theta_{Moly} \quad (6.7)$$

where θ_{Moly} and $\theta_{Moly-poly}$ correspond to the water contact angle on pure molybdenite (~75°) and molybdenite with full polymer coverage (~55°), respectively. Based on Equation 6.7,

the polymer coverage of molybdenite after conditioning in 1 ppm ($\theta = 73^\circ$) and 5 ppm ($\theta = 65^\circ$) polymer solution was calculated to be $\sim 10.3\%$ and $\sim 51.6\%$, respectively. It is worth noting that the contact angle measurements have provided the information on polymer coverage based on a statistical average of a typical area of square millimeters, which is comparable to the polymer coverage results obtained from AFM topographic imaging at the nanoscale.

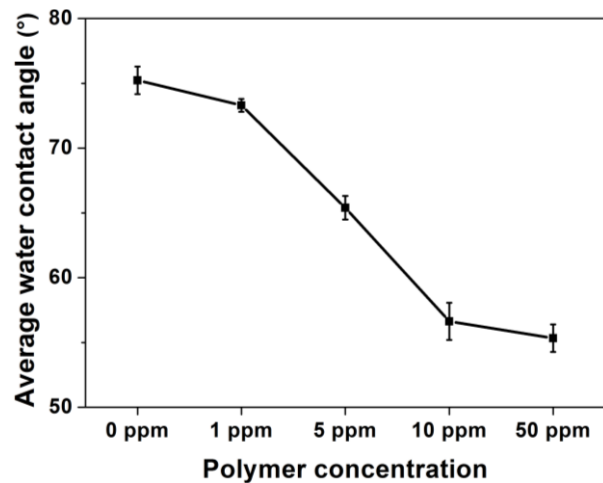


Figure 6.5 Water contact angle of molybdenite surface conditioned at different polymer concentrations.

6.3.3 Bubble-molybdenite interaction

Figure 6.6 shows the interaction force profiles measured between air bubble and molybdenite surface in NaCl solutions of different concentrations (i.e. 100, 10 and 1 mM) at an approaching velocity $v = 1 \mu\text{m/s}$. The measured force profile (open symbols) in 100 mM NaCl (Figure 6.6A) shows a sudden “jump-in” behavior during approach, indicating bubble attachment as also confirmed by an optical microscope. While no “jump-in” behavior could be observed during the approach-retraction cycle at lower NaCl

concentrations such as 10 mM (Figure 6.6B) and 1 mM (Figure 6.6C). It is clear that the salt concentration plays a critical role in the “jump-in” behavior or bubble attachment.

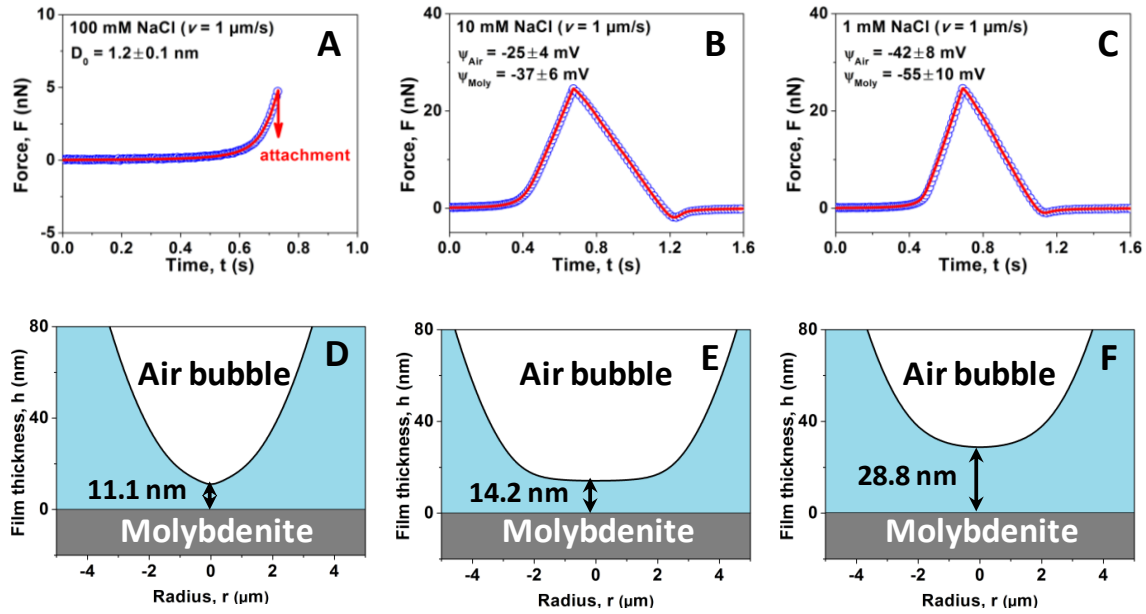


Figure 6.6 Interaction forces (A-C) and calculated thin film profile at maximum force load (D-F) between air bubble and molybdenite surface in NaCl solutions of different concentrations: 100 mM (A and D), 10 mM (B and E) and 1 mM (C and F) at an approaching velocity $v = 1 \mu\text{m/s}$ at pH 9 (open symbols are experiment results and red curves are theoretical calculations).

In Figure 6.6A, bubble attachment was observed during approach when the measured force reached just $\sim 4.8 \text{ nN}$. For the air-water-molybdenite system, the Hamaker constant between air and molybdenite in water is calculated to be $-2.68 \times 10^{-20} \text{ J}$, and thus the VDW interaction is repulsive at any separation.^{47, 55-56} In 100 mM NaCl, the Debye length is calculated to be 0.96 nm and the EDL interaction is significantly screened. Thus, the observed bubble attachment was induced by the attractive hydrophobic interaction. By fitting the measured forces (open symbols) with the theoretical model based on the

Reynolds lubrication equation and augmented Young-Laplace equation by including the influence of disjoining pressure due to hydrophobic interaction (red curve), the decay length of hydrophobic interaction was determined to be $D_0 = 1.2 \pm 0.1$ nm. The calculated profile of thin water film confined between air bubble and molybdenite surface at the maximum force load in 100 mM NaCl is illustrated in Figure 6.6D. The critical central separation just before bubble attachment was calculated to be 11.1 nm, where the central portion of bubble surface formed a pimple due to the overall attraction that exceeded the Laplace pressure inside the bubble.

With NaCl concentration decreasing to 10 and 1 mM, no bubble attachment was observed during the approach-retraction cycle even under a maximum force load of 25 nN as shown in Figures 6.6B and 6.6C. At lower NaCl concentrations, the repulsive EDL interaction between negatively charged air bubble and molybdenite surface could not be neglected. When the cantilever-anchored bubble approached molybdenite surface, the EDL interaction resulted in a strong repulsion that prevented the bubble from attaching to the mineral surface. During retraction of the cantilever, the repulsion gradually decreased and a small attraction was detected due to the hydrodynamic suction effect.⁵⁷⁻⁵⁸

By fitting the measured forces (open symbols) with the theoretical model (red curve), the surface potentials of air bubble and molybdenite surface in 10 and 1 mM NaCl are determined and summarized in Table 6.1, which coincide with the literature values.^{48-50, 52-54} The calculated profile of confined thin water film in 10 mM NaCl (Figure 6.6E) and 1 mM NaCl (Figure 6.6F) shows that the central portion of bubble surface was flattened as the disjoining pressure (due to EDL repulsion) balanced the Laplace pressure inside the bubbles. As NaCl concentration decreased from 10 mM to 1 mM, the central

separation between air bubble and molybdenite surface increased significantly from 14.2 nm to 28.8 nm, indicating that the enhanced EDL repulsion at lower salinity can inhibit the drainage of the confined water film and prevent the bubble attachment to molybdenite surface.

Table 6.1 Comparison of theoretically fitted surface potentials and literature values of air bubble and molybdenite in different solution conditions⁵³⁻⁵⁷

NaCl solution	Air bubble		Molybdenite	
	Fitted (mV)	Literature (mV)	Fitted (mV)	Literature (mV)
1 mM, pH 9	-42 ± 8	-38 -47	-55 ± 10	-54
10 mM, pH 9	-25 ± 4	-22 -23	-37 ± 6	-34

Figure 6.7 shows the calculated disjoining pressure profiles between air bubble and molybdenite surface in NaCl solutions of different concentrations. The disjoining pressure profile in 100 mM NaCl (Figure 6.7A) indicates the hydrophobic attraction is the driving interaction for the bubble attachment on molybdenite surface. At lower NaCl concentrations such as 10 mM (Figure 6.7B) and 1 mM (Figure 6.7C), the EDL repulsion becomes the dominant interaction and the hydrophobic attraction was too weak to trigger the bubble-molybdenite attachment.

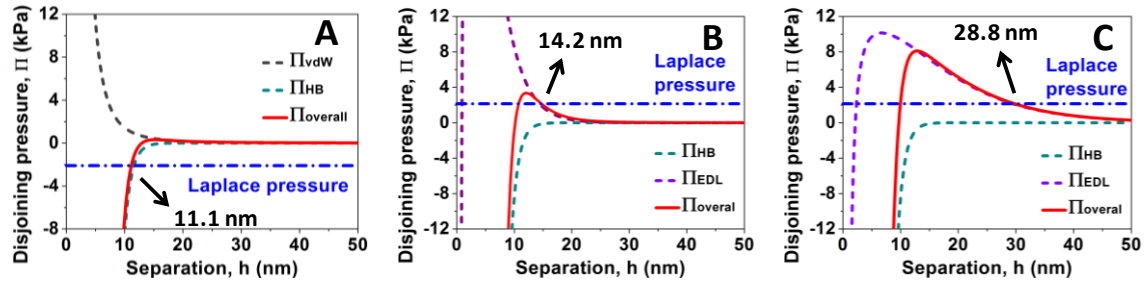


Figure 6.7 Calculated disjoining pressure profiles between air bubble and molybdenite surface in NaCl solutions of different concentrations: (A) 100 mM, (B) 10 mM and (C) 1 mM.

6.3.4 Effect of polymer adsorption on the interaction

The interaction forces between air bubble and molybdenite surfaces conditioned in 1 ppm and 5 ppm polymer solutions were measured in 100 mM NaCl at an approaching velocity $v = 1 \mu\text{m/s}$, as shown in Figure 6.8. Figure 6.8A shows bubble attachment on molybdenite surface conditioned in 1 ppm polymer solution during approach after overcoming a repulsive force of $\sim 11.9 \text{ nN}$, which is larger than the critical force of $\sim 4.8 \text{ nN}$ for the pure molybdenite case (Figure 6.6A), indicating that it becomes more difficult for the bubble to attach to the mineral surface after polymer adsorption. Since the adsorbed polymer layer is very thin, the effect of adsorbed polymer on VDW interaction can be neglected at separation $D > 3 \text{ nm}$ and the VDW interaction can be taken the same as that for the bubble-water-molybdenite system.⁴⁷ The decay length of hydrophobic interaction was determined to be $D_0 = 0.9 \pm 0.1 \text{ nm}$ by fitting the measured forces with the theoretical model including the effect of hydrophobic interaction. The decreased decay length of hydrophobic interaction as compared to the pure molybdenite

case suggested weakened hydrophobic attraction for molybdenite after polymer adsorption.

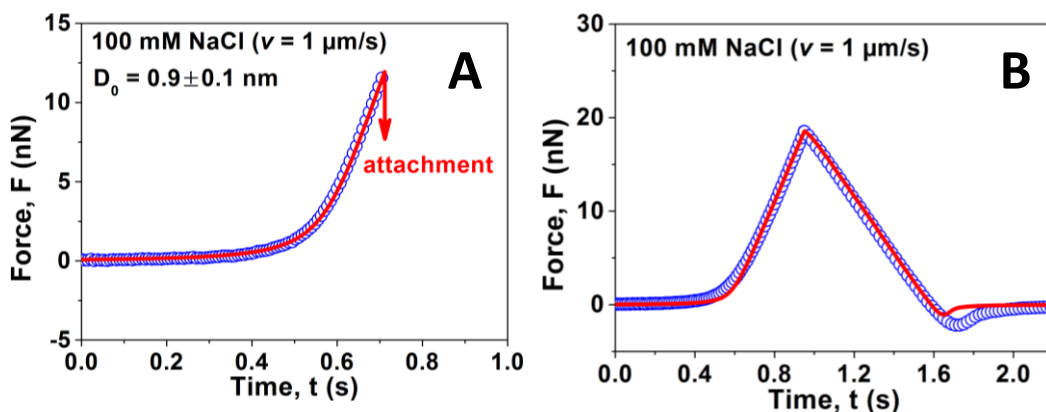


Figure 6.8 Interaction forces between air bubble and molybdenite surface conditioned in (A) 1 ppm polymer solution and (B) 5 ppm polymer solution in 100 mM NaCl at $v = 1 \mu\text{m/s}$ at pH 9 (open symbols for experiment results and solid curves for theoretical calculations).

With increasing the polymer concentration to 5 ppm, no bubble attachment could be observed (Figure 6.8B). Thus, conditioning the molybdenite surface in 5 ppm polymer could effectively inhibit the bubble attachment even though the polymer coverage was only $\sim 44.5\%$ based on the AFM imaging. The measured force results in Figure 6.8B could not be fully interpreted by the theoretical model, revealing the complex influence of adsorbed polymer on the bubble-molybdenite interaction and attachment. When the cantilever-anchored bubble approached the mineral surface, an additional repulsion was registered, which was higher than the theoretical calculations (e.g. considering the VDW repulsion and hydrodynamic interaction, while the significantly suppressed EDL interaction was negligible) (see the force data at $t \sim 0.6$ s in Figure 6.8B). Such additional repulsion was most likely attributed to the steric repulsion between the extended polymer

chains on mineral substrate and bubble surface. During retraction of the cantilever, a small adhesion could be measured, which may arise from the interaction of the hydrophobic moieties of polymer chains with the bubble surface in contact during approach. It was noted that molybdenite conditioned at higher polymer concentrations such as 10 and 50 ppm also showed the similar interaction behaviors, and air bubble could not effectively attach to the mineral surface.

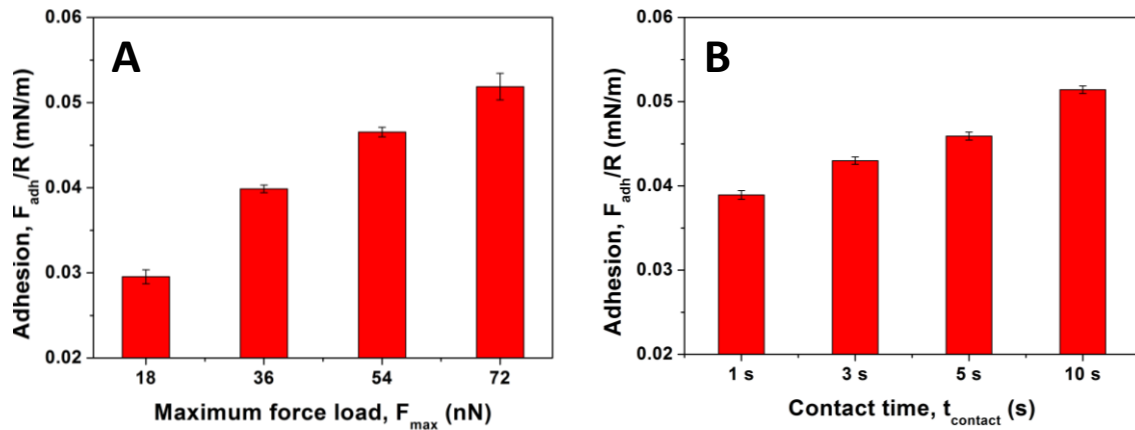


Figure 6.9 Normalized interfacial adhesion F_{adh}/R measured between air bubble and molybdenite surface conditioned in 5 ppm polymer solution at different values of (A) maximum force load F_{max} and (B) contact time $t_{contact}$ at a maximum force load $F_{max} = 18$ nN.

Figure 6.9 shows the effect of maximum force load F_{max} and contact time $t_{contact}$ on the normalized adhesion F_{adh}/R measured between air bubble and molybdenite surface conditioned in 5 ppm polymer solution. As shown in Figure 6.9A, the measured adhesion increased from 0.030 mN/m to 0.052 mN/m with the maximum force load increasing from 18 nN to 72 nN due to the enlarged contact area between the bubble surface and mineral surface. Similarly, with the contact time increasing from 1 s to 10 s, the measured

adhesion increased from 0.040 mN/m to 0.051 mN/m under a maximum force load $F_{max} = 18$ nN, as the hydrophobic domains on molybdenite surface and hydrophobic moieties of polymer chains could have more time to interact with the bubble surface (see Figure 6.9B).

6.3.5 Molybdenite flotation

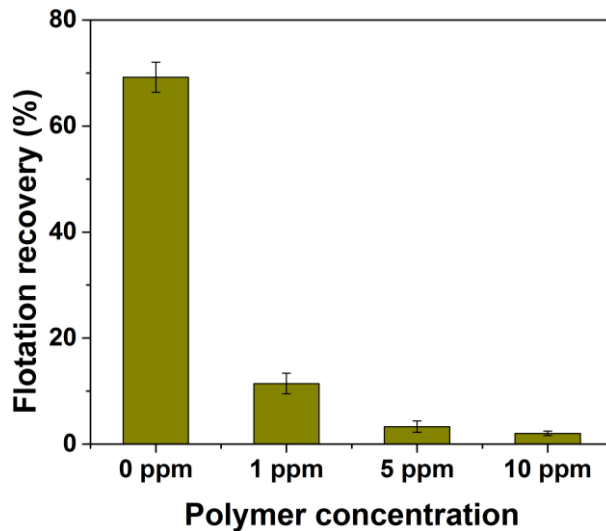


Figure 6.10 Flotation recovery of molybdenite in polymer solution of different concentrations in 100 mM NaCl at pH 9.

Figure 6.10 shows the flotation recovery of molybdenite in 100 mM NaCl with the addition of different concentrations of polymer. The flotation recovery of molybdenite was measured to be 69.2% without the polymer addition, which was dramatically reduced to 11.4% and 3.3% in the presence of 1 ppm and 5 ppm polymer (guar gum) solution, respectively. Further increasing polymer concentration to 10 ppm could not significantly change the flotation recovery (~2%), indicating that conditioning the molybdenite surface in 5 ppm polymer could effectively depress the molybdenite

flotation, which agrees well with the bubble-molybdenite interaction and attachment behaviors in AFM measurements.

6.4 Conclusions

The wettability and surface interactions of molybdenite have attracted tremendous research interest in a wide range of engineering applications, such as froth flotation. In this work, the interaction forces between air bubble and molybdenite mineral surface before/after polymer (i.e. guar gum) treatment were directly measured using bubble probe AFM technique. The AFM imaging showed that ~5.6%, ~44.5% and ~100% mineral surface was respectively covered with the adsorbed polymer after conditioning in 1, 5 and 10 ppm polymer solution, which coincided with the polymer coverage results obtained from contact angle measurements. The direct force measurement results revealed the critical role of electrolyte concentration in bubble-mineral interaction and attachment, which could be analyzed by a theoretical model based on Reynolds lubrication theory and augmented Young-Laplace equation by including the effect of disjoining pressure. It was found that the bubble-molybdenite attachment was enabled in higher NaCl concentration due to the suppressed EDL repulsion. After conditioning in 1 ppm polymer solution, the bubble became more difficult to attach to mineral surface as compared to the pure molybdenite case due to the weakened hydrophobic interaction with a smaller decay length D_0 . With increasing the polymer concentration to 5 ppm, additional steric repulsion between the extended polymer chains and bubble surface could be detected to inhibit the bubble-mineral attachment. This study provides valuable information on the interaction mechanism between air bubble and molybdenite mineral surface at the

nanoscale, with implications for the fundamental understanding of surface interaction mechanisms in many mineral flotation processes and other related engineering operations.

6.5 Acknowledgement

We gratefully acknowledge the financial support from the Natural Sciences and Engineering Research Council of Canada (NSERC), Canadian Centre for Clean Coal/Carbon and Mineral Processing Technologies (C5MPT), the Canada Foundation for Innovation (CFI) and the Alberta Advanced Education & Technology Small Equipment Grants Program (AET/SEGP).

6.6 References

1. Stephenson, T.; Li, Z.; Olsen, B.; Mitlin, D., Lithium Ion Battery Applications of Molybdenum Disulfide (MoS_2) Nanocomposites. *Energy & Environmental Science* **2014**, *7*, 209-231.
2. Gong, Y.; Liu, Z.; Lupini, A. R.; Shi, G.; Lin, J.; Najmaei, S.; Lin, Z.; Elias, A. L.; Berkdemir, A.; You, G., Band Gap Engineering and Layer-by-Layer Mapping of Selenium-Doped Molybdenum Disulfide. *Nano letters* **2013**, *14*, 442-449.
3. Kibsgaard, J.; Chen, Z.; Reinecke, B. N.; Jaramillo, T. F., Engineering the Surface Structure of MoS_2 to Preferentially Expose Active Edge Sites for Electrocatalysis. *Nature materials* **2012**, *11*, 963-969.
4. Radisavljevic, B.; Kis, A., Mobility Engineering and a Metal-Insulator Transition in Monolayer MoS_2 . *Nature materials* **2013**, *12*, 815-820.
5. Cheng, R.; Jiang, S.; Chen, Y.; Liu, Y.; Weiss, N.; Cheng, H.-C.; Wu, H.; Huang, Y.;

Duan, X., Few-Layer Molybdenum Disulfide Transistors and Circuits for High-Speed Flexible Electronics. *Nature communications* **2014**, *5*, 5143.

6. Zhu, W.; Low, T.; Lee, Y.-H.; Wang, H.; Farmer, D. B.; Kong, J.; Xia, F.; Avouris, P., Electronic Transport and Device Prospects of Monolayer Molybdenum Disulphide Grown by Chemical Vapour Deposition. *Nature communications* **2014**, *5*, 3087.

7. Gao, M.-R.; Liang, J.-X.; Zheng, Y.-R.; Xu, Y.-F.; Jiang, J.; Gao, Q.; Li, J.; Yu, S.-H., An Efficient Molybdenum Disulfide/Cobalt Diselenide Hybrid Catalyst for Electrochemical Hydrogen Generation. *Nature communications* **2015**, *6*, 5982.

8. Karunadasa, H. I.; Montalvo, E.; Sun, Y.; Majda, M.; Long, J. R.; Chang, C. J., A Molecular MoS₂ Edge Site Mimic for Catalytic Hydrogen Generation. *Science* **2012**, *335*, 698-702.

9. Zhou, F.; Xin, S.; Liang, H. W.; Song, L. T.; Yu, S. H., Carbon Nanofibers Decorated with Molybdenum Disulfide Nanosheets: Synergistic Lithium Storage and Enhanced Electrochemical Performance. *Angew. Chem., Int. Ed.* **2014**, *53*, 11552-11556.

10. Sun, G.; Zhang, X.; Lin, R.; Yang, J.; Zhang, H.; Chen, P., Hybrid Fibers Made of Molybdenum Disulfide, Reduced Graphene Oxide, and Multi-Walled Carbon Nanotubes for Solid-State, Flexible, Asymmetric Supercapacitors. *Angew. Chem., Int. Ed.* **2015**, *127*, 4734-4739.

11. Narayanan, T. N.; Vusa, C. S.; Alwarappan, S., Selective and Efficient Electrochemical Biosensing of Ultrathin Molybdenum Disulfide Sheets. *Nanotechnology* **2014**, *25*, 335702.

12. Sarkar, D.; Liu, W.; Xie, X.; Anselmo, A. C.; Mitragotri, S.; Banerjee, K., MoS₂ Field-Effect Transistor for Next-Generation Label-Free Biosensors. *Acs Nano* **2014**, *8*,

3992-4003.

13. Winer, W., Molybdenum Disulfide as a Lubricant: A Review of the Fundamental Knowledge. *Wear* **1967**, *10*, 422-452.

14. Gaur, A. P.; Sahoo, S.; Ahmadi, M.; Dash, S. P.; Guinel, M. J.-F.; Katiyar, R. S., Surface Energy Engineering for Tunable Wettability through Controlled Synthesis of MoS₂. *Nano letters* **2014**, *14*, 4314-4321.

15. Govind Rajan, A.; Sresht, V.; Pádua, A. A.; Strano, M. S.; Blankschtein, D., Dominance of Dispersion Interactions and Entropy over Electrostatics in Determining the Wettability and Friction of Two-Dimensional MoS₂ Surfaces. *ACS nano* **2016**, *10*, 9145-9155.

16. Kozbial, A.; Gong, X.; Liu, H.; Li, L., Understanding the Intrinsic Water Wettability of Molybdenum Disulfide (MoS₂). *Langmuir* **2015**, *31*, 8429-8435.

17. Chow, P. K.; Singh, E.; Viana, B. C.; Gao, J.; Luo, J.; Li, J.; Lin, Z.; Elías, A. L.; Shi, Y.; Wang, Z., Wetting of Mono and Few-Layered WS₂ and MoS₂ Films Supported on Si/SiO₂ Substrates. *ACS nano* **2015**, *9*, 3023-3031.

18. Rao, S. R., *Surface Chemistry of Froth Flotation: Volume 1: Fundamentals*; Springer Science & Business Media, **2013**.

19. Fuerstenau, M. C.; Jameson, G. J.; Yoon, R.-H., *Froth Flotation: A Century of Innovation*; SME, **2007**.

20. Xie, L.; Shi, C.; Wang, J.; Huang, J.; Lu, Q.; Liu, Q.; Zeng, H., Probing the Interaction between Air Bubble and Sphalerite Mineral Surface Using Atomic Force Microscope. *Langmuir* **2015**, *31*, 2438-2446.

21. Ralston, J.; Fornasiero, D.; Hayes, R., Bubble-Particle Attachment and Detachment in

- Flotation. *Int. J. Miner. Process.* **1999**, *56*, 133-164.
22. Horn, R. G.; Asadullah, M.; Connor, J. N., Thin Film Drainage: Hydrodynamic and Disjoining Pressures Determined from Experimental Measurements of the Shape of a Fluid Drop Approaching a Solid Wall. *Langmuir* **2006**, *22*, 2610-2619.
23. Tabor, R. F.; Chan, D. Y.; Grieser, F.; Dagastine, R. R., Structural Forces in Soft Matter Systems. *J. Phys. Chem. Lett.* **2011**, *2*, 434-437.
24. Fosu, S.; Skinner, W.; Zanin, M., Detachment of Coarse Composite Sphalerite Particles from Bubbles in Flotation: Influence of Xanthate Collector Type and Concentration. *Miner. Eng.* **2015**, *71*, 73-84.
25. Pugh, R., Macromolecular Organic Depressants in Sulphide Flotation-a Review, 1. Principles, Types and Applications. *Int. J. Miner. Process.* **1989**, *25*, 101-130.
26. Liu, Q.; Zhang, Y.; Laskowski, J., The Adsorption of Polysaccharides onto Mineral Surfaces: An Acid/Base Interaction. *Int. J. Miner. Process.* **2000**, *60*, 229-245.
27. Pearse, M., An Overview of the Use of Chemical Reagents in Mineral Processing. *Miner. Eng.* **2005**, *18*, 139-149.
28. Mierczynska-Vasilev, A.; Ralston, J.; Beattie, D. A., Adsorption of Modified Dextrins on Talc: Effect of Surface Coverage and Hydration Water on Hydrophobicity Reduction. *Langmuir* **2008**, *24*, 6121-6127.
29. Beaussart, A.; Parkinson, L.; Mierczynska-Vasilev, A.; Ralston, J.; Beattie, D. A., Effect of Adsorbed Polymers on Bubble-Particle Attachment. *Langmuir* **2009**, *25*, 13290-13294.
30. Cuba-Chiem, L. T.; Huynh, L.; Ralston, J.; Beattie, D. A., In Situ Particle Film ATR FTIR Spectroscopy of Carboxymethyl Cellulose Adsorption on Talc: Binding Mechanism,

- Ph Effects, and Adsorption Kinetics. *Langmuir* **2008**, *24*, 8036-8044.
31. Kaggwa, G. B.; Huynh, L.; Ralston, J.; Bremmell, K., The Influence of Polymer Structure and Morphology on Talc Wettability. *Langmuir* **2006**, *22*, 3221-3227.
32. Kaggwa, G. B.; Froebe, S.; Huynh, L.; Ralston, J.; Bremmell, K., Morphology of Adsorbed Polymers and Solid Surface Wettability. *Langmuir* **2005**, *21*, 4695-4704.
33. Beaussart, A.; Mierczynska-Vasilev, A.; Beattie, D. A., Adsorption of Dextrin on Hydrophobic Minerals. *Langmuir* **2009**, *25*, 9913-9921.
34. Kor, M.; Korczyk, P. M.; Addai-Mensah, J.; Krasowska, M.; Beattie, D. A., Carboxymethylcellulose Adsorption on Molybdenite: The Effect of Electrolyte Composition on Adsorption, Bubble-Surface Collisions, and Flotation. *Langmuir* **2014**, *30*, 11975-11984.
35. Shi, C.; Chan, D. Y.; Liu, Q.; Zeng, H., Probing the Hydrophobic Interaction between Air Bubbles and Partially Hydrophobic Surfaces Using Atomic Force Microscopy. *J. Phys. Chem. C* **2014**, *118*, 25000-25008.
36. Shi, C.; Cui, X.; Xie, L.; Liu, Q.; Chan, D. Y.; Israelachvili, J. N.; Zeng, H., Measuring Forces and Spatiotemporal Evolution of Thin Water Films between an Air Bubble and Solid Surfaces of Different Hydrophobicity. *ACS nano* **2015**, *9*, 95-104.
37. Vakarelski, I. U.; Lee, J.; Dagastine, R. R.; Chan, D. Y.; Stevens, G. W.; Grieser, F., Bubble Colloidal Afm Probes Formed from Ultrasonically Generated Bubbles. *Langmuir* **2008**, *24*, 603-605.
38. Vakarelski, I. U.; Manica, R.; Tang, X.; O'Shea, S. J.; Stevens, G. W.; Grieser, F.; Dagastine, R. R.; Chan, D. Y., Dynamic Interactions between Microbubbles in Water. *Proc. Natl. Acad. Sci. U. S. A.* **2010**, *107*, 11177-11182.

39. Tabor, R. F.; Chan, D. Y.; Grieser, F.; Dagastine, R. R., Anomalous Stability of Carbon Dioxide in PH-Controlled Bubble Coalescence. *Angew. Chem., Int. Ed.* **2011**, *123*, 3516-3518.
40. Manor, O.; Vakarelski, I. U.; Tang, X.; O'Shea, S. J.; Stevens, G. W.; Grieser, F.; Dagastine, R. R.; Chan, D. Y., Hydrodynamic Boundary Conditions and Dynamic Forces between Bubbles and Surfaces. *Phys. Rev. Lett.* **2008**, *101*, 024501.
41. Tabor, R. F.; Manica, R.; Chan, D. Y.; Grieser, F.; Dagastine, R. R., Repulsive Van Der Waals Forces in Soft Matter: Why Bubbles Do Not Stick to Walls. *Phys. Rev. Lett.* **2011**, *106*, 064501.
42. Manor, O.; Vakarelski, I. U.; Stevens, G. W.; Grieser, F.; Dagastine, R. R.; Chan, D. Y., Dynamic Forces between Bubbles and Surfaces and Hydrodynamic Boundary Conditions. *Langmuir* **2008**, *24*, 11533-11543.
43. Chan, D. Y.; Klaseboer, E.; Manica, R., Theory of Non-Equilibrium Force Measurements Involving Deformable Drops and Bubbles. *Adv. Colloid Interface Sci.* **2011**, *165*, 70-90.
44. Tabor, R. F.; Grieser, F.; Dagastine, R. R.; Chan, D. Y., Measurement and Analysis of Forces in Bubble and Droplet Systems Using AFM. *J. Colloid Interface Sci.* **2012**, *371*, 1-14.
45. Cui, X.; Shi, C.; Xie, L.; Liu, J.; Zeng, H., Probing Interactions between Air Bubble and Hydrophobic Polymer Surface: Impact of Solution Salinity and Interfacial Nanobubbles. *Langmuir* **2016**, *32*, 11236–11244.
46. Hutter, J. L.; Bechhoefer, J., Calibration of Atomic-Force Microscope Tips. *Rev. Sci. Instrum.* **1993**, *64*, 1868-1873.

47. Israelachvili, J. N., *Intermolecular and Surface Forces: Revised Third Edition*; Academic press, **2011**.
48. Raghavan, S.; Hsu, L. L., Factors Affecting the Flotation Recovery of Molybdenite from Porphyry Copper Ores. *Int. J. Miner. Process.* **1984**, *12*, 145-162.
49. Wie, J. M.; Fuerstenau, D., The Effect of Dextrin on Surface Properties and the Flotation of Molybdenite. *Int. J. Miner. Process.* **1974**, *1*, 17-32.
50. Lu, Z.; Liu, Q.; Xu, Z.; Zeng, H., Probing Anisotropic Surface Properties of Molybdenite by Direct Force Measurements. *Langmuir* **2015**, *31*, 11409-11418.
51. Beaussart, A.; Mierczynska-Vasilev, A.; Beattie, D. A., Evolution of Carboxymethyl Cellulose Layer Morphology on Hydrophobic Mineral Surfaces: Variation of Polymer Concentration and Ionic Strength. *J. Colloid Interface Sci.* **2010**, *346*, 303-310.
52. Yang, C.; Dabros, T.; Li, D.; Czarnecki, J.; Masliyah, J. H., Measurement of the Zeta Potential of Gas Bubbles in Aqueous Solutions by Microelectrophoresis Method. *J. Colloid Interface Sci.* **2001**, *243*, 128-135.
53. Cho, S.-H.; Kim, J.-Y.; Chun, J.-H.; Kim, J.-D., Ultrasonic Formation of Nanobubbles and Their Zeta-Potentials in Aqueous Electrolyte and Surfactant Solutions. *Colloids Surf., A* **2005**, *269*, 28-34.
54. Han, M.; Kim, M.; Shin, M., Generation of a Positively Charged Bubble and Its Possible Mechanism of Formation. *J. Water Supply Res. Technol. AQUA* **2006**, *55*, 471-478.
55. Yaminsky, V. V.; Ohnishi, S.; Vogler, E. A.; Horn, R. G., Stability of Aqueous Films between Bubbles. Part 1. The Effect of Speed on Bubble Coalescence in Purified Water and Simple Electrolyte Solutions. *Langmuir* **2010**, *26*, 8061-8074.

56. Clark, M. M., *Transport Modeling for Environmental Engineers and Scientists*; John Wiley & Sons, **2011**.
57. Christenson, H. K.; Claesson, P. M., Cavitation and the Interaction between Macroscopic Hydrophobic Surfaces. *Science* **1988**, *239*, 390-392.
58. Tsao, Y.-H.; Evans, D. F.; Wennerstrom, H., Long-Range Attractive Force between Hydrophobic Surfaces Observed by Atomic Force Microscopy. *Science* **1993**, *262*, 547-550.

Chapter 7 Conclusions and Future Work

7.1 Major conclusions

In this study, the surface characteristics of sulfide minerals, including sphalerite, galena and molybdenite, were probed in complex aqueous media using several complementary experimental techniques, aiming to understand the flotation related interfacial phenomena such as surface heterogeneity, electrochemical properties and bubble-particle interaction mechanisms at the nanoscale.

The nanoscale heterogeneity of surface hydrophobicity and surface interactions on sphalerite surface before/after conditioning treatment were studied using AFM force mapping, which revealed that the adhesion on sphalerite fell in a narrow range with a peak centered at 16.4 mN/m, and the adhesion on conditioned sphalerite fell in a wide range with a small peak centered at 15.5 mN/m and a large peak centered at 58.1 mN/m. It was clear that the conditioning treatment changed the chemical characteristics of mineral surface by keeping some domains unchanged while endowing other domains different degrees of hydrophobicity due to non-uniform adsorption of xanthate. The additional hydrophobic attraction with the decay length varying from 0.7 nm to 1.2 nm was found on the different hydrophobic domains.

Equipped with the electrochemical setup, the evolution of surface characteristics on galena surface was measured at the nanoscale with simultaneous modulation of interfacial chemical reaction using an EC-AFM. In situ topographic imaging revealed the slight surface roughening of galena at an applied potential of 0 V (0.206 V vs SHE) and more pronounced surface roughening at higher potentials such as 0.3 V and 0.45 V. With the applied potential increasing from -0.7 V to 0.45 V, the measured force results showed

long-range attraction with increased “jump-in” distance due to the enhanced surface hydrophobicity as confirmed by contact angle measurements. Fitted by the extended DLVO theory including the effect of hydrophobic interaction, the decay length of hydrophobic interaction was found to increase from 0.8 nm to 1.3 nm. The electrochemical oxidation at 0 V arose from the formation of metal-deficient lead sulfide, while the formation of elemental sulfur at 0.45 V was further confirmed by cryo-XPS.

In addition, the interaction forces between air bubbles and mineral surfaces (i.e. sphalerite before/after conditioning treatment and molybdenite before/after depressant adsorption) were systematically probed using an AFM bubble probe technique. The quantitative force measurements revealed the critical role of surface forces in bubble-mineral interaction and attachment. The theoretical calculations based on the Reynolds lubrication theory and augmented Young-Laplace equation by including the effect of disjoining pressure provided excellent agreement with the measured force results, and the weakened EDL disjoining pressure at high salt concentration facilitated the bubble-mineral attachment. For the bubble-sphalerite interaction, hydrophobic disjoining pressure was found to be stronger on the conditioned mineral, thereby enabling thin water film rupture and bubble-mineral attachment. For the bubble-molybdenite interaction, the adsorption of polymer depressant at 1 ppm (~5.6% surface coverage) could weaken the hydrophobic attraction, and thus the bubble became more difficult to attach to mineral surface as compared to the pure molybdenite case. The polymer concentration of 5 ppm was sufficiently high to stabilize thin water film and inhibit bubble-mineral attachment due to the steric repulsion even if the polymer coverage was only ~44.5%.

7.2 Original contributions

This work provided the first feasible methodologies to investigate the surface heterogeneity, electrochemical properties and bubble-particle interaction mechanisms of mineral particles in complex aqueous media at the nanoscale. The AFM force mapping was applied for the first time to quantitatively probe the distribution of surface hydrophobicity and surface interactions of the hydrophilic/hydrophobic domains on mineral surfaces. The nanoscale heterogeneity of surface hydrophobicity was verified on mineral surface, and these existed hydrophobic domains could provide the anchoring sites for preferential attachment of nanobubbles that would facilitate the attachment of fine particles to conventional sized bubbles. This method provided insights into improving the efficiency of fine particle flotation by modulating the size and distribution of hydrophobic domains in various solution conditions.

The application of EC-AFM in the investigation of in-situ evolution of morphological changes and surface interactions on mineral surface (i.e. galena) provided important contribution to uncovering the electrochemical reaction and surface interaction mechanisms on electrochemically polarized minerals. This technique successfully solved the challenging issues of surface variation after long-term exposure to air or aqueous solution in conventional surface analysis methods. The measured results revealed that the electrochemical oxidation changed the morphology of mineral surface due to the formed hydrophobic species, which could effectively enhance the hydrophobic attraction and adhesion with hydrophobic particles. It is critical to modulate the interactions and optimize the processing conditions towards the development of more cost-effective and environment-friendly flotation technology without reagent addition.

Different from the direct AFM force measurements between two solid surfaces, the quantitative measurement of interaction forces involving deformable air bubbles were far more complicated than that of solid surfaces due to the practical difficulties in precise manipulation of air bubble and interpretation of measured force results. The application of AFM bubble probe in the bubble-mineral interactions demonstrated the critical role of hydrodynamic condition, salt concentration and reagent conditioning in the attachment of air bubbles on both inherently hydrophilic and hydrophobic minerals. The results for the first time provided valuable information on the basic understanding of the interaction mechanisms between air bubbles and mineral surfaces at the nanoscale, which offered insights into the design of novel reagents (e.g. collector, depressant) to modulate the bubble attachment efficiency in froth flotation.

7.3 Suggestions for future work

1) The interaction mechanisms among air bubbles, mineral particles and gangue particles were investigated in relatively simple aqueous systems. More complicated environments with the combined effects of water chemistry (e.g. pH, ion type and concentration), reagent addition (e.g. surfactant, collector and depressant) and fine particle addition should be further investigated.

2) It is critical to apply the combined technique based on AFM force mapping, EC-AFM and AFM bubble probe to modulate the surface heterogeneity, electrochemical properties and bubble-mineral attachment toward the development of more cost-effective and environment-friendly flotation technology. All these complementary experimental

techniques could also be further extended to other mineral system, especially for complex polymetallic sulfide ores.

3) The novel chemical reagents should be designed to optimize the flotation selectivity of chalcopyrite/molybdenite by investigating the effects of polymer depressant with different chemical structures on the surface properties and bubble-particle interaction of chalcopyrite and molybdenite.

Bibliography

- (1) Klassen, V. I.; Mokrousov, V. A., *An Introduction to the Theory of Flotation*; Butterworths, **1963**.
- (2) Fuerstenau, M. C.; Jameson, G. J.; Yoon, R. H., *Froth Flotation: A Century of Innovation*; SME, **2007**.
- (3) Leja, J., *Surface Chemistry of Froth Flotation*; Plenum Press, **1982**.
- (4) Fuerstenau, M. C.; Miller, J. D.; Kuhn, M. C., *Chemistry of Flotation*; Random House Trade, **1985**.
- (5) Chandra, A.; Gerson, A., A Review of the Fundamental Studies of the Copper Activation Mechanisms for Selective Flotation of the Sulfide Minerals, Sphalerite and Pyrite. *Adv. Colloid Interface Sci.* **2009**, *145*, 97-110.
- (6) Wittstock, G.; Kartio, I.; Hirsch, D.; Kunze, S.; Szargan, R., Oxidation of Galena in Acetate Buffer Investigated by Atomic Force Microscopy and Photoelectron Spectroscopy. *Langmuir* **1996**, *12*, 5709-5721.
- (7) Beaussart, A.; Mierczynska-Vasilev, A.; Beattie, D. A., Adsorption of Dextrin on Hydrophobic Minerals. *Langmuir* **2009**, *25*, 9913-9921.
- (8) Kor, M.; Korczyk, P. M.; Addai-Mensah, J.; Krasowska, M.; Beattie, D. A., Carboxymethylcellulose Adsorption on Molybdenite: The Effect of Electrolyte Composition on Adsorption, Bubble-Surface Collisions, and Flotation. *Langmuir* **2014**, *30*, 11975-11984.
- (9) Liu, Q.; Zhang, Y.; Laskowski, J., The Adsorption of Polysaccharides onto Mineral Surfaces: An Acid/Base Interaction. *Int. J. Miner. Process.* **2000**, *60*, 229-245.
- (10) Nagaraj, D.; Ravishankar, S., Flotation Reagents-a Critical Overview from an

Industry Perspective. *Froth Flotation: A Century of Innovation*. Society for Mining, Metallurgy, and Exploration, Littleton, Colorado **2007**, 375-424.

(11) Wang, B.; Peng, Y., The Effect of Saline Water on Mineral Flotation-a Critical Review. *Miner. Eng.* **2014**, *66*, 13-24.

(12) Castro, S. In *Challenges in Flotation of Cu-Mo Sulfide Ores in Sea Water*, Water in Mineral Processing-Proc. of the First International Symposium, SME, **2012**.

(13) Farrokhpay, S.; Zanin, M., An Investigation into the Effect of Water Quality on Froth Stability. *Adv. Powder. Technol.* **2012**, *23*, 493-497.

(14) Miettinen, T.; Ralston, J.; Fornasiero, D., The Limits of Fine Particle Flotation. *Miner. Eng.* **2010**, *23*, 420-437.

(15) Rao, K.; Chernyshova, I., Challenges in Sulphide Mineral Processing. *Open. Miner. Process. J.* **2011**, *4*, 7-13.

(16) Castro, S.; Laskowski, J. S., Froth Flotation in Saline Water. *KONA. Powder. Part. J.* **2011**, *29*, 4-15.

(17) Moreno, P. A.; Aral, H.; Cuevas, J.; Monardes, A.; Adaro, M.; Norgate, T.; Bruckard, W., The Use of Seawater as Process Water at Las Luces Coppe-Molybdenum Beneficiation Plant in Taltal (Chile). *Miner. Eng.* **2011**, *24*, 852-858.

(18) Du, H.; Miller, J. D., Interfacial Water Structure and Surface Charge of Selected Alkali Chloride Salt Crystals in Saturated Solutions: A Molecular Dynamics Modeling Study. *J. Phys. Chem. C* **2007**, *111*, 10013-10022.

(19) Hewitt, D.; Fornasiero, D.; Ralston, J., Bubble Particle Attachment Efficiency. *Miner. Eng.* **1994**, *7*, 657-665.

(20) Israelachvili, J. N., *Intermolecular and Surface Forces*; Academic Press: London,

1991.

(21) Cheng, Y. T.; Rodak, D.; Wong, C.; Hayden, C., Effects of Micro-and Nano-Structures on the Self-Cleaning Behaviour of Lotus Leaves. *Nanotechnology* **2006**, *17*, 1359.

(22) Sánchez-Iglesias, A.; Grzelczak, M.; Altantzis, T.; Goris, B.; Perez-Juste, J.; Bals, S.; Van Tendeloo, G.; Donaldson Jr, S. H.; Chmelka, B. F.; Israelachvili, J. N., Hydrophobic Interactions Modulate Self-Assembly of Nanoparticles. *ACS nano* **2012**, *6*, 11059-11065.

(23) Meyer, E. E.; Rosenberg, K. J.; Israelachvili, J., Recent Progress in Understanding Hydrophobic Interactions. *Proc. Natl. Acad. Sci. U. S. A.* **2006**, *103*, 15739-15746.

(24) Zeng, H.; Shi, C.; Huang, J.; Li, L.; Liu, G.; Zhong, H., Recent Experimental Advances on Hydrophobic Interactions at Solid/Water and Fluid/Water Interfaces. *Biointerphases* **2016**, *11*, 018903.

(25) Butt, H.-J.; Cappella, B.; Kappl, M., Force Measurements with the Atomic Force Microscope: Technique, Interpretation and Applications. *Surf. Sci. Rep.* **2005**, *59*, 1-152.

(26) Binnig, G.; Quate, C. F.; Gerber, C., Atomic Force Microscope. *Phys. Rev. Lett.* **1986**, *56*, 930.

(27) Cappella, B.; Dietler, G., Force-Distance Curves by Atomic Force Microscopy. *Surf. Sci. Rep.* **1999**, *34*, 1-104.

(28) Hinterdorfer, P.; Dufrêne, Y. F., Detection and Localization of Single Molecular Recognition Events Using Atomic Force Microscopy. *Nature methods* **2006**, *3*, 347-355.

(29) Katan, A. J.; Van Es, M. H.; Oosterkamp, T. H., Quantitative Force Versus Distance Measurements in Amplitude Modulation Afm: A Novel Force Inversion Technique. *Nanotechnology* **2009**, *20*, 165703.

- (30) Ducker, W. A.; Senden, T. J.; Pashley, R. M., Direct Measurement of Colloidal Forces Using an Atomic Force Microscope. *Nature* **1991**, *353*, 239-241.
- (31) Butt, H.-J., A Technique for Measuring the Force between a Colloidal Particle in Water and a Bubble. *J. Colloid Interface Sci.* **1994**, *166*, 109-117.
- (32) Gillies, G.; Kappl, M.; Butt, H.-J., Direct Measurements of Particle–Bubble Interactions. *Adv. Colloid Interface Sci.* **2005**, *114*, 165-172.
- (33) Johnson, D. J.; Miles, N. J.; Hilal, N., Quantification of Particle–Bubble Interactions Using Atomic Force Microscopy: A Review. *Adv. Colloid Interface Sci.* **2006**, *127*, 67-81.
- (34) Ducker, W. A.; Xu, Z.; Israelachvili, J. N., Measurements of Hydrophobic and DLVO Forces in Bubble-Surface Interactions in Aqueous Solutions. *Langmuir* **1994**, *10*, 3279-3289.
- (35) Fielden, M. L.; Hayes, R. A.; Ralston, J., Surface and Capillary Forces Affecting Air Bubble-Particle Interactions in Aqueous Electrolyte. *Langmuir* **1996**, *12*, 3721-3727.
- (36) Attard, P.; Miklavcic, S. J., Effective Spring Constant of Bubbles and Droplets. *Langmuir* **2001**, *17*, 8217-8223.
- (37) Chan, D. Y.; Klaseboer, E.; Manica, R., Film Drainage and Coalescence between Deformable Drops and Bubbles. *Soft Matter* **2011**, *7*, 2235-2264.
- (38) Tabor, R. F.; Grieser, F.; Dagastine, R. R.; Chan, D. Y., Measurement and Analysis of Forces in Bubble and Droplet Systems Using Afm. *J. Colloid Interface Sci.* **2012**, *371*, 1-14.
- (39) Dagastine, R. R.; Manica, R.; Carnie, S. L.; Chan, D.; Stevens, G. W.; Grieser, F., Dynamic Forces between Two Deformable Oil Droplets in Water. *Science* **2006**, *313*, 210-213.

- (40) Vakarelski, I. U.; Manica, R.; Tang, X.; O'Shea, S. J.; Stevens, G. W.; Grieser, F.; Dagastine, R. R.; Chan, D. Y., Dynamic Interactions between Microbubbles in Water. *Proc. Natl. Acad. Sci. U. S. A.* **2010**, *107*, 11177-11182.
- (41) Tabor, R. F.; Chan, D. Y.; Grieser, F.; Dagastine, R. R., Anomalous Stability of Carbon Dioxide in Ph-Controlled Bubble Coalescence. *Angew. Chem., Int. Ed.* **2011**, *50*, 3454-3456.
- (42) Manor, O.; Vakarelski, I. U.; Tang, X.; O'Shea, S. J.; Stevens, G. W.; Grieser, F.; Dagastine, R. R.; Chan, D. Y., Hydrodynamic Boundary Conditions and Dynamic Forces between Bubbles and Surfaces. *Phys. Rev. Lett.* **2008**, *101*, 024501.
- (43) Tabor, R. F.; Manica, R.; Chan, D. Y.; Grieser, F.; Dagastine, R. R., Repulsive Van Der Waals Forces in Soft Matter: Why Bubbles Do Not Stick to Walls. *Phys. Rev. Lett.* **2011**, *106*, 064501.
- (44) Manor, O.; Vakarelski, I. U.; Stevens, G. W.; Grieser, F.; Dagastine, R. R.; Chan, D. Y., Dynamic Forces between Bubbles and Surfaces and Hydrodynamic Boundary Conditions. *Langmuir* **2008**, *24*, 11533-11543.
- (45) Shi, C.; Chan, D. Y.; Liu, Q.; Zeng, H., Probing Hydrophobic Interaction between Air Bubble and Partially Hydrophobic Surfaces Using Atomic Force Microscopy. *J. Phys. Chem. C* **2014**, *118*, 25000-25008.
- (46) Teng, F.; Liu, Q.; Zeng, H., In Situ Kinetic Study of Zinc Sulfide Activation Using a Quartz Crystal Microbalance with Dissipation (QCM-D). *J. Colloid Interface Sci.* **2012**, *368*, 512-520.
- (47) Deng, M., Impact of Gypsum Supersaturated Solution on the Flotation of Sphalerite. University of Alberta, **2013**.

- (48) Xie, L.; Shi, C.; Wang, J.; Huang, J.; Lu, Q.; Liu, Q.; Zeng, H., Probing the Interaction between Air Bubble and Sphalerite Mineral Surface Using Atomic Force Microscope. *Langmuir* **2015**, *31*, 2438-2446.
- (49) Shi, C.; Cui, X.; Xie, L.; Liu, Q.; Chan, D. Y.; Israelachvili, J. N.; Zeng, H., Measuring Forces and Spatiotemporal Evolution of Thin Water Films between an Air Bubble and Solid Surfaces of Different Hydrophobicity. *ACS nano* **2014**, *9*, 95-104.
- (50) Cui, X.; Shi, C.; Xie, L.; Liu, J.; Zeng, H., Probing Interactions between Air Bubble and Hydrophobic Polymer Surface: Impact of Solution Salinity and Interfacial Nanobubbles. *Langmuir* **2016**, *32*, 11236–11244.
- (51) Zhou, R.; Huang, X.; Margulis, C. J.; Berne, B. J., Hydrophobic Collapse in Multidomain Protein Folding. *Science* **2004**, *305*, 1605-1609.
- (52) Dyson, H. J.; Wright, P. E.; Scheraga, H. A., The Role of Hydrophobic Interactions in Initiation and Propagation of Protein Folding. *Proc. Natl. Acad. Sci. U. S. A.* **2006**, *103*, 13057-13061.
- (53) Chandler, D., Interfaces and the Driving Force of Hydrophobic Assembly. *Nature* **2005**, *437*, 640-647.
- (54) Wang, C.-W.; Sinton, D.; Moffitt, M. G., Flow-Directed Block Copolymer Micelle Morphologies Via Microfluidic Self-Assembly. *J. Am. Chem. Soc.* **2011**, *133*, 18853-18864.
- (55) Mao, Z.; Xu, H.; Wang, D., Molecular Mimetic Self-Assembly of Colloidal Particles. *Adv. Funct. Mater.* **2010**, *20*, 1053-1074.
- (56) Ma, F.; Wang, S.; Zhao, H.; Wu, D. T.; Wu, N., Colloidal Structures of Asymmetric Dimers Via Orientation-Dependent Interactions. *Soft matter* **2014**, *10*, 8349-8357.

- (57) Xie, L.; Wang, J.; Shi, C.; Huang, J.; Zhang, H.; Liu, Q.; Liu, Q.; Zeng, H., Probing Surface Interactions of Electrochemically Active Galena Mineral Surface Using Atomic Force Microscope. *J. Phys. Chem. C* **2016**, *120*, 22433–22442.
- (58) Schuler, B.; Lipman, E. A.; Eaton, W. A., Probing the Free-Energy Surface for Protein Folding with Single-Molecule Fluorescence Spectroscopy. *Nature* **2002**, *419*, 743-747.
- (59) Chau, T.; Bruckard, W.; Koh, P.; Nguyen, A., A Review of Factors That Affect Contact Angle and Implications for Flotation Practice. *Adv. Colloid Interface Sci.* **2009**, *150*, 106-115.
- (60) Chau, T., A Review of Techniques for Measurement of Contact Angles and Their Applicability on Mineral Surfaces. *Miner. Eng.* **2009**, *22*, 213-219.
- (61) Rao, S. R., *Surface Chemistry of Froth Flotation: Volume 1: Fundamentals*; Springer Science & Business Media, **2013**.
- (62) Fuerstenau, M. C.; Jameson, G. J.; Yoon, R.-H., *Froth Flotation: A Century of Innovation*; SME, **2007**.
- (63) Kelly, E. G.; Spottiswood, D. J., *Introduction to Mineral Processing*; Wiley New York, **1982**.
- (64) Leppinen, J.; Basilio, C.; Yoon, R., In-Situ FTIR Study of Ethyl Xanthate Adsorption on Sulfide Minerals under Conditions of Controlled Potential. *Int. J. Miner. Process.* **1989**, *26*, 259-274.
- (65) Larsson, M.; Holmgren, A.; Forsling, W., Xanthate Adsorbed on ZnS Studied by Polarized FTIR-ATR Spectroscopy. *Langmuir* **2000**, *16*, 8129-8133.
- (66) Mielczarski, J., XPS Study of Ethyl Xanthate Adsorption on Oxidized Surface of

Cuprous Sulfide. *J. Colloid Interface Sci.* **1987**, *120*, 201-209.

(67) Page, P.; Hazell, L., X-Ray Photoelectron Spectroscopy (XPS) Studies of Potassium Amyl Xanthate (Kax) Adsorption on Precipitated PbS Related to Galena Flotation. *Int. J. Miner. Process.* **1989**, *25*, 87-100.

(68) Woods, R.; Hope, G. A.; Watling, K., Surface Enhanced Raman Scattering Spectroscopic Studies of the Adsorption of Flotation Collectors. *Miner. Eng.* **2000**, *13*, 345-356.

(69) Buckley, A.; Parks, T.; Vassallo, A.; Woods, R., Verification by Surface-Enhanced Raman Spectroscopy of the Integrity of Xanthate Chemisorbed on Silver. *Int. J. Miner. Process.* **1997**, *51*, 303-313.

(70) Brinen, J.; Reich, F., Static Sims Imaging of the Adsorption of Diisobutyl Dithiophosphate on Galena Surfaces. *Surf. Interface Anal.* **1992**, *18*, 448-452.

(71) Brinen, J.; Greenhouse, S.; Nagaraj, D.; Lee, J., Sims and Sims Imaging Studies of Adsorbed Dialkyl Dithiophosphinates on PbS Crystal Surfaces. *Int. J. Miner. Process.* **1993**, *38*, 93-109.

(72) Stowe, K.; Chryssoulis, S.; Kim, J., Mapping of Composition of Mineral Surfaces by Tof-Sims. *Miner. Eng.* **1995**, *8*, 421-430.

(73) Piantadosi, C.; Jasieniak, M.; Skinner, W.; Smart, R. S. C., Statistical Comparison of Surface Species in Flotation Concentrates and Tails from Tof-Sims Evidence. *Miner. Eng.* **2000**, *13*, 1377-1394..

(74) Brito e Abreu, S.; Brien, C.; Skinner, W., Tof-Sims as a New Method to Determine the Contact Angle of Mineral Surfaces. *Langmuir* **2010**, *26*, 8122-8130.

(75) BARD, A.; FAN, F.; Pierce, D. T.; Unwin, P. R.; Wipf, D. O.; Zhou, F., Chemical

Imaging of Surfaces with the Scanning Electrochemical Microscope. *Science* **1991**, *254*, 68-74.

(76) Wang, J.; Liu, Q.; Zeng, H., Understanding Copper Activation and Xanthate Adsorption on Sphalerite by Time-of-Flight Secondary Ion Mass Spectrometry, X-Ray Photoelectron Spectroscopy, and in Situ Scanning Electrochemical Microscopy. *J. Phys. Chem. C* **2013**, *117*, 20089-20097.

(77) Ducker, W. A.; Senden, T. J.; Pashley, R. M., Direct Measurement of Colloidal Forces Using an Atomic Force Microscope. *Nature* **1991**, *353*, 239-241.

(78) Yang, D.; Xie, L.; Bobicki, E.; Xu, Z.; Liu, Q.; Zeng, H., Probing Anisotropic Surface Properties and Interaction Forces of Chrysotile Rods by Atomic Force Microscopy and Rheology. *Langmuir* **2014**, *30*, 10809-10817.

(79) Wang, J.; Li, J.; Xie, L.; Shi, C.; Liu, Q.; Zeng, H., Interactions between Elemental Selenium and Hydrophilic/Hydrophobic Surfaces: Direct Force Measurements Using AFM. *Chem. Eng. J.* **2016**, *303*, 646-654.

(80) Shi, C.; Zhang, L.; Xie, L.; Lu, X.; Liu, Q.; Mantilla, C. A.; van den Berg, F. G.; Zeng, H., Interaction Mechanism of Oil-in-Water Emulsions with Asphaltenes Determined Using Droplet Probe AFM. *Langmuir* **2016**, *32*, 2302-2310.

(81) Gao, Z.; Hu, Y.; Sun, W.; Drelich, J. W., Surface Charge Anisotropy of Scheelite Crystals. *Langmuir* **2016**, *32*, 6282-6288.

(82) He, Y.; Tian, Y.; Ribbe, A. E.; Mao, C., Highly Connected Two-Dimensional Crystals of DNA Six-Point-Stars. *J. Am. Chem. Soc.* **2006**, *128*, 15978-15979.

(83) Frisbie, C. D.; Rozsnyai, L. F.; Noy, A.; Wrighton, M. S.; Lieber, C. M., Functional Group Imaging by Chemical Force Microscopy. *Science* **1994**, *265*, 2071-2074.

- (84) Noy, A.; Vezenov, D. V.; Lieber, C. M., Chemical Force Microscopy. *Annu. Rev. Mater. Sci.* **1997**, *27*, 381-421.
- (85) Noy, A.; Frisbie, C. D.; Rozsnyai, L. F.; Wrighton, M. S.; Lieber, C. M., Chemical Force Microscopy: Exploiting Chemically-Modified Tips to Quantify Adhesion, Friction, and Functional Group Distributions in Molecular Assemblies. *J. Am. Chem. Soc.* **1995**, *117*, 7943-7951.
- (86) Vezenov, D. V.; Noy, A.; Rozsnyai, L. F.; Lieber, C. M., Force Titrations and Ionization State Sensitive Imaging of Functional Groups in Aqueous Solutions by Chemical Force Microscopy. *J. Am. Chem. Soc.* **1997**, *119*, 2006-2015.
- (87) Dague, E.; Alsteens, D.; Latgé, J.-P.; Verbelen, C.; Raze, D.; Baulard, A. R.; Dufrêne, Y. F., Chemical Force Microscopy of Single Live Cells. *Nano letters* **2007**, *7*, 3026-3030.
- (88) Alsteens, D.; Dague, E.; Rouxhet, P. G.; Baulard, A. R.; Dufrêne, Y. F., Direct Measurement of Hydrophobic Forces on Cell Surfaces Using AFM. *Langmuir* **2007**, *23*, 11977-11979.
- (89) Hutter, J. L.; Bechhoefer, J., Calibration of Atomic-Force Microscope Tips. *Rev. Sci. Instrum.* **1993**, *64*, 1868-1873.
- (90) Drelich, J.; Long, J.; Yeung, A., Determining Surface Potential of the Bitume-Water Interface at Nanoscale Resolution Using Atomic Force Microscopy. *Can. J. Chem. Eng.* **2007**, *85*, 625-634.
- (91) Van Oss, C. J., *Interfacial Forces in Aqueous Media*; CRC press, **2006**.
- (92) Wang, J.; Xie, L.; Liu, Q.; Zeng, H., Effects of Salinity on Xanthate Adsorption on Sphalerite and Bubble-Sphalerite Interactions. *Miner. Eng.* **2015**, *77*, 34-41.
- (93) Szargan, R.; Karthe, S.; Suoninen, E., XPS Studies of Xanthate Adsorption on Pyrite.

Appl. Surf. Sci. **1992**, *55*, 227-232.

(94) Ranta, L.; Minni, E.; Suoninen, E.; Heimala, S.; Hintikka, V.; Saari, M.; Rastas, J., XPS Studies of Adsorption of Xanthate on Sulfide Surfaces. *Appl. Surf. Sci.* **1992**, *55*, 227-232

(95) Somasundaran, P., *Encyclopedia of Surface and Colloid Science*; CRC press, **2006**; Vol. 2.

(96) Love, J. C.; Estroff, L. A.; Kriebel, J. K.; Nuzzo, R. G.; Whitesides, G. M., Self-Assembled Monolayers of Thiolates on Metals as a Form of Nanotechnology. *Chem. Rev.* **2005**, *105*, 1103-1170.

(97) Toikka, G.; Hayes, R. A.; Ralston, J., Surface Forces between Spherical ZnS Particles in Aqueous Electrolyte. *Langmuir* **1996**, *12*, 3783-3788.

(98) Park, J. Y. *Current Trends of Surface Science and Catalysis*; Springer Science & Business Media: New York, **2014**.

(99) Roucoux, A.; Schulz, J.; Patin, H. Reduced Transition Metal Colloids: A Novel Family of Reusable Catalysts? *Chem. Rev.* **2002**, *102*, 3757-3778.

(100) Frey, N. A.; Peng, S.; Cheng, K.; Sun, S. Magnetic Nanoparticles: Synthesis, Functionalization, and Applications in Bioimaging and Magnetic Energy Storage. *Chem. Soc. Rev.* **2009**, *38*, 2532-2542.

(101) Feng, X. *Nanocarbons for Advanced Energy Storage*; John Wiley & Sons: Weinheim, **2015**.

(102) Farrokhpay, S. The Significance of Froth Stability in Mineral Flotation-a Review. *Adv. Colloid Interface Sci.* **2011**, *166*, 1-7.

(103) Smith, M. C.; Gilbert, J. A.; Mawdsley, J. R.; Seifert, S. N.; Myers, D. J. In Situ

Small-Angle X-Ray Scattering Observation of Pt Catalyst Particle Growth During Potential Cycling. *J. Am. Chem. Soc.* **2008**, *130*, 8112-8113.

(104) Raimondi, F.; Scherer, G. G.; Kötzt, R.; Wokaun, A. Nanoparticles in Energy Technology: Examples from Electrochemistry and Catalysis. *Angew. Chem. Int. Ed.* **2005**, *44*, 2190-2209.

(105) Hu, Y.; Sun, W.; Wang, D. *Electrochemistry of Flotation of Sulphide Minerals*; Springer Science & Business Media: Berlin, **2009**.

(106) Tolley, W.; Kotlyar, D.; Van Wagoner, R. Fundamental Electrochemical Studies of Sulfide Mineral Flotation. *Miner. Eng.* **1996**, *9*, 603-637.

(107) Buckley, A.; Woods, R. X-Ray Photoelectron Spectroscopic and Electrochemical Studies of the Interaction of Xanthate with Galena in Relation to the Mechanism Proposed by Page and Hazell. *Int. J. Miner. Process.* **1990**, *28*, 301-311.

(108) Nowak, P.; Laajalehto, K.; Kartio, I. A Flotation Related X-Ray Photoelectron Spectroscopy Study of the Oxidation of Galena Surface. *Colloids Surf., A* **2000**, *161*, 447-460.

(109) Shapter, J.; Brooker, M.; Skinner, W. M. Observation of the Oxidation of Galena using Raman Spectroscopy. *Int. J. Miner. Process.* **2000**, *60*, 199-211.

(110) Turcotte, S.; Benner, R.; Riley, A.; Li, J.; Wadsworth, M.; Bodily, D. Surface Analysis of Electrochemically Oxidized Metal Sulfides using Raman Spectroscopy. *J. Electroanal. Chem.* **1993**, *347*, 195-205.

(111) Chernyshova, I. In Situ FTIR-Spectroelectrochemical Study of the Anodic Processes on a Galena (PbS) Electrode under Open-Air Conditions in the Absence and Presence of N-Butyl Xanthate. *Langmuir* **2002**, *18*, 6962-6968.

- (112) Smart, R. S. C.; Jasieniak, M.; Prince, K.; Skinner, W. SIMS Studies of Oxidation Mechanisms and Polysulfide Formation in Reacted Sulfide Surfaces. *Miner. Eng.* **2000**, *13*, 857-870.
- (113) Eggleston, C. M.; Hochella, M. F. Scanning Tunneling Microscopy of Galena (100) Surface Oxidation and Sorption of Aqueous Gold. *Science* **1991**, *254*, 983-986.
- (114) Kim, B. S.; Hayes, R. A.; Prestidge, C. A.; Ralston, J.; Smart, R. S. C. Scanning Tunneling Microscopy Studies of Galena: The Mechanisms of Oxidation in Aqueous Solution. *Langmuir* **1995**, *11*, 2554-2562.
- (115) Israelachvili, J.; Min, Y.; Akbulut, M.; Alig, A.; Carver, G.; Greene, W.; Kristiansen, K.; Meyer, E.; Pesika, N.; Rosenberg, K. Recent Advances in the Surface Forces Apparatus (SFA) Technique. *Rep. Prog. Phys.* **2010**, *73*, 036601.
- (116) Zeng, H.; Tian, Y.; Anderson, T. H.; Tirrell, M.; Israelachvili, J. N. New SFA Techniques for Studying Surface Forces and Thin Film Patterns Induced by Electric Fields. *Langmuir* **2008**, *24*, 1173-1182.
- (117) Israelachvili, J.; Pashley, R. The Hydrophobic Interaction Is Long Range, Decaying Exponentially with Distance. *Nature* **1982**, *300*, 341-342.
- (118) Israelachvili, J. N.; Pashley, R. M. Molecular Layering of Water at Surfaces and Origin of Repulsive Hydration Forces. *Nature* **1983**, *306*, 249-250.
- (119) Israelachvili, J. N.; McGuiggan, P. M. Forces between Surfaces in Liquids. *Science* **1988**, *241*, 795-800.
- (120) Valtiner, M.; Banquy, X.; Kristiansen, K.; Greene, G. W.; Israelachvili, J. N. The Electrochemical Surface Forces Apparatus: The Effect of Surface Roughness, Electrostatic Surface Potentials, and Anodic Oxide Growth on Interaction Forces, and

Friction between Dissimilar Surfaces in Aqueous Solutions. *Langmuir* **2012**, *28*, 13080-13093.

(121) Hampton, M. A.; Plackowski, C.; Nguyen, A. V. Physical and Chemical Analysis of Elemental Sulfur Formation During Galena Surface Oxidation. *Langmuir* **2011**, *27*, 4190-4201.

(122) Reid, O. G.; Munechika, K.; Ginger, D. S. Space Charge Limited Current Measurements on Conjugated Polymer Films using Conductive Atomic Force Microscopy. *Nano letters* **2008**, *8*, 1602-1609.

(123) Tan, S.; Tang, Z.; Liang, X.; Kotov, N. A. Resonance Tunneling Diode Structures on CdTe Nanowires Made by Conductive AFM. *Nano Letters* **2004**, *4*, 1637-1641.

(124) Zhang, L.; Mitani, Y. Structural and Electrical Evolution of Gate Dielectric Breakdown Observed by Conductive Atomic Force Microscopy. *Appl. Phys. Lett.* **2006**, *88*, 032906.

(125) Balke, N.; Winchester, B.; Ren, W.; Chu, Y. H.; Morozovska, A. N.; Eliseev, E. A.; Huijben, M.; Vasudevan, R. K.; Maksymovych, P.; Britson, J. Enhanced Electric Conductivity at Ferroelectric Vortex Cores in BiFeO₃. *Nature Physics* **2012**, *8*, 81-88.

(126) Xu, D.; Watt, G. D.; Harb, J. N.; Davis, R. C. Electrical Conductivity of Ferritin Proteins by Conductive AFM. *Nano letters* **2005**, *5*, 571-577.

(127) Headrick, J. E.; Berrie, C. L. Alternative Method for Fabricating Chemically Functionalized Afm Tips: Silane Modification of HF-Treated Si₃N₄ Probes. *Langmuir* **2004**, *20*, 4124-4131.

(128) Buckley, A. N.; Woods, R. An X-Ray Photoelectron Spectroscopic Study of the Oxidation of Galena. *Appl. Surf. Sci.* **1984**, *17*, 401-414.

- (129) Richardson, P.; Yoon, R.-H.; Woods, R.; Buckley, A. The Photoelectrochemistry of Galena. *Int. J. Miner. Process.* **1994**, *41*, 77-97.
- (130) Chen, J.; Long, X.; Chen, Y. Comparison of Multilayer Water Adsorption on the Hydrophobic Galena (PbS) and Hydrophilic Pyrite (FeS₂) Surfaces: A DFT Study. *J. Phys. Chem. C* **2014**, *118*, 11657-11665.
- (131) Tsukruk, V. V.; Bliznyuk, V. N. Adhesive and Friction Forces between Chemically Modified Silicon and Silicon Nitride Surfaces. *Langmuir* **1998**, *14*, 446-455.
- (132) Christenson, H. K.; Claesson, P. M. Direct Measurements of the Force between Hydrophobic Surfaces in Water. *Adv. Colloid Interface Sci.* **2001**, *91*, 391-436.
- (133) Stephenson, T.; Li, Z.; Olsen, B.; Mitlin, D., Lithium Ion Battery Applications of Molybdenum Disulfide (MoS₂) Nanocomposites. *Energy & Environmental Science* **2014**, *7*, 209-231.
- (134) Gong, Y.; Liu, Z.; Lupini, A. R.; Shi, G.; Lin, J.; Najmaei, S.; Lin, Z.; Elías, A. L.; Berkdemir, A.; You, G., Band Gap Engineering and Layer-by-Layer Mapping of Selenium-Doped Molybdenum Disulfide. *Nano letters* **2013**, *14*, 442-449.
- (135) Kibsgaard, J.; Chen, Z.; Reinecke, B. N.; Jaramillo, T. F., Engineering the Surface Structure of MoS₂ to Preferentially Expose Active Edge Sites for Electrocatalysis. *Nature materials* **2012**, *11*, 963-969.
- (136) Radisavljevic, B.; Kis, A., Mobility Engineering and a Metal-Insulator Transition in Monolayer MoS₂. *Nature materials* **2013**, *12*, 815-820.
- (137) Cheng, R.; Jiang, S.; Chen, Y.; Liu, Y.; Weiss, N.; Cheng, H.-C.; Wu, H.; Huang, Y.; Duan, X., Few-Layer Molybdenum Disulfide Transistors and Circuits for High-Speed Flexible Electronics. *Nature communications* **2014**, *5*, 5143.

- (138) Zhu, W.; Low, T.; Lee, Y.-H.; Wang, H.; Farmer, D. B.; Kong, J.; Xia, F.; Avouris, P., Electronic Transport and Device Prospects of Monolayer Molybdenum Disulfide Grown by Chemical Vapour Deposition. *Nature communications* **2014**, *5*, 3087.
- (139) Gao, M.-R.; Liang, J.-X.; Zheng, Y.-R.; Xu, Y.-F.; Jiang, J.; Gao, Q.; Li, J.; Yu, S.-H., An Efficient Molybdenum Disulfide/Cobalt Diselenide Hybrid Catalyst for Electrochemical Hydrogen Generation. *Nature communications* **2015**, *6*, 5982.
- (140) Karunadasa, H. I.; Montalvo, E.; Sun, Y.; Majda, M.; Long, J. R.; Chang, C. J., A Molecular MoS₂ Edge Site Mimic for Catalytic Hydrogen Generation. *Science* **2012**, *335*, 698-702.
- (141) Zhou, F.; Xin, S.; Liang, H. W.; Song, L. T.; Yu, S. H., Carbon Nanofibers Decorated with Molybdenum Disulfide Nanosheets: Synergistic Lithium Storage and Enhanced Electrochemical Performance. *Angew. Chem., Int. Ed.* **2014**, *53*, 11552-11556.
- (142) Sun, G.; Zhang, X.; Lin, R.; Yang, J.; Zhang, H.; Chen, P., Hybrid Fibers Made of Molybdenum Disulfide, Reduced Graphene Oxide, and Multi-Walled Carbon Nanotubes for Solid-State, Flexible, Asymmetric Supercapacitors. *Angew. Chem., Int. Ed.* **2015**, *127*, 4734-4739.
- (143) Narayanan, T. N.; Vusa, C. S.; Alwarappan, S., Selective and Efficient Electrochemical Biosensing of Ultrathin Molybdenum Disulfide Sheets. *Nanotechnology* **2014**, *25*, 335702.
- (144) Sarkar, D.; Liu, W.; Xie, X.; Anselmo, A. C.; Mitragotri, S.; Banerjee, K., MoS₂ Field-Effect Transistor for Next-Generation Label-Free Biosensors. *Acs Nano* **2014**, *8*, 3992-4003.
- (145) Winer, W., Molybdenum Disulfide as a Lubricant: A Review of the Fundamental

Knowledge. *Wear* **1967**, *10*, 422-452.

(146) Gaur, A. P.; Sahoo, S.; Ahmadi, M.; Dash, S. P.; Guinel, M. J.-F.; Katiyar, R. S., Surface Energy Engineering for Tunable Wettability through Controlled Synthesis of MoS₂. *Nano letters* **2014**, *14*, 4314-4321.

(147) Govind Rajan, A.; Sresht, V.; Pádua, A. A.; Strano, M. S.; Blankschtein, D., Dominance of Dispersion Interactions and Entropy over Electrostatics in Determining the Wettability and Friction of Two-Dimensional MoS₂ Surfaces. *ACS nano* **2016**, *10*, 9145-9155.

(148) Kozbial, A.; Gong, X.; Liu, H.; Li, L., Understanding the Intrinsic Water Wettability of Molybdenum Disulfide (MoS₂). *Langmuir* **2015**, *31*, 8429-8435.

(149) Chow, P. K.; Singh, E.; Viana, B. C.; Gao, J.; Luo, J.; Li, J.; Lin, Z.; Elías, A. L.; Shi, Y.; Wang, Z., Wetting of Mono and Few-Layered WS₂ and MoS₂ Films Supported on Si/SiO₂ Substrates. *ACS nano* **2015**, *9*, 3023-3031.

(150) Ralston, J.; Fornasiero, D.; Hayes, R., Bubble-Particle Attachment and Detachment in Flotation. *Int. J. Miner. Process.* **1999**, *56*, 133-164.

(151) Horn, R. G.; Asadullah, M.; Connor, J. N., Thin Film Drainage: Hydrodynamic and Disjoining Pressures Determined from Experimental Measurements of the Shape of a Fluid Drop Approaching a Solid Wall. *Langmuir* **2006**, *22*, 2610-2619.

(152) Tabor, R. F.; Chan, D. Y.; Grieser, F.; Dagastine, R. R., Structural Forces in Soft Matter Systems. *J. Phys. Chem. Lett.* **2011**, *2*, 434-437.

(153) Fosu, S.; Skinner, W.; Zanin, M., Detachment of Coarse Composite Sphalerite Particles from Bubbles in Flotation: Influence of Xanthate Collector Type and Concentration. *Miner. Eng.* **2015**, *71*, 73-84.

- (154) Pugh, R., Macromolecular Organic Depressants in Sulphide Flotation-a Review, 1. Principles, Types and Applications. *Int. J. Miner. Process.* **1989**, *25*, 101-130.
- (155) Pearse, M., An Overview of the Use of Chemical Reagents in Mineral Processing. *Miner. Eng.* **2005**, *18*, 139-149.
- (156) Mierczynska-Vasilev, A.; Ralston, J.; Beattie, D. A., Adsorption of Modified Dextrins on Talc: Effect of Surface Coverage and Hydration Water on Hydrophobicity Reduction. *Langmuir* **2008**, *24*, 6121-6127.
- (157) Beaussart, A.; Parkinson, L.; Mierczynska-Vasilev, A.; Ralston, J.; Beattie, D. A., Effect of Adsorbed Polymers on Bubble-Particle Attachment. *Langmuir* **2009**, *25*, 13290-13294.
- (158) Cuba-Chiem, L. T.; Huynh, L.; Ralston, J.; Beattie, D. A., In Situ Particle Film ATR FTIR Spectroscopy of Carboxymethyl Cellulose Adsorption on Talc: Binding Mechanism, Ph Effects, and Adsorption Kinetics. *Langmuir* **2008**, *24*, 8036-8044.
- (159) Kaggwa, G. B.; Huynh, L.; Ralston, J.; Bremmell, K., The Influence of Polymer Structure and Morphology on Talc Wettability. *Langmuir* **2006**, *22*, 3221-3227.
- (160) Kaggwa, G. B.; Froebe, S.; Huynh, L.; Ralston, J.; Bremmell, K., Morphology of Adsorbed Polymers and Solid Surface Wettability. *Langmuir* **2005**, *21*, 4695-4704.
- (161) Vakarelski, I. U.; Lee, J.; Dagastine, R. R.; Chan, D. Y.; Stevens, G. W.; Grieser, F., Bubble Colloidal Afm Probes Formed from Ultrasonically Generated Bubbles. *Langmuir* **2008**, *24*, 603-605.
- (162) Tabor, R. F.; Chan, D. Y.; Grieser, F.; Dagastine, R. R., Anomalous Stability of Carbon Dioxide in PH-Controlled Bubble Coalescence. *Angew. Chem., Int. Ed.* **2011**, *123*, 3516-3518.

- (163) Chan, D. Y.; Klaseboer, E.; Manica, R., Theory of Non-Equilibrium Force Measurements Involving Deformable Drops and Bubbles. *Adv. Colloid Interface Sci.* **2011**, *165*, 70-90.
- (164) Raghavan, S.; Hsu, L. L., Factors Affecting the Flotation Recovery of Molybdenite from Porphyry Copper Ores. *Int. J. Miner. Process.* **1984**, *12*, 145-162.
- (165) Wie, J. M.; Fuerstenau, D., The Effect of Dextrin on Surface Properties and the Flotation of Molybdenite. *Int. J. Miner. Process.* **1974**, *1*, 17-32.
- (166) Lu, Z.; Liu, Q.; Xu, Z.; Zeng, H., Probing Anisotropic Surface Properties of Molybdenite by Direct Force Measurements. *Langmuir* **2015**, *31*, 11409-11418.
- (167) Beaussart, A.; Mierczynska-Vasilev, A.; Beattie, D. A., Evolution of Carboxymethyl Cellulose Layer Morphology on Hydrophobic Mineral Surfaces: Variation of Polymer Concentration and Ionic Strength. *J. Colloid Interface Sci.* **2010**, *346*, 303-310.
- (168) Yaminsky, V. V.; Ohnishi, S.; Vogler, E. A.; Horn, R. G., Stability of Aqueous Films between Bubbles. Part 1. The Effect of Speed on Bubble Coalescence in Purified Water and Simple Electrolyte Solutions. *Langmuir* **2010**, *26*, 8061-8074.
- (169) Clark, M. M., *Transport Modeling for Environmental Engineers and Scientists*; John Wiley & Sons, **2011**.
- (170) Christenson, H. K.; Claesson, P. M., Cavitation and the Interaction between Macroscopic Hydrophobic Surfaces. *Science* **1988**, *239*, 390-392.
- (171) Tsao, Y.-H.; Evans, D. F.; Wennerstrom, H., Long-Range Attractive Force between Hydrophobic Surfaces Observed by Atomic Force Microscopy. *Science* **1993**, *262*, 547-550.

- (172) Rubio, J.; Souza, M.; Smith, R., Overview of Flotation as a Wastewater Treatment Technique. *Miner. Eng.* **2002**, *15*, 139-155.
- (173) Kemper, M., State-of-the-Art and New Technologies in Flotation Deinking. *Int. J. Miner. Process.* **1999**, *56*, 317-333.
- (174) Albijanic, B.; Ozdemir, O.; Nguyen, A. V.; Bradshaw, D., A Review of Induction and Attachment Times of Wetting Thin Films between Air Bubbles and Particles and Its Relevance in the Separation of Particles by Flotation. *Adv. Colloid Interface Sci.* **2010**, *159*, 1-21.
- (175) Schulze, H., Hydrodynamics of Bubble-Mineral Particle Collisions. *Miner. Process. Extr. Metall. Rev.* **1989**, *5*, 43-76.
- (176) Dai, Z.; Fornasiero, D.; Ralston, J., Particle–Bubble Attachment in Mineral Flotation. *J. Colloid Interface Sci.* **1999**, *217*, 70-76.
- (177) Tian, Y.; Pesika, N.; Zeng, H.; Rosenberg, K.; Zhao, B.; McGuiggan, P.; Autumn, K.; Israelachvili, J., Adhesion and Friction in Gecko Toe Attachment and Detachment. *Proc. Natl. Acad. Sci. U. S. A.* **2006**, *103*, 19320-19325.
- (178) Zhang, X.; Kumar, A.; Scales, P. J., Effects of Solvency and Interfacial Nanobubbles on Surface Forces and Bubble Attachment at Solid Surfaces. *Langmuir* **2011**, *27*, 2484-2491.
- (179) Alcantar, N.; Israelachvili, J.; Boles, J., Forces and Ionic Transport between Mica Surfaces: Implications for Pressure Solution. *Geochim. Cosmochim. Acta* **2003**, *67*, 1289-1304.
- (180) Duke, C.; Wang, Y., Surface Structure and Bonding of the Cleavage Faces of

- Tetrahedrally Coordinated II–VI Compounds. *J. Vac. Sci. Technol., B* **1988**, *6*, 1440-1443.
- (181) Nguyen, A., Historical Note on the Stefan–Reynolds Equations. *J. Colloid Interface Sci.* **2000**, *231*, 195.
- (182) Nguyen, A.; Schulze, H. J., *Colloidal Science of Flotation*; CRC Press, **2003**.
- (183) Mielczarski, J.; Mielczarski, E.; Cases, J., Interaction of Amyl Xanthate with Chalcopyrite, Tetrahedrite, and Tennantite at Controlled Potentials. Simulation and Spectroelectrochemical Results for Two-Component Adsorption Layers. *Langmuir* **1996**, *12*, 6521-6529.
- (184) Mielczarski, J. A.; Mielczarski, E.; Zachwieja, J.; Cases, J., In Situ and Ex Situ Infrared Studies of Nature and Structure of Thiol Monolayers Adsorbed on Cuprous Sulfide at Controlled Potential. *Langmuir* **1995**, *11*, 2787-2799.
- (185) Yang, C.; Dabros, T.; Li, D.; Czarnecki, J.; Masliyah, J. H., Measurement of the Zeta Potential of Gas Bubbles in Aqueous Solutions by Microelectrophoresis Method. *J. Colloid Interface Sci.* **2001**, *243*, 128-135.
- (186) Cho, S.-H.; Kim, J.-Y.; Chun, J.-H.; Kim, J.-D., Ultrasonic Formation of Nanobubbles and Their Zeta-Potentials in Aqueous Electrolyte and Surfactant Solutions. *Colloids Surf., A* **2005**, *269*, 28-34.
- (187) Han, M.; Kim, M.; Shin, M., Generation of a Positively Charged Bubble and Its Possible Mechanism of Formation. *J. Water Supply Res. Technol. AQUA* **2006**, *55*, 471-478.
- (188) Ji, Y.; Lu, Q.; Liu, Q.; Zeng, H., Effect of Solution Salinity on Settling of Mineral Tailings by Polymer Flocculants. *Colloids Surf., A* **2013**, *430*, 29-38.
- (189) Pashley, R.; Israelachvili, J., DLVO and Hydration Forces between Mica Surfaces in

- Mg²⁺, Ca²⁺, Sr²⁺, and Ba²⁺ Chloride Solutions. *J. Colloid Interface Sci.* **1984**, *97*, 446-455.
- (190) Teng, F.; Zeng, H.; Liu, Q., Understanding the Deposition and Surface Interactions of Gypsum. *J. Phys. Chem. C* **2011**, *115*, 17485-17494.
- (191) Craig, V.; Ninham, B.; Pashley, R., Effect of Electrolytes on Bubble Coalescence. *Nature* **1993**, *364*, 317-319.
- (192) Craig, V. S.; Ninham, B. W.; Pashley, R. M., The Effect of Electrolytes on Bubble Coalescence in Water. *The Journal of Physical Chemistry* **1993**, *97*, 10192-10197.
- (193) Faghihnejad, A.; Zeng, H., Hydrophobic Interactions between Polymer Surfaces: Using Polystyrene as a Model System. *Soft Matter* **2012**, *8*, 2746-2759.
- (194) Faghihnejad, A.; Zeng, H., Interaction Mechanism between Hydrophobic and Hydrophilic Surfaces: Using Polystyrene and Mica as a Model System. *Langmuir* **2013**, *29*, 12443-12451.
- (195) Wang, W.; Zhou, Z.; Nandakumar, K.; Masliyah, J. H.; Xu, Z., An Induction Time Model for the Attachment of an Air Bubble to a Hydrophobic Sphere in Aqueous Solutions. *Int. J. Miner. Process.* **2005**, *75*, 69-82.
- (196) Ahmed, N.; Jameson, G., The Effect of Bubble Size on the Rate of Flotation of Fine Particles. *Int. J. Miner. Process.* **1985**, *14*, 195-215.
- (197) Yoon, R.; Luttrell, G., The Effect of Bubble Size on Fine Particle Flotation. *Min. Proc. Ext. Met. Rev.* **1989**, *5*, 101-122.
- (198) Dai, Z.; Fornasiero, D.; Ralston, J., Particle-Bubble Attachment in Mineral Flotation. *Int. J. Miner. Process.* **1999**, *217*, 70-76.
- (199) Matis, K.; Gallios, G.; Kydros, K., Separation of Fines by Flotation Techniques. *Separ. Technol.* **1993**, *3*, 76-90.

(200) Zhou, Z.; Xu, Z.; Finch, J., On the Role of Cavitation in Particle Collection During Flotation-a Critical Review. *Miner. Eng.* **1994**, *7*, 1073-1084.

(201) Mishchuk, N.; Ralston, J.; Fornasiero, D., Influence of Very Small Bubbles on Particle/Bubble Heterocoagulation. *J. Colloid Interface Sci.* **2006**, *301*, 168-175.